
Magnetic and dielectric properties of functional minerals:

The cases of sugilite, eosphorite, and
rockbridgeite

BENEDIKT RÖSKA



*Dissertation zur Erlangung des Doktorgrades
an der Fakultät für Geowissenschaften
der Ludwig-Maximilians-Universität München*

München - June 5, 2018

1st Reviewer: Prof. Dr. S.-H. Park

2nd Reviewer: Prof. Dr. P. Gille

Date of the oral examination: November 16, 2018

Abbreviations

□ : vacancy

3d TM: *3d* transitional metal

ADPs: atomic displacement parameters

AFM: antiferromagnetic

D6MR: double 6-membered ring

DE: double exchange

ΔF : difference Fourier

FM: ferromagnetic

HB(s): hydrogen bond(s)

HBN(s): hydrogen bond network(s)

LIB: lithium-ion battery

MSG: magnetic space group

M: multiplicity in chemical formula based on site occupation

M: magnetic moment at crystallographic site

pfu: per formula unit

RT: room temperature

SE: superexchange interaction

SIB: sodium-ion battery

T_N : Néel Temperature

T_C : Curie Temperature

TO: tetrahedral-octahedral

Abstract

The present work explains structure-property relations combining physical characterisation with subtle structure analysis using neutron diffraction technique. Magnetic and dielectric properties of two oxyhydroxides and an as-synthesised double 6-membered ring (D6MR) silicate were characterised to evaluate charge transportation, proton dynamics, and magnetic spin order.

A synthesis route for the D6MR sugilite-type analogue $\text{Na}_2\text{Fe}_2\text{K}[\text{Li}_3\text{Si}_{12}\text{O}_{30}]$ was established under mild hydrothermal conditions. Impedance spectra of as-synthesised powder reveal a bulk conductivity of $1.2 \times 10^{-5} \text{ S cm}^{-1}$ at 923 K. 2D hopping pathways of Na^+ - and Li^+ -ions were extracted from ΔF maps of structure analyses with neutron powder diffraction data collected at 298 - 1123 K. Wide crystal chemical flexibility and thermal stability make (D6MR) silicates cost-effective and environment-friendly candidates for combined Li/Na all-solid state electrochemical cells.

Eosphorite, $(\text{Mn}_{0.5}\text{Fe}_{0.5})^{2+}\text{AlPO}_4(\text{OH})_2\text{H}_2\text{O}$, shows an anomalous increase in the real part of the permittivity (ϵ') while cooling from 300 K to ≈ 70 K. A paraelectric to antiferroelectric transition is excluded due to the absence of discontinuities above T_N (≈ 7 K) in the heat capacity curve. The dielectric behaviour is explained with electric field induced proton dynamics in very short hydrogen bonds of $2.480(3) \text{ \AA}$. The critical temperature of ϵ' could be shifted to ≈ 2 K applying isostatic pressure ($P \leq 1.51 \text{ GPa}$). A strong correlation of proton transfer and compression of the hydrogen bond length close to the symmetrisation length is inferred.

Four independent hydrogen sites were determined in a rockbridgeite-type compound $\text{Fe}^{2+}\text{Fe}_{3.2}^{3+}(\text{Mn}^{2+}, \text{Zn})_{0.8}(\text{PO}_4)_3(\text{OH})_{4.2}(\text{HOH})_{0.8}$ using neutron powder diffraction at 298 K and 25 K. Protons are disordered over a honeycomb like network of hydrogen bonds running infinitely in [100], reminiscent of dynamically disordered hydrogen bond networks in superprotonic sulphates and selenates. High proton conductivity is experimentally supported by dramatic increases of real and imaginary parts of the dielectric response starting around 298 K. A strict correlation of protonic disorder with defects at half occupied Fe^{3+} sites in the aliovalent 3d TM bearing octahedral framework is indicated by structure analyses. Below the magnetic transition temperature of 81 - 83 K, the ferrimagnetic spin structure could be solved from analysis of neutron diffraction data collected at 25 K. Complex exchange interactions from three magnetic sublattices cause a net magnetisation parallel to [001]. With its thermal stability up to 600 K, this phosphatic oxyhydroxide compounds could be an interesting prototype for proton exchange membranes in fuel cells.

Contents

I	Introduction	1
1	Oxide & oxyhydroxide minerals as functional materials	2
2	Introduction to case studies	3
2.1	Na ⁺ /Li ⁺ -ionic conductivity in Fe ₂ Na ₂ K[Li ₃ Si ₁₂ O ₃₀]	3
2.2	Anomalous dielectric response of short hydrogen bonds under pressure: the case of eosphorite, (Mn,Fe) ²⁺ AlPO ₄ (OH) ₂ H ₂ O	4
2.3	Hydrogen-bond network and ferrimagnetism in a rockbridgeite-type compound, Fe ²⁺ Fe _{3.2} ³⁺ (Mn ²⁺ ,Zn) _{0.8} (PO ₄) ₃ (OH) _{4.2} (HOH) _{0.8}	5
3	Applications of solid state ionic/protonic conductors	7
3.1	Ion batteries	7
3.2	Proton exchange membrane fuel cells (PEMFCs)	9
II	Theoretical background	13
4	Ionic conduction and disorder phenomena in inorganic solids	14
4.1	Defects driving ionic conductivity	14
4.2	Hopping model: ionic conduction in bulk crystals	15
5	Hydrogen bonds and proton dynamics in the solid state	18
5.1	The hydrogen bond - an incipient proton transfer reaction	19
5.2	Polarisability and order-disorder phenomena in hydrogen bonds	21
5.3	Proton conductivity in non-metallic solids	22
6	Magnetic interactions in 3d TM oxides and oxyhydroxides	26
6.1	Magnetic moments	26
6.2	Magnetic exchange interactions in oxides	27
6.2.1	Superexchange interaction (SE)	28
6.2.2	Double exchange	30
6.2.3	Direct exchange	30
6.3	Magnetic order in oxides	31
6.3.1	Symmetry of magnetic spin orders	32
III	Instrumental methods	34
7	Analytical characterisation methods	35
7.1	Chemical analysis with Electron Probe micro analysis (EPMA)	35
7.2	Thermal behaviour	35
7.2.1	Heat capacity at T ≤ 298 K	35
7.2.2	Thermogravimetry (TGA) and differential scanning calorimetry (DSC) at T ≥ RT	36
7.3	Magnetometric characterisation	36

7.4	Spectroscopy	37
7.4.1	Fourier Transformed Infrared (FTIR) Spectroscopy	37
7.4.2	Dielectric spectroscopy	38
7.4.3	^{57}Fe Mössbauer spectroscopy	39
7.5	Structure analysis using X-ray and neutron diffraction techniques	40
7.5.1	X-ray single crystal diffraction (XSD)	43
7.5.2	Powder diffraction methods	43
7.6	Laue method	44
IV	Case studies	45
8	Na^+/Li^+-ionic conductivity in $\text{Fe}_2\text{Na}_2\text{K}[\text{Li}_3\text{Si}_{12}\text{O}_{30}]$	46
8.1	Hydrothermal synthesis	46
8.2	Impedance Spectroscopy	46
8.3	Structure analysis	47
8.4	Mechanisms of ionic conduction	48
8.5	Conclusion	52
9	Anomalous dielectric response of short hydrogen bonds under pressure: the case of eosphorite, $(\text{Mn}_{0.5},\text{Fe}_{0.5})^{2+}\text{AlPO}_4(\text{OH})_2\text{H}_2\text{O}$	53
9.1	Hydrogen bonds	53
9.2	Dielectric response	53
9.3	Conclusion	54
10	Determination of the hydrogen-bond network and the ferrimagnetic structure of a rockbridgeite-type compound, $\text{Fe}^{2+}\text{Fe}_{3.2}^{3+}(\text{Mn}^{2+},\text{Zn})_{0.8}(\text{PO}_4)_3(\text{OH})_{4.2}(\text{HOH})_{0.8}$	56
10.1	A new structure for rockbridgeite-type compounds	56
10.2	Proton conduction in the hydrogen bond network	58
10.3	Ferrimagnetic spin structure below 25 K	59
10.4	Conclusion	63
11	Conclusion	64
	Bibliography	66
V	Appendix	74
12	Publication on sugilite	75
13	Publication on eosphorite	87
14	Publication on rockbridgeite	93
	Acknowledgement	109

Part I.
Introduction

1. Oxide & oxyhydroxide minerals as functional materials

Discovery of novel physical properties of solid state matter has often been driven by investigations of prototype minerals. The development of new functional materials is based on the understanding of their fundamental physical properties. Nature provides a large pool of functional compounds of which the underlying physical mode of action can be systematically trimmed for applications by finding synthetic counterparts. Magnetite, Fe_3O_4 , was the first known material with magnetic remanence and subject to Néel's ground-breaking work on ferrimagnetism and to Zener's findings on magnetic direct exchange interactions [1, 2]. For decades, ferrite derivatives of $\gamma\text{-Fe}_3\text{O}_4$, were almost exclusively used for magnetic tape storage devices, even in the NASA space shuttle until the 1990s for their reliability [3]. Perovskite and garnet-type compounds are studied to be used as stable superionic and protonic conductors [4]. The first evidence for *advanced superionic conductivity* of $10^{-10^2} \text{ S cm}^{-1}$ at RT were discovered in pearceite-polybasite $(\text{Ag, Cu})_{16}(\text{Sb, As})_2\text{S}_{11}$ group minerals first in 2006 [5]. The phenomenon of ferroelectricity was discovered only in the 1920s in rochelle salt [6], initiating a tremendous journey in applied material science and physics [7]. Coupling of magnetic order and electric polarisation are merged in the hot topic of magneto-electric multiferroics, a new promising energy efficient approach for data storage and sensor applications [8]. Pioneering work in this field was accomplished in huebnerite- (MnWO_4) and dellafossite-type (CuFeO_2) phases showing complex magnetic spin-spiral orders [9–11].

The above mentioned examples include many functional oxides providing a plethora of applications in energy efficient electromagnetic information storage, photonics, superconductors, optoelectronics, fuel cell and battery materials, or photovoltaics [12]. The rich variety of oxide properties such as magnetism, ferroelectricity, protonic and ionic conductivity/storage, reaching into advanced fields of multiferroicity and spin-orbital coupling offers a wide scientific field to probe into. High availability, new synthesis and deposition routes, chemical and thermal stability, as well as their broad structural and chemical flexibility attracted attention to tunable functional oxides [13].

Oxides are typically built-up of tetrahedral-octahedral (TO) frameworks in which cations are coordinated by oxygen ligands forming mixed strong covalent and ionic bonds. TO building-units are interlinked to each other by sharing faces, edges, and corners realising dense to porous topologies. Electronic and magnetic interactions among aliovalent $3d$ TM are established via mutual overlap with oxygen orbitals involving magnetic spin order and/or charge-order transitions.

Despite their close structural kinship to oxides, the functionality of oxyhydroxide minerals and synthetic counterparts has been addressed less frequently. The prominent feature of oxyhydroxides is the partial substitution of oxygen ligands by OH and HOH groups which involves the presence of hydrogen bonds (HBs) in the form of $\text{O}-\text{H}\cdots\text{O}$ in a rigid TO framework. While HBs seem to play a decisive role for

the structural stability of oxyhydroxides [14], proton dynamics in hydrogen bond networks (HBNs) may open the field for dielectric phenomena such as proton conduction.

Recently, the subgroup of phosphatic oxyhydroxides has attracted attention for their diverse properties. Hureaulite-type compounds $\text{Mn}_5(\text{PO}_3(\text{OH}))_2(\text{PO}_4)_2 \cdot 4 \text{H}_2\text{O}$, are widely used as additives increasing wear and corrosion resistance of steel, and are investigated for their optic, magnetic and electrochemical properties [15–18]. Lipscombite-type, $\text{Fe}_{2-y}\text{PO}_4(\text{OH})$ ($0 \leq y \leq 2/3$), and barbosalite-type compounds $\text{Fe}^{2+}\text{Fe}^{3+}(\text{PO}_4)_2(\text{OH})_2$, show magnetic transitions around 90 K and 160 K, respectively, and are considered as electrode materials [19, 20]. Eosphorite $(\text{Mn, Fe})^{2+}\text{AlPO}_4(\text{OH})_2 \cdot \text{H}_2\text{O}$ inherits antiferromagnetic ordering below 7 K, of which the spin structure was recently solved [21].

This work highlights phosphatic oxyhydroxide minerals and D6MR silicates as prototype functional materials. Their dielectric and magnetic properties are of importance to modern applications, as briefed in the following.

2. Introduction to case studies

2.1. Na^+/Li^+ -ionic conductivity in $\text{Fe}_2\text{Na}_2\text{K}[\text{Li}_3\text{Si}_{12}\text{O}_{30}]$

In the course of finding stable electrolyte materials for all-solid electrochemical cells, the sugilite-sogdianite solid solution was investigated showing anisotropic superionic conductivity starting at temperatures of about 1000 K [22]. Sugilite belongs to the group of Li-bearing milarite-type compounds with the general formula $^{[6]}\text{A}_2$ $^{[9]}\text{B}_2$ $^{[12]}\text{C}$ $^{[18]}\text{D}$ $^{[4]}\text{T}_2$ $^{[4]}\text{T}_{12}$ O_{30} (*P6/mcc*) [23]. As shown in Fig. 2.1, this structure-type features double 6-membered rings (D6MR) of $[\text{T}_1\text{O}_4]$ -tetrahedra forming channels in the crystallographic *c*-axis. These are linked by a 2D TO framework lying in the (*a-b*) plane which consists of alternating $[\text{T}_2\text{O}_4]$ and $[\text{AO}_6]$ moieties. The pseudo-porous structure offers capacious voids for cations at *B*, *C*, and *D* sites. Their size is too small for H_2O making the structure resistant to hydration. Exhibiting an extremely wide crystal chemical flexibility, the milarite-family comprises 23 members, present as polycrystalline masses or small crystallite needles [24]. The high thermal stability up to 1300 K and the chemical flexibility similar to those of perovskites and spinels, make milarite-type compounds ideal candidates to find economical- and ecological-friendly solid solutions for novel battery materials.

Case study #1 (Cha. 8; Cha. 12 in Appendix) covers the detailed structural and dielectric characterisation of synthetic end-member analogue to sugilite, $\text{Na}_2\text{Fe}_2\text{K}[\text{Li}_3\text{Si}_{12}\text{O}_{30}]$. Sugilite specimen from few known natural occurrences [25–27] are described by the generic formula $(\text{Fe}^{3+}, \text{Al}, \text{Mn}^{3+})_2\text{Na}_2\text{K}[\text{Li}_3\text{Si}_{12}\text{O}_{30}]$. Its Zr-rich counterpart sogdianite, $(\text{Zr}, \text{Ti}, \text{Fe}^{3+}, \text{Al})_2(\text{Na}, \square)_2\text{K}[\text{Li}_3\text{Si}_{12}\text{O}_{30}]$ [\square = vacancy], contains considerably less Na for the presence of quadrivalent cations

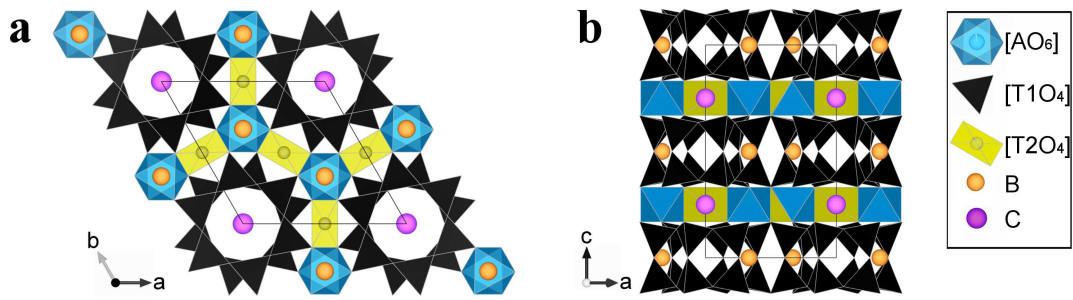


Fig. 2.1.: Framework structure of milarite-type minerals, with the site occupation T1 = Si, T2 = Li, A = Fe^{3+} , B = Na, C = K, and D = empty in synthetic sugilite analogue $\text{Na}_2\text{Fe}_2\text{K}[\text{Li}_3\text{Si}_{12}\text{O}_{30}]$.

at the A site, while the content of Li is constant in the solid solution. Curiously, Na-rich sugilite shows a higher ionic conductivity compared to sogdianite (Park et al., to be published), which is ascribed to joint charge transfer of Li^+ and Na^+ .

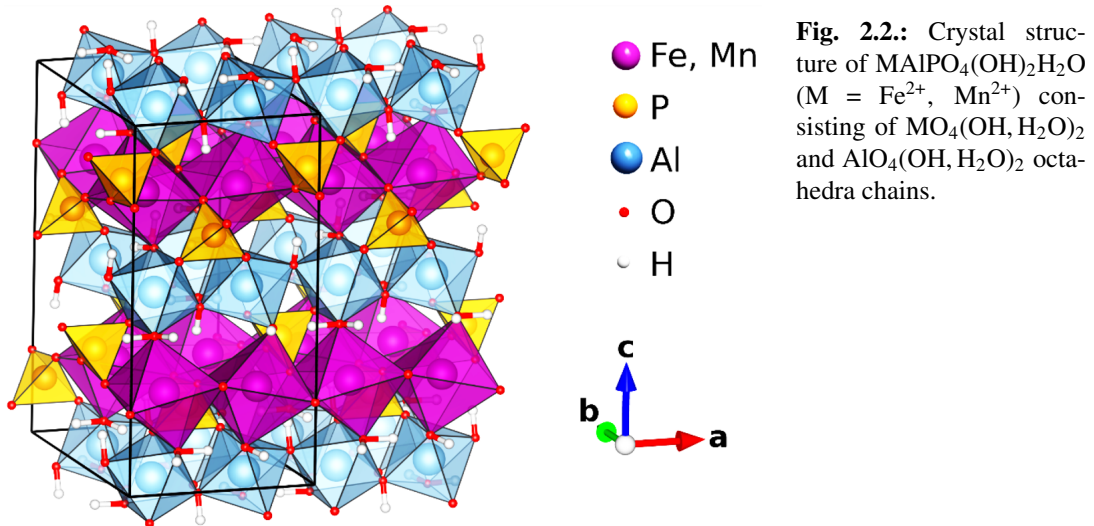
A mild hydrothermal route is suggested to obtain the sugilite analogue $(\text{Fe})_2\text{Na}_2\text{K}[\text{Li}_3\text{Si}_{12}\text{O}_{30}]$. As-synthesised powder samples of this compound were investigated via impedance spectroscopy and neutron powder diffraction at variable temperatures. Dynamic disorder and interstitial sites of Li and Na were found via subtle structure analysis and subsequently evaluated in ΔF maps, which allowed to understand ionic conduction mechanisms.

2.2. Anomalous dielectric response of short hydrogen bonds under pressure: the case of eosphorite, $(\text{Mn}_{0.5}, \text{Fe}_{0.5})^{2+} \text{AlPO}_4(\text{OH})_2\text{H}_2\text{O}$

A variety of H-bearing materials feature (anti-)ferroelectric transitions involving proton ordering within short HBs of $\approx 2.5 \text{ \AA}$ in length. In the prominent examples KH_2PO_4 (KDP)-type structures, squaric acid ($\text{H}_2\text{C}_4\text{O}_4$), or mono-protonated diazabicyclo[2.2.2]octane (HdabcoH⁺) derivatives, the concerted proton ordering in asymmetric HBs gives rise to bulk or layer-confined polar states [7, 28]. The critical temperature of such disorder-order transitions is sensible to the length of the involved HBs, readily altered by applying pressure. This requires short hydrogen bonds $\text{O}-\text{H}\cdots\text{O}$ with lengths in the vicinity of the symmetrisation length around 2.39 \AA [29].

For instance, quantum paraelectricity is induced in squaric acid at a pressure of 3 GPa causing the compression of the short acceptor–donor distance of 2.55 \AA down to $\approx 2.45 \text{ \AA}$ i.e. near to the non-polar symmetric configuration $\text{O}\cdots\text{H}\cdots\text{O}$ [30]. In the same manner, ferroelectric ordering of protons is prevented in KDP by applying only 1.7 GPa [31]. Much higher pressures about 20 GPa are necessary to shorten the hydrogen bonding distance from $\approx 2.7 \text{ \AA}$ to $\approx 2.5 \text{ \AA}$ in the relatively rigid framework of goethite ($\alpha\text{-FeOOH}$) [32].

Nothing is known about the influence of pressure on the proton disorder in phosphatic oxyhydroxide compounds, exhibiting a more flexible framework with $(\text{OH})^-$,



(HOH), and O^{2-} ligands. For example, the eosphorite-childrenite solid solution minerals $\text{MAIPO}_4(\text{OH})_2\text{H}_2\text{O}$ ($\text{M} = \text{Mn}^{2+}$ and Fe^{2+}) are built with strongly distorted $\text{MO}_4(\text{OH}, \text{H}_2\text{O})_2$ and more regular $\text{AlO}_2(\text{OH})_2(\text{OH}, \text{H}_2\text{O})_2$ octahedra [33–35], as illustrated in Fig. 2.2. The structure crystallises in space group Cmce with unit cell metrics of $a \approx 6.9 \text{ \AA}$, $b \approx 10.4 \text{ \AA}$, and $c \approx 13.4 \text{ \AA}$ [21]. OH^- and H_2O groups are involved in various hydrogen bonds of which one has a particularly short length of $2.480(3) \text{ \AA}$ at ambient conditions.

Case study #2 (Cha. 9; Cha. 13 in Appendix) reported a remarkable temperature-dependent dielectric response of $\text{Mn}_{0.5}\text{Fe}_{0.5}\text{AlPO}_4(\text{OH})_2\text{H}_2\text{O}$. Being highly sensitive to low pressures below 1.6 GPa, the alteration of hydrogen bonds could be resolved. An anomaly around 70 K is peculiar in resembling those of antiferroelectric transitions. However, no excess heat is observed in heat capacity measurement aside from the anomaly recently related to the antiferromagnetic phase transition at around 7 K [21]. This is the first study of dielectric behaviour of short hydrogen bonds in phosphatic oxyhydroxides.

2.3. Hydrogen-bond network and ferrimagnetism in a rockbridgeite-type compound, $\text{Fe}^{2+}\text{Fe}_{3.2}^{3+}(\text{Mn}^{2+}, \text{Zn})_{0.8}(\text{PO}_4)_3(\text{OH})_{4.2}(\text{HOH})_{0.8}$

Rockbridgeite-type compounds are mixed-valence iron-bearing phosphatic oxyhydroxides with the idealized formula reported so far $\text{M}^{2+}\text{Fe}_4^{3+}(\text{PO}_4)_3(\text{OH})_5$ ($\text{M} = \text{Fe}, \text{Mn}, \text{Zn}$) [36–38].

Potential applications of $3d$ TM bearing oxyhydroxides as catalytic, energy, or sensor materials are motivated by their magnetic properties, as well as complex proton behaviours in various HB settings. Among the few studied phosphatic oxyhydroxides, barbosalite ($\text{Fe}^{2+}\text{Fe}_2^{3+}(\text{PO}_4)_2(\text{OH})_2$) [19, 39, 40] and eosphorite-childrenite series ($(\text{Fe}^{2+}, \text{Mn}^{2+})\text{AlPO}_4(\text{OH})\text{H}_2\text{O}$) [21] develop antiferromagnetic ordering at around

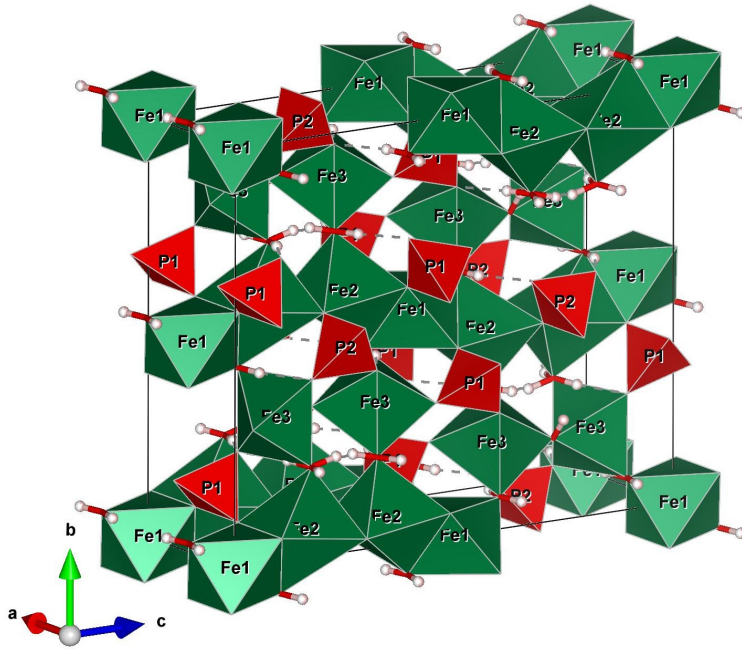


Fig. 2.3.: Structure of rockbridgeite-type minerals ($5.127(1) \times 13.971(2) \times 16.845(2) \text{ \AA}^3$) including the newly revealed hydrogen sites. Complicated linkage via corners, edges and faces of $[\text{FeO}_6]$ octahedra indicate complex magnetic interactions.

160 K and 7 K, respectively. As introduced in the previous Sec. 2.2, the latter showed a pressure-sensitive anomalous dielectric response related to small bond-length variations of short HBs [11]. The lipscombite-type compounds, $\text{Fe}^{2+}\text{Fe}_2^{3+}(\text{PO}_4)_2(\text{OH})_2$, develop magnetic ordering between 60 K and 90 K and are debated as electrochemically active materials [41, 42]. Previous investigations of rockbridgeite-type compounds focused on intervalence charge transfer in narrow mixed-valence pairs of $\text{Fe}^{2+}-\text{Fe}^{3+}$ [43, 44], and the selective CO oxidation catalyses in Pt-doped synthetic analogues [45]. In addition, a magnetic ordering was observed at 83 K, but its spin structure was not determined [44].

The structure of rockbridgeite-type series ($Cmcm$) was solved previously by diverse studies using X-ray diffraction techniques [36–38]: the structure topology encloses mixed valence corner-, edge-, and face sharing $\text{Fe}^{2+}/\text{Fe}^{3+}$ octahedra which are connected by rigid PO_4 tetrahedra (Fig. 2.3). These incomplete structure models missing hydrogen positions were complemented in the case study #3 using HRNPD (Cha. 10; Cha. 14 in Appendix): protons are statically disordered among four unique hydrogen sites building up a HBN similar to those of sulphite and selenite superprotonic conductors. Static and dynamic disorder of protons in OH and HOH give rise to proton-conductivity as indicated by the dramatically increasing dielectric response above RT. Furthermore, the ferrimagnetic spin structure occurring below T_c (81 - 83 K) was solved from analysis of the HRNPD pattern acquired at 25 K.

3. Applications of solid state ionic/protonic conductors

3.1. Ion batteries

Lithium ion batteries (LIBs) play a tremendous role in everyday consumer electronics, mobile devices, and the currently rapidly emerging electric vehicle market [47]. Furthermore, large scale energy storage systems are becoming indispensable to adapt to the fluctuating power supply by renewable solar and wind energy facilities [48]. Li-ion batteries are the main player in the field of rechargeable battery systems since their commercial introduction in the 1990s by *Sony* [49]. Though the development of Na-ion batteries (SIBs) commenced in the same time period from the 1970s - 1980s, LIBs were commercially established due to the rapid development of suitable battery materials [50]. Development of SIBs suffers from the significantly larger ionic radius of Na (1.02 Å) compared to Li⁺ (0.76 Å) hampering in particular intercalation in electrodes and ion transportation in electrolytes [51]. Furthermore, Na is heavier than Li by the factor of 3.3, hence, the energy density of SIBs will inevitably lag behind those of LIBs considering a fixed volume of battery systems. However, rich minable resources of Li are located in only few countries and their exploitation is expected to involve a skyrocketing Li retail price [50, 52, 53]. On the other hand, Na is the 6th most abundant element in the earth's crust and not reserved to few regions or countries [54]. In view of the rapid development of suitable electrolytes and electrode materials, SIBs are therefore highly promising candidates for the post-LIB-era which requires cost effective large-scale energy storage systems.

SIBs and LIBs are built up by the same key components (Fig. 3.1): Two electrodes are connected by an electrically insulating electrolyte material allowing the flow of charge carrier ions (Li⁺, Na⁺) from negative anode to positive cathode (discharge) and vice versa (charge). As positive charge carriers migrate, electric neutrality of the electrodes is maintained by a separate flow of electrons from anode to cathode driving an electric circuit (discharge). Electrodes typically consist of crystalline materials in which the Li⁺/Na⁺ ions are intercalated at non-occupied structural sites, such as in graphite Li_xC₆, or in A_{1-x}MO₂-type materials (A = Li/Na; M = 3d TM).

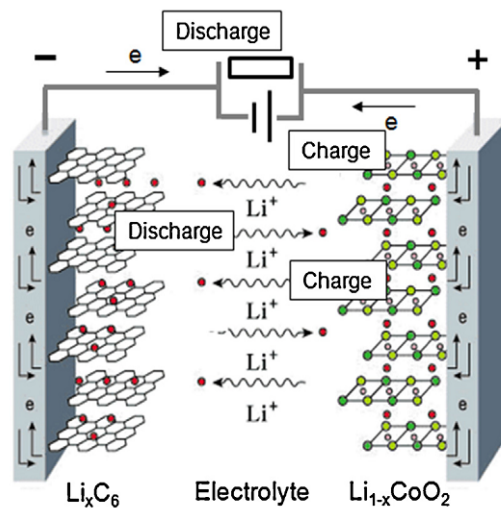


Fig. 3.1.: Schematic drawing of a rechargeable Li-ion cell. Li⁺ ions migrate through an ion conducting electrolyte between two electrodes. [46]

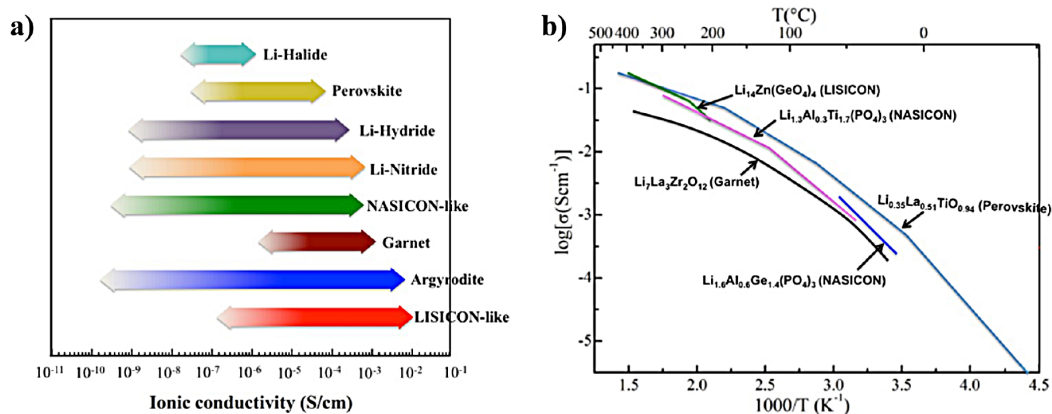


Fig. 3.2.: Ionic conductivities of several compounds at RT (a). Ionic conductivities of superionic conductors at $T \leq 500^\circ\text{C}$ (b). [4]

The electrolyte is basically a Li^+/Na^+ -ionic conductor which should fulfil the following requirements: chemically stable, electrochemically stable, thermally stable, high ionic conductivity ($10^{-1} - 10^{-3} \text{ S cm}^{-1}$ at RT), electrically insulating, and low toxicity [50, 55].

Solid electrolytes

Great effort is put into the development of 'all-solid-state' batteries, comprising not only solid electrodes, but also inorganic solid electrolytes [50, 56]. Commercial electrolytes are usually composed of organic polymers, salts or fluids with high conductivity values of up to $10^{-1} \text{ S cm}^{-1}$ at RT. These often toxic and flammable compounds constitute not only a security issue, but also favour the growth of Li/Na dendrites causing short-circuits and ultimately the death of the battery. These disadvantages are circumvented by inert solid electrolytes, being mechanically, chemically, and thermally stable over a broad electrochemical window. A large drawback has been the relatively low ionic conductivity of current solid electrolytes, barely reaching $10^{-2} \text{ S cm}^{-1}$ in LIBs, and $10^{-3} \text{ S cm}^{-1}$ in SIBs at RT [46]. As shown in Fig. 3.2, some of the promising candidates for the solid electrolyte are structures derived from natural minerals, such as garnet-, perovskite-, and argyrodite-type compounds. Some of the highest conductivity values in solid electrolytes for LIBs and SIBs were established with heavily defective LISICON and NASICON structures (Li/Na SuperIonic CONductor) (Fig. 3.2b). Only very recently, novel sulfur based solid electrolyte compounds exhibit highly promising RT Li^+ - and Na^+ -ionic conductivity values of $10^{-1} \text{ S cm}^{-1}$ and $10^{-2} \text{ S cm}^{-1}$, respectively [57, 58].

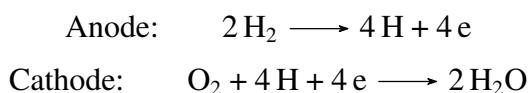
Offside consumer market demands, the development of battery materials for extreme temperature and chemical conditions requires highly stable electrolytes [59]. These compounds are investigated for exploratory basic research, but are demanded for long-term storage purposes [60]. Being stocked for several decades, such materials should exhibit negligible discharge and degradation at extreme temperature

conditions covering -40°C to $+70^{\circ}\text{C}$. In addition, they should be stable at operation temperatures about 670 - 870 K, with high conductivity values of at least $10^{-1} \text{ S cm}^{-1}$. As shown in one of the present case studies (Cha. 8; Cha. 12 in Appendix), cost-effective and ecologically friendly materials in this field may be developed on the basis of highly stable Li/Na bearing silicate materials, which can be synthesised at low temperatures.

3.2. Proton exchange membrane fuel cells (PEMFCs)

Similar to the field of classical cationic conductors, proton conduction in solid inorganic materials is of burgeoning interest. These materials are of immense technological concern for the application in hydrogen and oxygen sensors, membranes for water electrolyzers, but uttermost important for proton exchange membrane fuel cells (PEMFCs) [61]. Fuel cells have been renowned as a technology producing electrical energy from the reaction of oxygen with a hydrogen bearing fuel gas at high thermodynamic efficiencies [62]. Working at temperatures around 150°C , PEMFCs using light weight hydrogen fuel are particularly interesting for transportation purposes [63]: hydrogen possesses a high energy density and is processed with oxygen to H_2O at high conversion rates.

Fig. 3.3 illustrates the operation of a PEMFC built up by its main constituents, anode, electrolyte, cathode, and a electric current circuit. Energy is generated by the controlled processing of the highly exothermic oxyhydrogen reaction using catalyst coated electrodes ($\Delta\text{H} = -285.83 \text{ kJ per mol of H}_2$):



Hydrogen is split into protons and electrons at the anode. Protons migrate the electrolyte to reach the cathode where H_2O is catalytically formed with oxygen supplied by an air stream. The electrochemical cycle is completed by the flow of electrons from anode to cathode driving an electronic load.

Proton electrolytes in fuel cells

The conversion rate in FCs is dependent on easy proton transportation in the electrolyte transferring H^+ from anode to cathode. Previous studies revealed that hydrogen-bonding plays an important role for proton-conductivity [29, 64], meaning that structures with abundant, or easily formed hydrogen bonds are likely good proton conductors.

Amorphous *Nafion*, a perfluorinated sulfonated polymer (*Dupont de Nemours*), is the most widely used electrolyte membrane in FCs and has already been applied in the Gemini and Apollo space programs [61]. Despite its high proton conductivity of $10^{-2} \text{ S cm}^{-1}$, the large scale implementation of *Nafion* suffers from some major

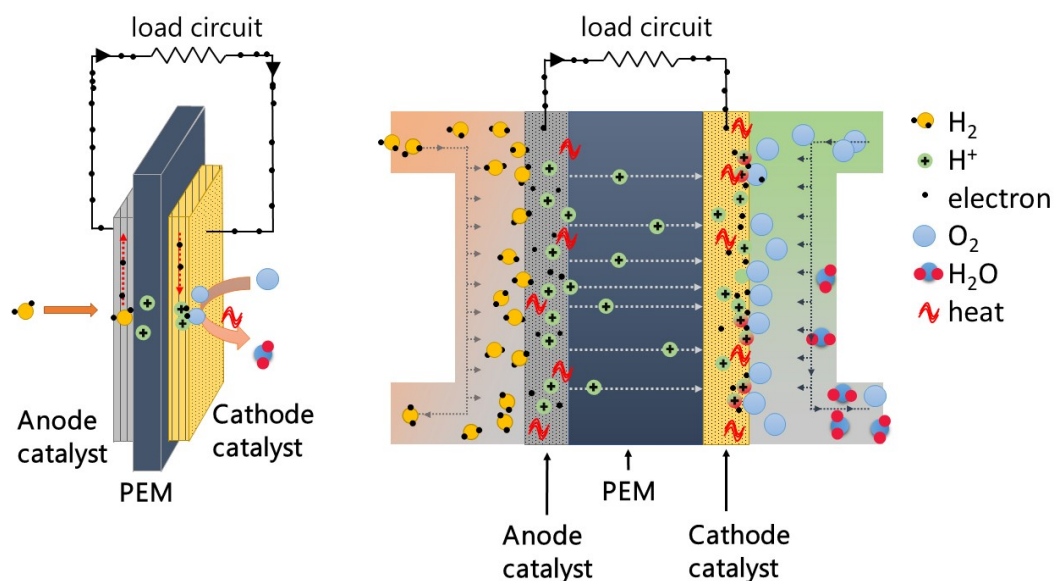


Fig. 3.3.: Graphic illustration of a proton exchange membrane fuel cell (PEMFC) in operating mode.

drawbacks [65]: *Nafion* is produced at high cost, dehydrates at around 80°C , thereby losing its proton conductivity, and only works at sufficiently high humidity. Therefore, large efforts were devoted to the development of more efficient and cheaper proton-conducting materials which should fulfil the following requirements [66, 67]: high proton conductivity with at least $10^{-2} \text{ S cm}^{-1}$ starting at below RT, good chemical stability in highly acidic media, thermal stability at low to medium temperatures ($\approx 150^{\circ}\text{C}$), low cost, and the ability to be processed into thin films.

There are multiple classes of proton conductors which provide sufficiently high proton conductivity, but lack at least one of the modern requirements [66, 68]. For example, amorphous solid acids, such as $\text{H}_3[\text{PMo}_{12}\text{O}_{40}] \cdot 29\text{H}_2\text{O}$ do show conductivity values up to $10^{-2} \text{ S cm}^{-1}$ between 0°C and 75°C but are easily dehydrated losing their conductivity [69].

Many of the recent approaches for innovative proton conductors focus on crystalline materials though. They encompass the substantial advantage of insights into proton conduction mechanisms using diffraction techniques, necessary for tailoring subtle conduction mechanisms.

A showcase type are perovskite-structured oxides reaching conductivities in the range of $10^{-1} \text{ S cm}^{-1}$ at temperatures higher than 300°C , but dropping rapidly approaching lower temperatures [70]. A disadvantage is the decomposition in the presence of CO_2 , SO_2 or H_2O gases, commonly occurring in FCs and water electrolyzers operating at high temperatures [71].

Another interesting group are $\text{MH}(\text{XO}_4)$, $\text{M}_3\text{H}(\text{XO}_4)_2$, $\text{M}_2\text{H}(\text{XO}_4)$ compounds, where M = alkali metal or NH_4 and X = S, Se, P, As [72]. Many of these sulfates and selenates are ferroelectric at low temperatures due to ordering of hydrogen atoms in hydrogen bond networks (HBNs). In addition they undergo first order phase tran-

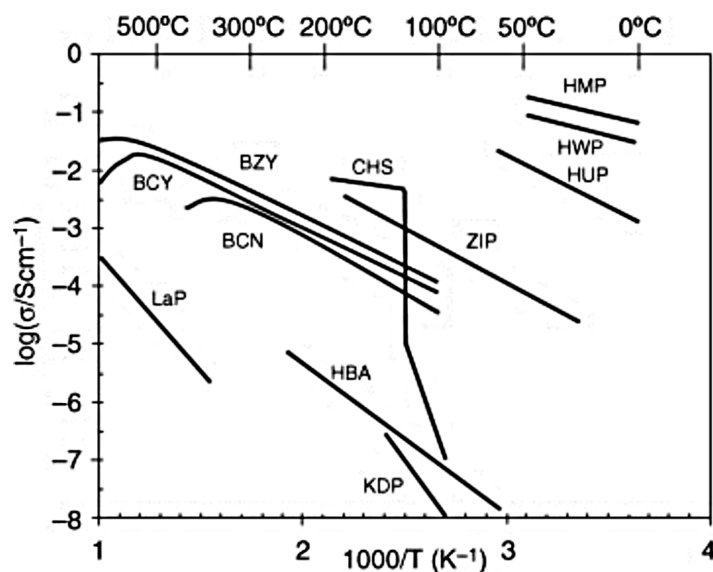


Fig. 3.4.: Overview of conductivities of inorganic solid proton conductors, showing a gap of compounds with high conductivity between 50 - 350°C. BCN: $\text{Ba}(\text{Ca}_{1.18}\text{Nb}_{1.82})\text{O}_9$; BCY: $\text{BaCe}_{0.9}\text{Y}_{0.01}\text{O}_{3-\delta}$; CHS: CsHSO_4 ; HBA: $(\text{H}_3\text{O})_2\text{Al}_{11}\text{O}_{17}$; HMP: $\text{H}_3[\text{PMo}_{12}\text{O}_{40}] \cdot 29\text{H}_2\text{O}$; HUP: $\text{H}_3\text{UO}_2\text{PO}_4 \cdot 4\text{H}_2\text{O}$; HWP: $\text{H}_3[\text{PW}_{12}\text{O}_{40}] \cdot 29\text{H}_2\text{O}$; KDP: KH_2PO_4 ; LaP: LaPO_4 ; SCY: $\text{SrCe}_{0.95}\text{YO}_{3-\delta}$; and ZrP: $\text{Zr}(\text{HPO}_4)_2 \cdot \text{H}_2\text{O}$. [68]

sitions between 80°C - 230°C involving a steep increase of proton conductivity by 2-3 magnitudes reaching values up to $10^{-1} \text{ S cm}^{-1}$. In these superprotonic states, protons become highly disordered within the HBN [73]. However these compounds are impractical for FC application due to their water-solubility and the tendency of SO_4 oxidation by hydrogen [68].

Only recently, significant advances were achieved with metal-organic-frameworks (MOFs) and closely related porous structures [74, 75]. High framework tunability and tolerance towards vehicular guest molecules carrying protons give rise to conductivity values of up to $10^{-2} \text{ S cm}^{-1}$ between RT and 150°C. A major challenge in this field remains in this poor thermal and chemical stability, as well as in the processibility [67].

As noticed by various authors [68, 76], there exists a gap of stable inorganic solids with high proton conductivity between 200°C and 350°C. A class of materials which could fill the gap, but has been largely disregarded in the context of proton conduction, are oxyhydroxides. Typically, these compounds are thermally less stable than pure oxides, but more stable than amorphous or organic proton conductors. Boehmite, $\gamma\text{-AlOOH}$, is the first oxyhydroxide suggested as a highly suitable electrolyte material for PEMFCs with a predicted high proton conductivity at low energy barriers between RT and 400°C [66, 77]. The structural key for proton conductivity in $\gamma\text{-AlOOH}$ lies in HBs connected to one another forming an infinite HBN.

Further candidates are likely found in the pool of phosphatic oxyhydroxides containing HBNs in mixed TO frameworks impervious to dehydration up to temperatures

of 350°C [18, 21, 78, 79]. For instance, intense proton disorder in local clusters of hydrogen bonds was resolved via neutron single crystal diffraction of the eosphorite-childrenite series, $(\text{Mn,Fe})^{2+}\text{AlPO}_4(\text{OH})_2\text{H}_2\text{O}$ [80]. Another interesting candidate with superprotonic behaviour for a highly disordered HBN is the rockbridgeite-type series, as shown by one of the case studies (Cha. 10; Cha. 14 in Appendix). A large variety of phosphatic oxyhydroxide structures is available and may provide further interesting novel electrolyte materials for PEMFC applications.

Part II.

Theoretical background

4. Ionic conduction and disorder phenomena in inorganic solids

4.1. Defects driving ionic conductivity

Ionic conductivity is referred to as the process of ions migrating a framework sublattice through vacant or interstitial sites at equal or similar energy with respect to the original site of the ion [81].

The mobility of ions is adherently dependent on the presence of structural defects providing partially unoccupied sites in the framework structure [81–83]. In real crystal structures at $T > 0$ K, the quasi-infinite periodic arrangements of atoms is interspersed with thermodynamically inherent point defects [84].

Most solids comprise *Schottky defects* which correspond to the coupled formation of cation and anion vacancy pairs. As shown in Fig. 4.1a, the vacancy-driven mechanism of cationic conduction is based on the re-occupation of vacancies by hopping of adjacent ions with similar bonding affinity. *Schottky defects* can be engineered by aliovalent substitutions during crystal growth. For example, replacing Ag^+ by Cd^{2+} in AgCl creates a vacancy at a Ag site for bulk electro neutrality, which is then available for surrounding mobile Ag^+ ions [85].

The interstitial mechanism on the other hand is described in terms of *Frenkel defects*. Usually unoccupied structural sites, i.e. interstitial sites in the crystal structure, can be occupied by ions in the vicinity with suitable bonding preference. Interstitial sites inherit a higher ionic energy compared to regular sites (Fig. 4.1b), making a long-term residence of a mobile ion less probable [86].

The comprehensive description of conduction paths in ionic conductors includes both mechanisms, i.e. ions migrate from framework sites to interstitial sites and vice versa [86]. Much like in electronic insulators, ionic energies of regular and interstitial sites are separated by an intrinsic energy gap ΔH_g (Fig. 4.2) [87]. Ions can hop to interstitial sites of higher ionic energy if thermal activation is supplied. Especially in crystalline solid electrolytes, a cooperative ion avalanche motion is triggered ions hopping from regular to interstitial sites [88].

As shown in Fig. 4.2, the respective abundances of Frenkel and Schottky defects are of high significance for ionic conductivity. As the defect density increases, energies of regular and interstitial sites are approaching ($\Delta H_g = 0$ J) to an intermediate level reflecting structural relaxation processes [87]. Hence, ΔH_g can be engineered by the density of defects in the structure, e.g. in the case of NASICON superionic conductors [83].

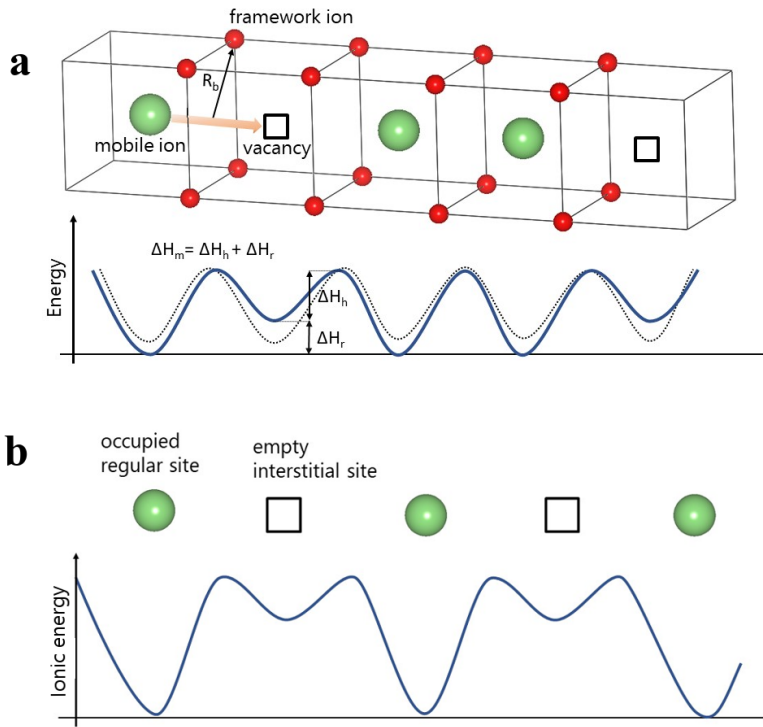


Fig. 4.1.: Site exchanging of ions with radius R_b towards vacant regular lattice sites (a). Motional enthalpy ΔH_m contains terms related to hopping process (ΔH_h), e.g. bottleneck-geometries, and for post exchange lattice relaxations (ΔH_r). Interstitial sites of higher ionic energy provide short term transitional residence for ions migrating from one regular site to another (b). Figures are illustrated according to Ref. [86]

4.2. Hopping model: ionic conduction in bulk crystals

Ionic conduction through solids is described by thermally activated hopping of ions through a framework via defects. The total electric conductivity of a solid is given by the sum of partial conductivities of ionic and electronic charge carriers:

$$\sigma = \sum_{i=1} q_i u_i c_i \quad (4.1)$$

where: σ = sum of partial conductivities of ionic and electronic charge carriers [S cm^{-1}]

q_i = charge of charge carrier [C]

u_i = mobility of charge carrier [$\text{cm}^2 \text{s}^{-1} \text{V}^{-1}$]

c_i = concentration of charge carrier [cm^{-3}]

From Eq. 4.1 it becomes obvious that conductivity may be tuned by increasing concentration of charge carriers and their respective mobilities. Under the presumption of Boltzmann statistics, the diffusion of ions through a sublattice is then expressed by:

$$D_i = \gamma a^2 \nu_0 e^{\frac{-\Delta G_{migr}}{kT}} \quad (4.2)$$

where: D_i

= Diffusion coefficient of an ion i

γ = factor for geometrical and correlation effects

a = hopping distance [m]

ν_0 = hopping attempt frequency [s^{-1}]

$\Delta G_{migr} = \Delta H_{migr} - T\Delta S_{migr}$ = Gibbs free energy of migration

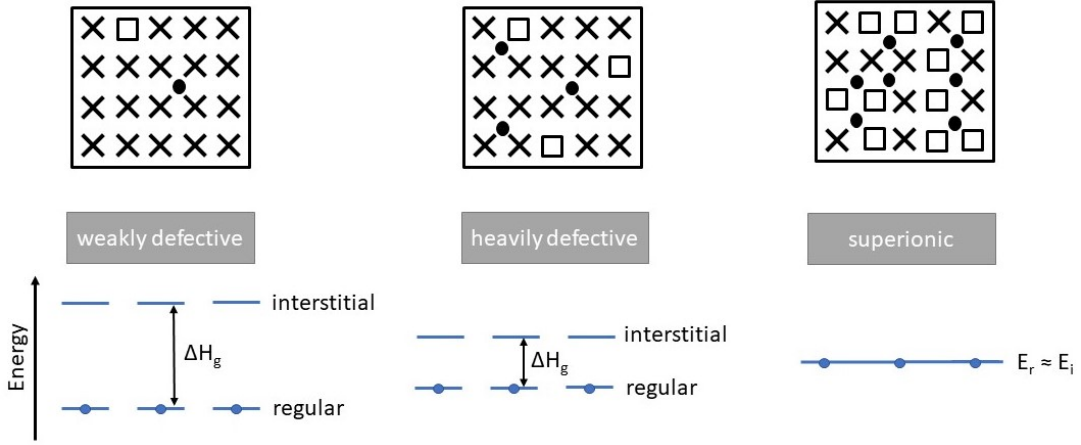


Fig. 4.2.: Schematic crystal lattice with point defects at charge carrier sites (X: regular lattice site; □: vacancy; ●: interstitial site). Intrinsic gap ΔH_g between energies of regular sites (E_r) and interstitial sites (E_i) is reduced with increasing defect density leading to superionic conductors with $E_r = E_i$. The figure is illustrated according to Ref. [87]

γ includes geometrical and correlation effects taking into account the difference in hopping probability for solitary and cooperative motion of ions. For solids, ν_0 lies in the range of 10^{13} hopping attempts per second and is mostly set equal to the Debye frequency. ΔH_{migr} determines the temperature dependence of ionic mobility and is usually between 0.2 and 2 eV in solid ionic conductors [89].

The diffusivity of an ion can be linked to the ionic mobility using *Nernst-Einstein equation*:

$$u_i = \frac{D_i q_i}{kT} \quad (4.3)$$

Combining Eq. 4.1, 4.2, and 4.3 the ionic conductivity can thus be expressed by:

$$\sigma_{ion} = \frac{q_i^2}{kT} c_i \gamma a^2 \nu_0 e^{-\frac{\Delta S_{migr}}{k}} e^{-\frac{\Delta H_{migr}}{kT}} \quad (4.4)$$

Usually Eq. 4.4 is simplified as a function of the activation energy ΔH_{act} using an exponential prefactor:

$$\sigma_{ion} = \frac{\sigma_0}{T} e^{-\frac{\Delta H_{act}}{kT}} \quad (4.5)$$

In practice, σ_{ion} values are obtained experimentally at several temperatures, and ΔH_{act} can be inferred from the slope of an Arrhenius plot $\ln(\sigma_{ion} T)$ vs $1/T$. ΔH_{act} reflects the potential barrier ions and the local framework lattice face over the course of an ionic site exchange. As illustrated in Fig. 4.1a, it is composed of a barrier height the ions need to overcome when moving from on to an adjacent site (ΔH_h), as well as a relaxational enthalpy (ΔH_r) reflecting framework relaxations due to the ion shifts [86]:

$$\Delta H_{act} = \Delta H_h + \Delta H_r \quad (4.6)$$

Among several others, ΔH_h depends on intuitive factors [81, 83]: (i) the radius of mobile ion R_b , as well as framework ions which build up a structural bottleneck for the conduction pathways indicated as simple planar frames in Fig. 4.1a (ii) thermal at-site motion of the mobile ion facilitating a site exchange in a certain direction (iii) thermal at-site motion of framework ions widening the structural bottleneck.

The relaxation enthalpy ΔH_r on the other hand is the energy which needs to be supplied to level the energy of the acceptor site to the one of the donor site [86]. This is necessary since the hopping process takes relatively long time compared to that immobile framework ions require to relax in their equilibrium positions, which is different for empty or occupied sites of mobile ions (Fig. 4.1a).

In conclusion, ΔH_h is minimized by a smaller ionic radius R_b of a mobile ion passing a narrow bottleneck (Fig. 4.1a), whereas ΔH_r relies on suitable ionic radii of the mobile ion to fit the coordination of the new site. This incompatible scheme illustrates well that interstitial sites have higher ionic energy compared to vacancies as shown in Fig. 4.1b & 4.2). Interstitials are usually larger or smaller compared to relaxed regular sites of appropriate size for the mobile ion, and therefore increase ΔH_r in the motion enthalpy [86].

It should be noted that structures with high free volume do not stringently provide higher conductivity values [68]: The most impelling factor for ionic conduction is the polarisability of the mobile ion. The higher the polarisability, the more soft and deformable behaves the ion during an intermediate valence in the non-bonded transfer process. For example, Na^+ is more polarisable than Li^+ for its larger radius and higher number of electrons. On the other hand, Li^+ is highly polarising. Its strong attraction of framework anions might cause the trapping of Li^+ in narrow topological sites.

As outlined in Sec. 7.4.2, the conductivity σ [S cm^{-1}] is evaluated from resistivity values [$\Omega \text{ cm}$] measured at various temperatures using impedance spectroscopic methods. The above explanations point out that conductivity and activation energy can be optimized by structural investigations and defect engineering. Ion conductors are then optimised by varying the bottleneck geometries or increasing the density of mobile ions/defects, e.g. through aliovalent substitutions in the framework structure. Structural investigations using X-ray/neutron diffraction methods are essential for the characterisation of geometrical constrictions, as well as for detection of conduction pathways and interstitial sites via ΔF synthesis (see Sec. 7.5). Furthermore, at-site motions of mobile cations are resolvable by anisotropic ADPs (atomic displacement parameters) and PDF (pair distribution function) analysis, being highly valuable indicators for the preferred direction of charge diffusion in ionic conductors.

5. Hydrogen bonds and proton dynamics in the solid state

Hydrogen bonds are vital structural constituents in almost all material science subclasses, reaching from supramolecular chemistry, polymer chemistry, biochemistry to mineralogy and pharmacy-relevant applications. Hydrogen bonding is investigated for the involvement in manifold material properties, e.g. order-disorder (anti-)ferroelectric transitions, quantum critical hydrogen tunnelling phenomena, and protonic conductivity. In oxide and oxyhydroxide structures, HBs are established among oxygen atoms of suitable distance providing a substantial contribution to structural stability. Hydrogen bonds are described by the local molecular configuration $X-H\cdots A$ where the group $X-H$ is called the proton donor, and A the proton acceptor. H shares its sole electron forming a covalent bond with the more electronegative X , making $X^{\delta-}-H^{\delta+}$ immanently polar. The partial positive charge at H can attract ions $A^{\delta-}$ with sterically available negative charge for example from lone-pair electrons, as illustrated for the simplest case of water in Fig. 5.1. In the resulting intermolecular $H\cdots O_A$ interaction, the distance d between H and O_A is found to be about 1 \AA shorter than the sum of their van-der-Waals ionic radii (r_{vdW} : $H = 1.1 \text{ \AA}$; $O = 1.52 \text{ \AA}$) [90] indicating a significant overlap of electron orbitals [29]. Depending on the distance, the bond character established within $H\cdots A$ can contain terms of electrostatic, covalent, ionic, but also repulsive interactions [91]. Similar to the classical case $O_D-H\cdots O_A$, a large variety of atoms and groups are known as proton donors and acceptors, e.g. $X = O-H, N^+-OH, S-OH, P-OH, TM-OH$; $A = O, -OH, P-O^-, P-OH, F^-, TM-O^-$ [29].

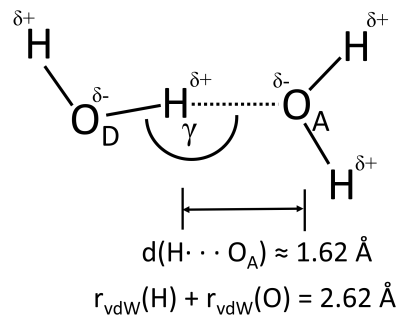


Fig. 5.1.: Prototype of a water dimer where $d < r_{vdW}(H) + r_{vdW}(O)$ indicating bonding interaction via electron orbital overlap of H and O_A ; ($\gamma = \angle(O_D-H-O_A)$)

Table 5.1.: Classification of hydrogen bond strengths by means of guided values for bond geometry [92]. (d = distance; $\gamma = \angle(\text{X-H-A})$)

	Strong	Moderate	Weak
interaction type	strongly covalent	mostly electrostatic	electrostatic dispersed
$d(\text{H}\cdots\text{A})$ [Å]	1.2 – 1.5	1.5 – 2.2	> 2.2
$D = d(\text{X}\cdots\text{A})$ [Å]	2.2 – 2.5	2.5 – 3.2	> 3.2
$d(\text{X-H})$ vs $d(\text{H}\cdots\text{A})$	$d(\text{X-H}) \approx d(\text{H}\cdots\text{A})$	$d(\text{X-H}) < d(\text{H}\cdots\text{A})$	$d(\text{X-H}) \ll d(\text{H}\cdots\text{A})$
γ [°]	170 – 180	> 130	> 90
E_{bond} [kcal/mol]	15 – 40	4 – 15	< 4

5.1. The hydrogen bond - an incipient proton transfer reaction

Proton transfer within HBs is the vital basis for proton conducting mechanisms and (anti-)ferroelectric proton order-disorder transitions [64, 68]. The hydrogen bond can be regarded as an incipient proton transfer reaction, where with increasing strength of the HB, the transfer is more well-advanced [29]. Hence, it is necessary to discuss the classification of HBs in classes of strong to weak bonds.

As briefly touched afore, HB interaction strengths are broadly categorised by means of geometrical parameters, namely the distances $d(\text{H}\cdots\text{A})$, $d(\text{X-H})$, and $D = d(\text{X}\cdots\text{A})$, as well as the angle $\gamma = \angle(\text{X-H-A})$ [29]. A large variety of bond strengths (2 - 40 kcal/mol) are described for HBs, reflecting the large diversity of this bond type with strong correlation to their geometries (Tab. 5.1) [92]:

Modern definitions include HBs with D values up to 3.0 - 3.2 Å and a lower angular cutoff of $\gamma > 90^\circ$. Weaker electrostatic interactions between donor group and acceptor are dominant in longer and weaker HBs ($d(\text{H}\cdots\text{A}) > 1.5$ Å) since electrostatic interaction drops relatively slow with distance (r^{-3}). The same accounts for deviations of the optimal geometry, i.e. $\angle(\text{X-H-A}) = 180^\circ$. As a rule of thumb, covalent bonds and repulsive forces are strong in short hydrogen bonds, the former dropping by e^{-r} with increasing distance, and the latter increasing rapidly by r^{12} in very short distances below $d(\text{H}\cdots\text{A}) = 1.2$ Å.

The strength of HBs and accordingly the probability of a proton transfer is readily visualized in corresponding energy-well potentials [93] (Fig. 5.2). Classical HBs are described by an asymmetric double well potential in which H is trapped in the donor-group (Fig. 5.2a). Regarding donor and acceptor groups as Brønstedt acids, the potential difference is furthermore proportional to their respective (logarithmic) *acid dissociation constant* pK_a [93]. Preferred dissociation of the proton is expressed by a lower pK_a value, whereas a higher value reflects higher proton affinity. Hence, the pronounced disparity of the local minima in moderately strong ($D = 2.5 - 3.2$ Å) to weak ($D = 3.0 - 3.2$ Å) HBs reflects a lower probability of proton transfer reaction from donor to acceptor.

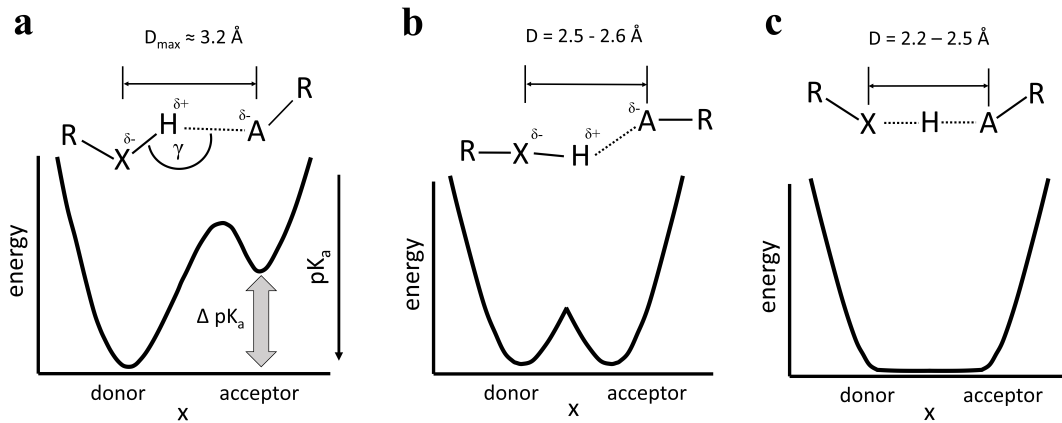


Fig. 5.2.: Different types of HBs [92]: (a) weak to moderately strong HBs with classical asymmetrical energy potential and higher proton affinity, i.e. high pK_a , at the donor moiety (b) moderately strong HBs with facile proton transfer reaction through similar proton affinities (pK_a) and energy potentials at narrow donor/acceptor groups (*low barrier HBs*); (c) *very short* hydrogen bonds with a single potential well, where the extreme example of a symmetric HB is indicated on top. $d = H \cdots A$; $D = X \cdots A$; $\gamma = \angle(X-H-A)$; r_{vdW} are taken from Ref. [90]. Figures are illustrated according to Ref. [93].

A transition to a symmetric double well occurs at the shorter bound of moderately strong HBs with $D = 2.5 - 2.6 \text{ \AA}$ valid for donor and acceptor groups of very uniform pK_a (Fig. 5.2b). Hydrogen transfer in these *low barrier HBs* is considerably facilitated for the short barrier height and the homogeneous energy potentials.

On the extreme, there are *very short* and strong HBs approaching a length of $D = 2.2 - 2.5 \text{ \AA}$ (Fig. 5.2c). The abbreviation and increased bond strength of $H \cdots A$ is reflected in the approximation of the distances between H and A, as well as H and X the latter being increased from its usual bond length (Tab. 5.1). In this case, H is equally favourably hosted by donor and acceptor groups which makes them indistinguishable. In case of oxygen as acceptor and donor, HBs can be as short as $D_{min} \approx 2.39 \text{ \AA}$ with $\angle(O_D-H-O_A) \approx 170 - 180^\circ$ [29]. In such symmetrical HB configuration $O \cdots H \cdots O$, oxygens are equally distanced to H under the formation of two equivalently strong and mostly covalent bonds [29]. Thereby, proton transfer in the HB is permanently accomplished and the proton is fastened under the loss of polarisation and polarisability of the HB.

As pointed out in the following sections, the ease with which proton transfer reactions proceed depicts a critical parameter for various phenomena: Low barrier proton transfer reactions are characteristic for short HBs. However, protons may get trapped in strong HBs making them unavailable for long range proton conductivity. On the other hand, (anti-)ferroelectric order-disorder transitions require sufficiently short but still asymmetric HBs such that concerted proton transfer can induce a stable polar state. The ordering process can effectively be suppressed by compressing short HBs to a near symmetrical non-polar configuration.

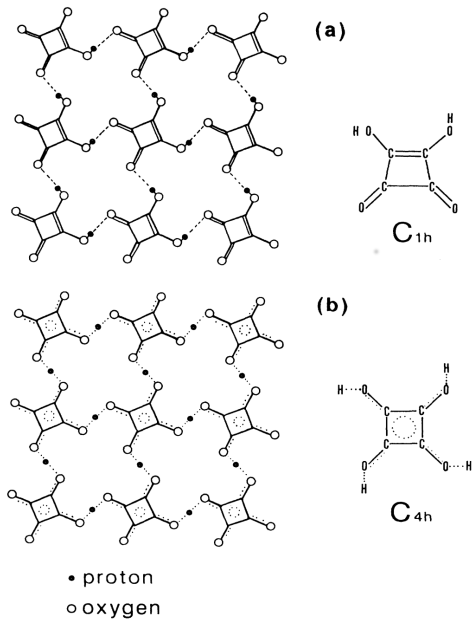


Fig. 5.3.: (*a-b*) plane of squaric acid ($\text{H}_2\text{C}_4\text{O}_4$) structure below T_N (**a**) showing asymmetrically ordered protons in the HBN giving rise to a planar polarisation. The antiferroelectric order can be suppressed (**b**) by application of pressure (≈ 3 GPa) symmetrising the HBs under the loss of their polar character (*quantum paraelectric state*). [30]

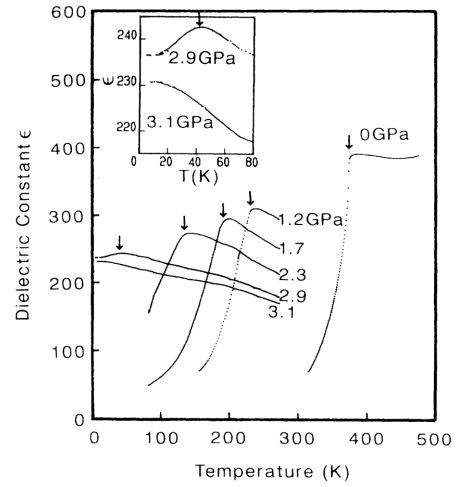


Fig. 5.4.: Dielectric response isobars of squaric acid indicate the shift of T_N towards lower temperatures, associated with a inhibiting of proton ordering by shortening of very short HBs (see also Fig. 5.3). [30]

5.2. Polarisability and order-disorder phenomena in hydrogen bonds

Polarisation from asymmetric HBs and the ease of proton transfer reactions depending on their length is exemplified in hydrogen bonded (anti-)ferroelectrics. There are several compounds undergoing such order-disorder (anti-)ferroelectric transitions under concerted ordering of protons within HBs, such as KDP (KH_2PO_4), squaric acid ($\text{H}_2\text{C}_4\text{O}_4$), or mono-protonated diazabicyclo[2.2.2]octane (HdabcoH⁺) derivatives [7, 28]. Below the 'lock-in' transition temperature, protons order within HBs under the formation of a long range order of HB dipoles establishing a net (anti-)ferroelectric polarisation.

A showcase compound is squaric acid ($\text{H}_2\text{C}_4\text{O}_4$), where below $T_N \approx 370$ K protons order anti-phase wise in a HBN parallel to the (*a-b*) plane (Fig. 5.3a), while the squaric C_4 rings adopt a non-centrosymmetric arrangement in the HBN plane [31]. Very short HBs with lengths close to the symmetrisation length of ≈ 2.40 Å are considered as a prerequisite for spontaneous ordering due to proton transfer in a low barrier double well potential. Interestingly, by applying isostatic pressure T_N is tuned towards lower temperatures (Fig. 5.4) [30]. This was explained by the compression

of HBs, i.e. length D , whereby the freezing point of proton transfer reactions is shifted towards lower temperatures prohibiting the lock-in of protons within their *low barrier HBs*. Once the pressure is high enough, HBs are symmetrised losing their polar character and antiferroelectric ordering is suppressed even at 0 K (Fig. 5.3b). Similar observations were obtained with other hydrogen bonded (anti-)ferroelectrics, such as KDP-type structures [94–96].

Such dielectric response of hydrogen bonded antiferroelectrics as shown in Fig. 5.4, reflects the feasibility of the applied alternating electric field to shift the protons within their HBs [97]. Once protons are locked-in, the structure loses its polarisability and the real part dielectric permittivity drops rapidly. However, as shown by one of the case studies (Cha. 9; Cha. 13 in Appendix), such supposedly typical anomalies may be misleading. Very similar dielectric response curves could be attributed to electric field stimulated proton transfer reactions in very short HBs in the absence of a phase transition.

5.3. Proton conductivity in non-metallic solids

The electronic characteristics of protons are peculiar [61]: with its sole valence electron lost, the proton is outstandingly small, light, and polarising, causing strong interactions with its immediate surrounding. Other than charge carrier ions such as Ag^+ , K^+ , Na^+ , and Li^+ , the small proton free of electrons is able to connect with the valence shell of anions realising a very strong interaction [98]. In the case of oxides, the bond strength is emphasised regarding the short bonding distance of only 0.984 \AA between O and H, considering that the radius of oxygen is about 1.4 \AA [99]. Thus, a classical site hopping from one crystallographic site to another, which involves the break-up of O–H bonds, depicts a highly unlikely conduction mechanism for protons [68, 98]

In non-metallic materials with either large volume of free space in the atomic lattice, or with a pervading HBN, there are two broadly accepted mechanisms for long range proton conduction [68, 98]:

- i)* In the *vehicular mechanism* the proton is transferred to carrier molecules such as H_2O or NH_3 acting as transport vehicles. The long range conduction is limited to layered or porous structures allowing flow and counterflow of the carrier molecules.
- ii)* The *Grotthuß mechanism* was originally applied to explain the high electric conductivity in water, but has been extended to hydrogen bonded salt structures, as well as to *3d* TM bearing oxides and oxyhydroxides where protons are constituents of OH and HOH groups occupying oxygen sites. The mechanism describes a two step process, in which a proton is first transferred to an acceptor followed by reorientation of the local environment. The reorientation process establishes new bonding opportunities for the as-transferred proton in preparation for the next step, required for long range proton conduction.

A simplistic scheme of this mechanism with rotational reorientation of OH groups and proton transfer through establishing and subsequent dispersion of HBs is illustrated in Fig. 5.5 for perovskite type structures.

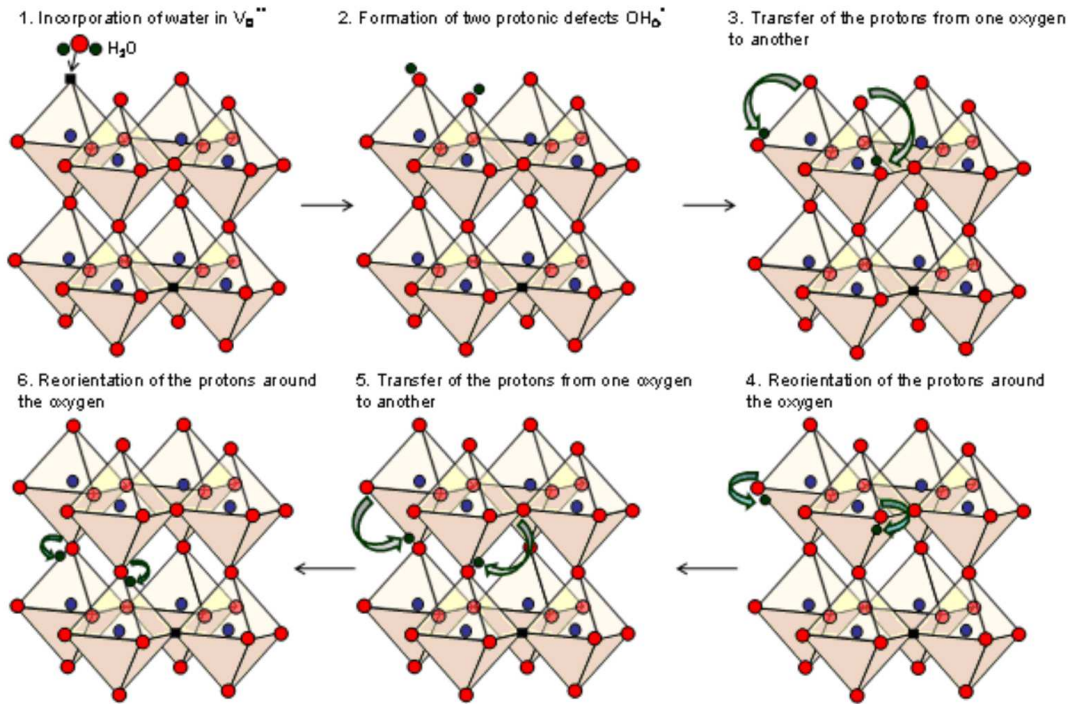


Fig. 5.5.: Schematic mechanism for water incorporation at defective oxygen sites (black square) and proton transport via the *Grotthuss mechanism* in high temperature perovskite proton conductors. (dark green circles: proton; red circles: oxygen; dark blue circles: cations at *B* site) [100]

Regardless of the conduction mechanisms, proton transfer reactions in HBs play a key role [64, 68, 101]. The bond strength of the HB is ambiguous [102]: strong hydrogen bonds are favourable for a rapid proton transfer reaction. However, the high bond strength impedes structural reorientation.

This ambiguity is illustrated in the theoretical model of a basic H_5O_2 donor/acceptor system with $D = 3 \text{ \AA}$ (Fig. 5.6) [101]. The bond energy E_{bond} equals the barrier energy $\Delta E_{\text{barrier}}$ at 1 eV, indicating breaking of the O–H bond. However, E_A of proton conduction in bulk water is found in the range of 0.1 eV. The huge energy difference is ascribed to many particles interaction in bulk water, significantly reducing energy barrier for proton transfer, e.g. through reorientations of surrounding water molecules.

Proton conduction in other solvents, for example oxide or salt lattices, similarly includes many particle interactions which enable long range proton transfer through

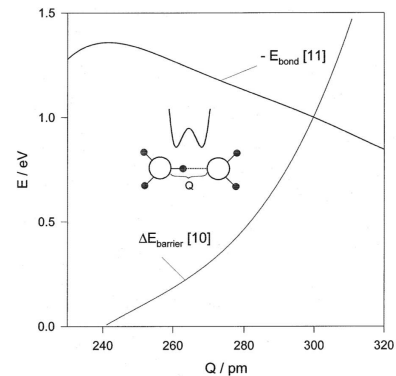


Fig. 5.6.: Theoretical curves for hydrogen bond energy (E_{bond}) and energy barrier ($\Delta E_{\text{barrier}}$) for proton transfer in an isolated H_5O_2 dimer. [101] and Ref. [10,11] therein;

short (strong) HBs by lowering the energy barrier [101]. These processes are linked to the mutual interplay of hydrogen bonding with site defects at oxygen and $3d$ TM cation sites including strong covalent and ionic bonds, as well as repulsive forces. For instance, the role of these complex interactions is illustrated for BaCeO_3 in Fig. 5.7 extending the simplistic *Grotthuß mechanism* shown in Fig. 5.5 to a more detailed picture of hydrogen streaming along oxide frameworks [103, 104]: The proton defect in the central OH group of two $[\text{Ce}(\text{O},\text{OH})_6]$ octahedra shows rotational disorder attracting eight adjacent oxygen atoms which are shifted on average by forming transient HBs (Fig. 5.7a). In an instant, a strong HB ($D = 2.8 \text{ \AA}$) is formed with one of these oxygens causing heavy distortion by O-Ce-O bending (Fig. 5.7b). As the strong covalent bonds of Ce to donor and acceptor oxygen atoms become elongated, the straightening of the HB opening angle enhances proton transfer probability. After the proton transfer within the HB is accomplished, the framework undergoes relaxation and reorientation. The proton rotates about its new host oxygen atom, initiating the next transfer procedure.

Other than for perovskites, where OH defects are extrinsically introduced, plenty compounds exhibit structure inherent HBNs enabling proton conduction. A prominent example is CsHSO_4 (Fig. 5.8) which undergoes a transition to a superprotonic state at 414 K reaching conductivities up to $10^{-2} \text{ S cm}^{-1}$ [105]. Above the transition temperature, disordered protons and fast rotations of hydrogen bonded HSO_4 tetrahedra realise a *dynamically disordered hydrogen bond network (DDHBN)* [106]. Fast 3D proton conductivity is established by a permanently changing HBN of ceasing and reorienting HBs. The structure contains basically isolated chains of hydrogen bonded HSO_4 tetrahedra running in [001]. Protons are easily transferred back and forth intra-bond wise within the chains (Fig. 5.9a).

Ab initio models indicated a mechanism where the proton transfer at one side of a HSO_4 tetrahedron facilitates its subsequent rotation [105]. Thereby a new HB is realised in which the proton is readily transferred to a formerly detached chain (Fig. 5.9b). Both *Grotthuß* segments, i.e. rotation and proton transfer, act in the same time scale. A rate limiting step are rather angular HB reorientations in the absence of rotation defects (Fig. 5.9c).

Despite some similarities, the above examples indicate that the distinct mechanism of proton conduction is usually of higher complexity compared to cationic conduction using the classical hopping model (Sec. 4). Obviously, unique crystal structure topologies demand careful investigation of transfer and reorientation phases includ-

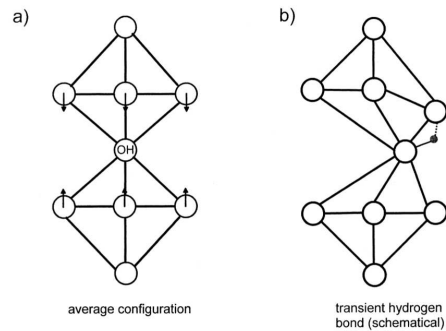


Fig. 5.7.: Proton transfer along octahedral edges in perovskites: an average transitional state of attracted oxygens around OH defects (a) is followed by an instant formation of a HB transferring the proton to an adjacent oxygen (b). [101]

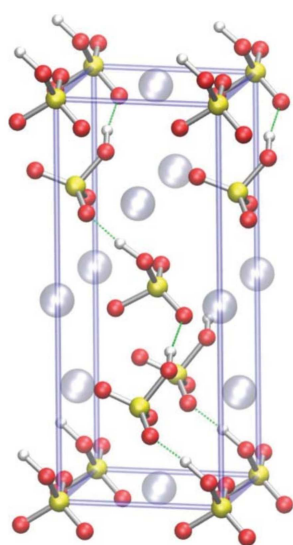


Fig. 5.8.: Structure of the superprotonic phase of CsHSO_4 with infinite chains of HSO_4 tetrahedra connected via HBs (dashed green lines). (H = white, O = red, S = yellow, Cs = grey) [105]

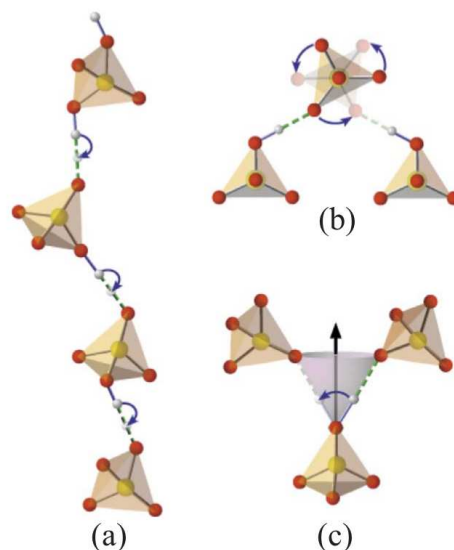


Fig. 5.9.: (a) Illustration of a sequence of proton transfer reaction in HBs initiated by a H_2SO_4 defect in the uppermost tetrahedron. Dynamically disordered HBN are created by reorientations of HBs connecting formerly isolated HBN, introduced by the rotation of HSO_4 tetrahedron (b), or by a hydrogen bond twist with static HSO_4 tetrahedron (c). (Colour scheme following Fig. 5.8) [105]

ing many particle interactions to explain the underlying mechanism. Eq. 4.1 - 4.5 are in fact applicable for proton conduction, but access to the contributions of activation enthalpy due to these complex processes are more challenging [68, 98]. In this sense, the so far poorly investigated proton conduction in phosphatic oxyhydroxides constitutes an interesting research subject as indicated in one of the case studies treating a rockbridgeite-type compound (Cha. 10; Cha. 14 in Appendix). These compounds combine a highly disordered HBN comparable to the one in CsHSO_4 , with a TO topology the like of oxide conductors, e.g. perovskites.

6. Magnetic interactions in 3d TM oxides and oxyhydroxides

6.1. Magnetic moments

Macroscopic magnetism in 3d TM bearing oxyhydroxide and oxide structures rests on interaction of magnetic moments from ions with partially filled 3d orbitals distributed periodically in the crystal lattice. Once a critically low temperature is reached, interaction among sufficiently narrow magnetic moments may exceed their thermal fluctuations. A spontaneous long range order of magnetic moments gives rise to a first order ferro-, antiferro-, or ferrimagnetic phase transition.

The magnetism of free ions derives from angular momenta of unpaired electrons in partially filled orbitals, e.g. in 3d or 4f subshells. The magnetic moment of an electron is composed of the angular momenta of its orbital movement, as well as of its intrinsic angular momentum, the electron spin. The momenta are described in terms of the respective quantum numbers m_l and m_s , which according to the *Pauli principle*, may not be equal for two electrons in the same orbital. There are two possible spin states usually described with \uparrow and \downarrow . In fully occupied subshells, where each orbital is filled with paired electrons, one of \uparrow and the other of \downarrow spin state, the magnetic moment is cancelled out, i.e. in $1s^2$, $2s^2$, $2p^6$ etc..

3d TM ions contain partially filled 3d orbitals. The strong intraionic exchange ($J_H = 1.0 - 2.0$ eV) [3] links electron spins in the same subshell to maximise the total ionic spin, following *Hund's first rule*. Accordingly, half occupied 3d orbitals are filled mainly by electrons with spins of the same state. The intraionic spin coupling gives rise to the ionic magnetic moment, of which the strength depends on the number of unpaired electrons in the 3d orbital (Tab. 6.1). As pointed out in the next section, the vast majority of magnetic ground states in oxides is established by indirect in-

Table 6.1.: Electron occupation of selected 3d TM cations and their spin-only magnetic moments.

3d TM	electr. configuration	orbital spins	spin only moment [μ_B]
V ³⁺	[Ar] 3d ²	\uparrow \uparrow \square \square \square	2.83
Cr ³⁺	[Ar] 3d ³	\uparrow \uparrow \uparrow \square \square	3.87
Cr ²⁺ /Mn ³⁺	[Ar] 3d ⁴	\uparrow \uparrow \uparrow \uparrow \square	4.90
Mn ²⁺ /Fe ³⁺	[Ar] 3d ⁵	\uparrow \uparrow \uparrow \uparrow \uparrow	5.92
Fe ²⁺ /Co ³⁺	[Ar] 3d ⁶	$\uparrow\downarrow$ \uparrow \uparrow \uparrow \uparrow	4.90
Co ²⁺	[Ar] 3d ⁷	$\uparrow\downarrow$ $\uparrow\downarrow$ \uparrow \uparrow \uparrow	3.87
Ni ²⁺	[Ar] 3d ⁸	$\uparrow\downarrow$ $\uparrow\downarrow$ $\uparrow\downarrow$ \uparrow \uparrow	2.83

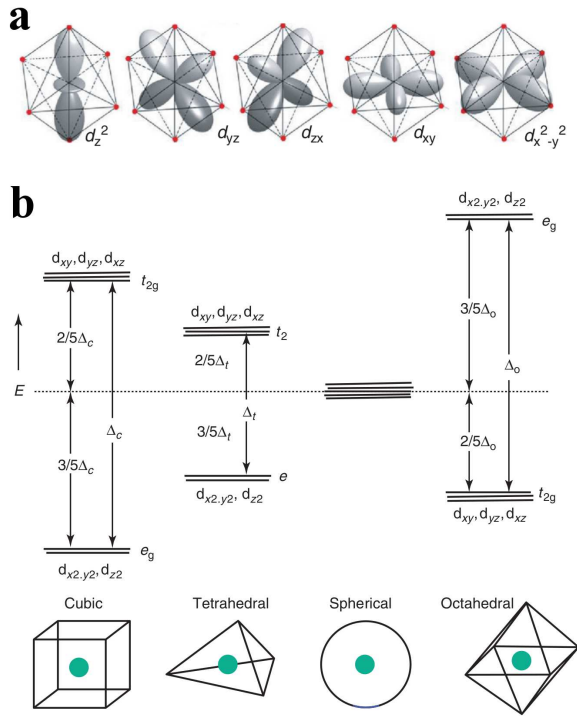


Fig. 6.1.: 3d orbitals in a cubic crystal field (a) which are subject to crystal field splitting depending on their ligand-field (b). Occupation and degeneracy of bonding orbitals in the respective cases determines magnetic exchange interaction between 3d TM ions. [3]

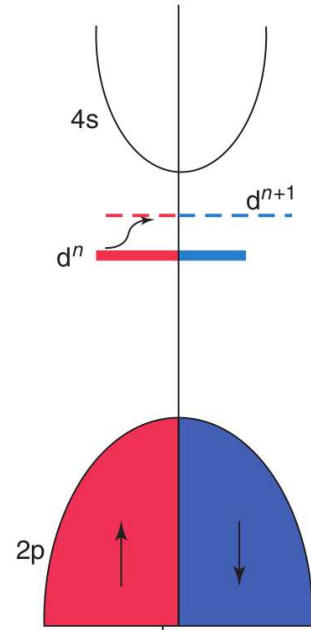


Fig. 6.2.: Typical band gap of several eV between electrons of occupied 2p oxygen orbitals and empty ion 4s conduction orbitals of 3d TM in insulating oxides. Hybridised $3d^{n+1}$ electrons of the 3d TM ions are typically located in the gap. [3]

interactions of spins mediated by intermittent oxygen orbitals [3, 107, 108]. 3d TM elements form part covalent part ionic chemical bonds by overlap of their 3d with the 2p oxygen orbitals. As recalled in Fig. 6.1, depending on the local crystal-field, 3d electrons might be distributed in triply degenerate t_{2g} (d_{yz}, d_{zx}, d_{xy}) or e_g ($d_{x^2-y^2}, d_{z^2}$) orbitals. The degeneracy and occupation plays a crucial role in the type of interaction as explained in the next section. As a result from the orbital overlap, the $3d^{n+1}$ band usually falls in the gap spanned up by $2p^6$ oxygen valence band and the unoccupied 4s conduction band of the transition metal cations (Fig. 6.2). The gap typically accounts to several eV giving rise to the insulating character of most oxide structures.

6.2. Magnetic exchange interactions in oxides

The magnetic order in solids is governed by symmetry constrained coulomb forces causing exchange interactions among magnetic moments of neighbouring ions [109]. The interionic exchange J_{ij} couples spins of adjacent ions and is dependent on the

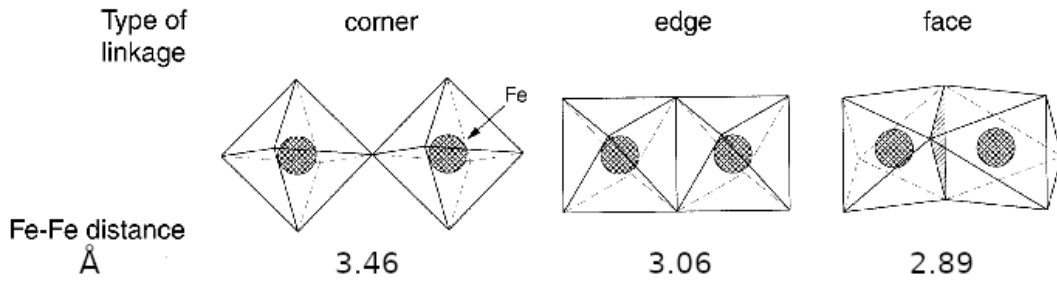


Fig. 6.3.: Octahedrally coordinated 3d TM in oxide structures providing corner-, edge- and face-sharing topologies entailing different magnetic interactions. Typical intercationic distances are provided for Fe³⁺. [114]

overlap of exponentially decaying wave functions of orbital electrons in adjacent ions. Though J_{ij} is usually very weak (0.01 - 0.02 eV) [3] it realises the interaction among strong intraionic exchange, i.e. spin coupling within the 3d subshell, resulting in long range order magnetic moments. The interionic exchange between spins \mathbf{S}_i and \mathbf{S}_j of a pair of ions is expressed in terms of the Heisenberg Hamiltonian H_{ex} :

$$H_{ex} = -2J_{ij}\mathbf{S}_i \cdot \mathbf{S}_j \quad (6.1)$$

Spins are coupled by the Heisenberg exchange J either parallel ($J > 0$) or antiparallel ($J < 0$), giving rise to ferromagnetic or antiferromagnetic/ferrimagnetic ordering, respectively.

Because magnetic exchange interactions in oxides are realised predominantly via bridging oxygen electrons, the orbital structures of involved ions are crucial. They determine sign and strength of the interaction by the degeneracy of 3d orbitals of metal ions and the overlap with 2p orbitals of oxygen. The specific discussion of the Hamiltonian and exchange integral J involves elaborate calculations and *ab initio* simulations, as well as inelastic magnetic scattering techniques. However, experimentally evaluated magnetic spin structures, e.g. from neutron diffraction data, are commonly validated on the basis of exchange interaction rules systematically studied by Kanamori [110], Goodenough [111], and Anderson [112], commonly referred to as *Goodenough-Kanamori rules (G-K rules)* [113]. These guidelines enable to estimate magnetic interactions based on 3d orbital occupation and geometrical considerations for a given topology, i.e. M-M distances, and M-O-M angles. 3d TM elements in phosphatic oxyhydroxides are usually in octahedral coordination which link corner-, edge-, or face-wise (Fig. 6.3). Magnetic interactions within complicated octahedral topologies can be competing causing complex spin orders.

6.2.1. Superexchange interaction (SE)

While there is little or no overlap of 3d orbitals of neighbouring magnetic ions to cause electrical conductivity, both of them strongly overlaps with bridging 2p oxygen orbitals. The hybridisation of 3d and 2p orbitals acts as a transmitter of 3d electron

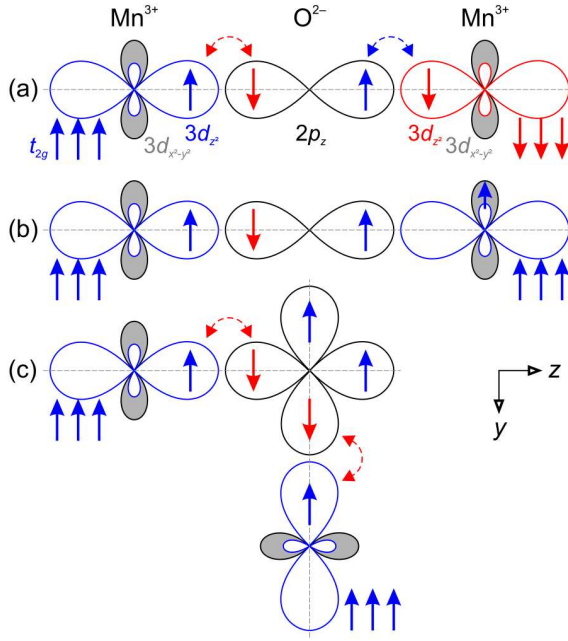


Fig. 6.4.: Superexchange interactions according to *G-K* rules [113] between two Mn^{3+} $3d_{z^2}$ orbitals via $2p_z$ oxygen orbitals realised for example in LaMnO_3 . Depending on the occupation of d_{z^2} and $d_{x^2-y^2}$ (grey) orbitals, the interaction can be strongly AFM (**a**), or weakly FM (**b**) & (**c**). (**a**) and (**b**) involve corner sharing topology (180° case) and (**c**) edge- or face-sharing topology (90° case). [108]

spin states by virtual electron transfer over $2p$ oxygen orbitals. Intraionic spins of adjacent $3d$ TM ions are correlated such that the virtual electron hopping does not violate *Pauli's exclusion principle*, i.e. two electrons of same spin state in one orbital. Such indirect magnetic spin interaction via oxygen orbitals are termed *superexchange* (SE) interactions constituting by far the most common and important magnetic coupling mechanism in oxides.

Depending on the geometry, degeneracy and occupation of the participating orbitals, AFM or FM magnetic interactions can be assessed using *G-K* rules. An example is provided in Fig. 6.4 for Mn^{3+} - Mn^{3+} interactions in cubic LaMnO_3 [108]: Mn^{3+} ions are octahedrally coordinated by six oxygen. Oxygen has the electronic configuration $1s^2 2s^2 2p^6$ where the bonding orbitals p_x , p_y , and p_z are fully occupied by electrons. Mn^{3+} has the electronic configuration $[\text{Ar}]3d^4$, with three electrons in degenerate low energy t_{2g} orbitals and one occupying either $d_{x^2-y^2}$ or d_{z^2} orbital, which make bonding out of overlapping $2p$ oxygen orbitals.

SE interactions causing AFM or FM spin order are initiated respecting *Pauli's exclusion principle* and *Hund's rule*: i) electrons in the same e_g orbital need to exhibit antiparallel spins, and ii) electrons of parallel spins should be situated in different orbitals, i.e. e_g and t_{2g} .

The bonding and orbital configuration leaves the following coupling scenarios illustrated accordingly in Fig. 6.4a-c:

- With both Mn^{3+} having singly occupied d_{z^2} orbitals pointing towards each other, the virtual electron transfer from p_z oxygen orbital causes a strong 180° AFM coupling.
- If d_{z^2} orbital is occupied in one Mn^{3+} pointing towards the empty one of the other, this will favour weak 180° FM coupling ($J > 0$).

- (c) If the Mn-O-Mn bonding involves two perpendicular $2p$ orbitals (p_z, p_y), the virtual electron transfer establishes weak 90° FM coupling.

The above SE coupling possibilities point out that the specific case of 3d TM combinations requires special treatment due to the crucial role of occupation, symmetry, and degeneracy of 3d orbitals. In addition, interaction strength (J) depends critically on the atomic separation and correlates strongly with the M-O-M opening angle by $\cos^2\theta$. Many possible combinations considering geometrical arrangements of 3d TM are summarised in the *G-K* rules [113], which may be applied in a simplified manner:

- If two cations have singly occupied orbital lobes pointing towards each other, then the exchange is strong and AFM ($J < 0$). This case is valid for M-O-M angles of 120° - 180° (see case (a) above), which occurs for corner-linked $[\text{MO}_6]$ octahedra.
- If two cations have 3d orbital lobes pointing towards each other, where one is singly occupied and the other empty or fully occupied, then the exchange is weak and ferromagnetic ($J > 0$). This case is also valid for M-O-M angles of 120° - 180° realised by corner-linked $[\text{MO}_6]$ octahedra (see case (b) above).
- If orbital overlap of two singly occupied 3d orbitals is excluded by symmetry, i.e. if they are rotated by 90° with respect to each other, then the exchange is relatively weak and FM. This is valid for M-O-M angles of $\approx 90^\circ$ (see case (c) above), and is comprised in edge- and face-sharing $[\text{MO}_6]$ octahedral configurations.

6.2.2. Double exchange

In contrast to SE interaction, *double exchange* mechanism (DE) includes real electron transfer among mixed valence 3d TM ion pairs, e.g. $\text{Fe}^{2+}/\text{Fe}^{3+}$ and $\text{Mn}^{3+}/\text{Mn}^{4+}$, causing FM interaction [2, 115]. The case for DE between Mn^{3+} and Mn^{4+} in $\text{La}_{0.5}\text{Ba}_{0.5}\text{MnO}_3$ is illustrated in Fig. 6.5. Itinerant d_{z^2} electrons can be transferred from Mn^{3+} via the p_z orbital to the empty Mn^{4+} d_{z^2} orbital resulting in two virtually degenerate states. With respect to *Hund's rule*, this mechanism is especially favourable once the intraionic spin of both Mn ions is parallel, i.e. when they are FM coupled, since the transferred electron must not change its spin. Correlation of electric conductivity and FM order realises local or long range magnetoresistive phenomena.

Similar to SE, the DE mechanism must be treated case by case by investigating geometry, degeneracy and coordination of the 3d orbitals.

6.2.3. Direct exchange

Less common in oxides is the *direct exchange* from direct overlap of two 3d orbitals of different cations. It requires a close intercationic distance in face-sharing octahedral topology involving electron hopping between partially filled t_{2g} orbitals (Fig. 6.6)

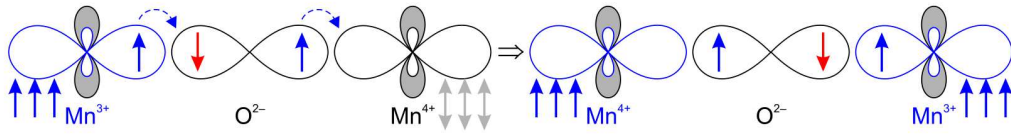


Fig. 6.5.: Double exchange mechanism among mixed valence $3d$ TM ions via an interstitial p_z oxygen orbital. FM coupling is energetically favourable because no spin change of the transferred electron between two cations of similar intraionic spin is required. [108]

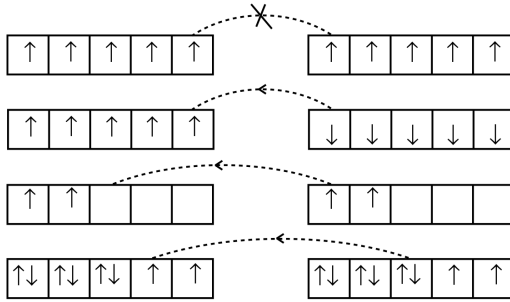


Fig. 6.6.: Direct exchange of delocalised electrons in adjacent $3d$ orbitals causing AFM or FM order depending on the occupancy of the neighbouring $3d$ orbital. [109]

[113]. Similar to DE, this involves delocalised $3d$ electrons and must be treated case by case regarding the $3d$ orbital occupations.

6.3. Magnetic order in oxides

In crystals with periodically arranged magnetic ions, the various exchange interactions result in a spontaneous long range order of atomic dipoles, i.e. magnetic spins, below a critical transition temperature (Fig. 6.7). In contrast to AFM structures, FM and ferrimagnetic structures result in a macroscopic magnetisation below T_c (Fig. 6.8). The oppositely arranged sublattices in AFM structures with magnetic moments $\mathbf{M}_A = \mathbf{M}_B$ cancel out, causing zero magnetisation below Néel temperature T_N . In ferrimagnetic structures, the spin lattices are not equal, nor do they require to be in antiparallel orientation, i.e. ($\mathbf{M}_A \neq \mathbf{M}_B \neq \mathbf{M}_C \dots$). The magnetisation curves measured versus temperature contain contributions of the various sublattices which may give rise to unusual net magnetisation curves.

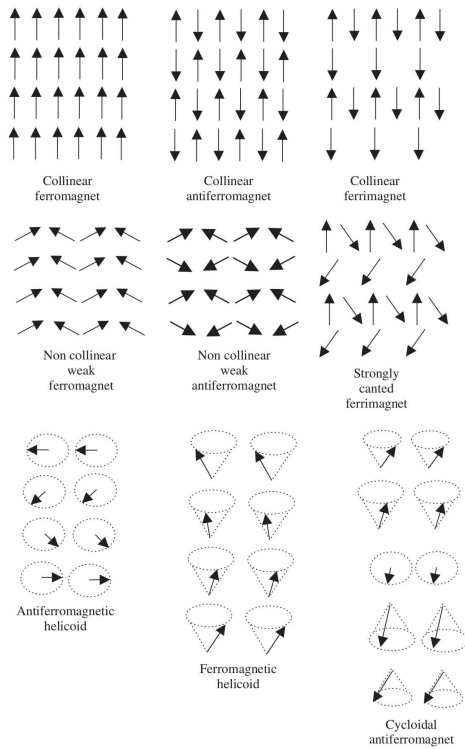


Fig. 6.7.: Several FM, AFM and ferrimagnetic spin structures. [116]

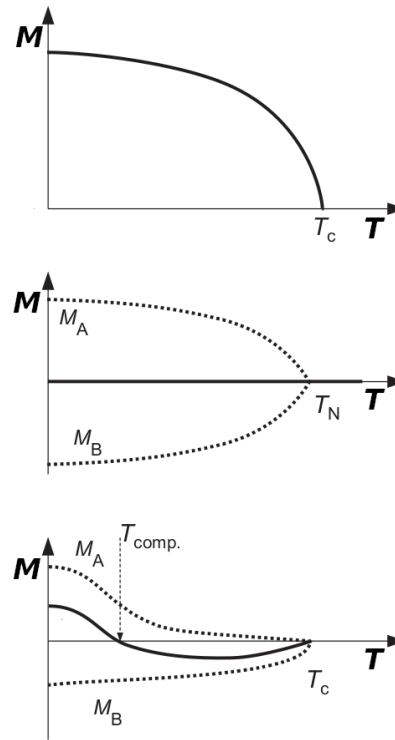


Fig. 6.8.: Top to bottom: typical curves of spontaneous magnetisation (M) upon cooling obtained for FM, AFM and ferrimagnetic structures with sublattices A and B. [117]

6.3.1. Symmetry of magnetic spin orders

Strength and orientation of ordered magnetic spin (sub-)lattices are resolved using neutron diffraction techniques complemented by group theoretical analysis. The neutron has a spin giving rise to a magnetic dipole, which may interact with spins of the matter under investigation. Neutron diffraction methods are of particular importance for ferrimagnetic and AFM structures where details of the spin sublattices are commonly hidden from a macroscopic viewpoint and are indispensable to resolve complex cycloidal or helical spin orders shown in Fig. 6.7.

A periodic magnetic spin structure is described in terms of magnetic space groups (MSGs) (*Shubkinov* groups). Besides the nuclear symmetry, MSGs may contain additional symmetry operators which rotate magnetic spins while the atomistic lattice stays untouched, the so called *time-reversal* (Fig. 6.9). Time-reversal operation is understood as inverting the rotation of a current flow responsible for a magnetic dipole. Symmetry operations with subsequent time-reversal are *primed*, e.g. $2'$, m' , c' . They add an extra dimension to the 3D space symmetry enabling to simultaneously relate polar vectors, i.e. atomic positions, and axial vectors (magnetic moments) in the unit cell by symmetry operation.

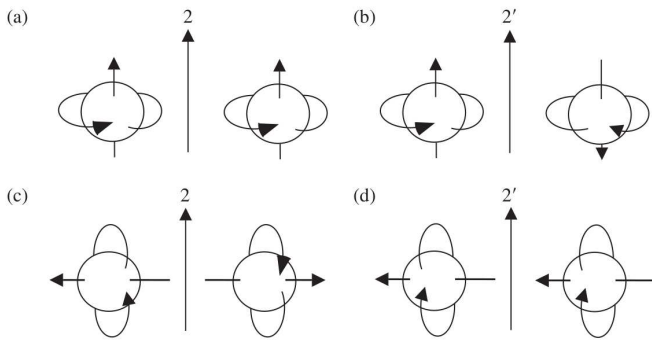


Fig. 6.9.: Proper twofold rotation symmetry (2) is contained for particle and magnetic spin in (a) and (c). Time reversal is applied to magnetic spin current in (b) and (d) after proper twofold rotation of particles and their spin currents, resulting in the operation $2'$. [116]

The 1651 MSGs applicable for AFM, FM and ferrimagnetic orders include the 230 classical crystallographic space groups of which they are derived as subgroups adding time-reversal [118]. Hence, given a known space group of a crystal structure there are usually multiple MSGs to choose from. The group - subgroup relation can be performed via group theoretical representation analysis, which is implemented in software packages such as Jana2006 [119]. The subsequent selection of possible MSGs can be facilitated using (direction dependent) magnetic susceptibility or magnetisation measurements. This is especially effective, since AFM and ferri-/ferromagnetic spin orders are explained in mutually exclusive MSG symmetries. If single crystals are provided, an anisotropy of spin order can be determined by magnetic characterisation methods, i.e. easy- and hard-axis of spin alignments, further downsizing the list of possible MSG.

In practice neutron diffraction patterns are treated via least-square refinements using a list of considered MSG and the reliability factors of the single approaches are compared.

Part III.
Instrumental methods

7. Analytical characterisation methods

7.1. Chemical analysis with Electron Probe micro analysis (EPMA)

Determination of chemical composition is the essential prerequisite for several further instrumental methods. Particularly structure analyses using diffraction techniques, but also magnetometric and thermal characterisations, as well as spectroscopic methods rely on exactly specified sample chemistry.

EPMA delivers concentration ratios of elements with $Z > 4$ in solid state matter with accuracy of 0.01 wt% based on reference materials with known chemical composition. A particular advantage of this method is the possibility to obtain spatially-specific chemical compositions. Chemical gradients can be observed by line scans where elemental compositions are acquired along a line with predefined step widths. Good statistics are easily obtained in homogeneous samples by collecting compositions at multiple points on one sample.

Sample fragments are moulded in epoxy-resin and carefully polished prior to be carbon-coated, allowing electrical conductivity. An electron beam is produced by a cathode with 10 nA current and an accelerating voltage of 40 kV. Sets of magnetic lenses focus the beam on the sample surface where a spot of $\approx 2 \mu\text{m}$ in diameter excites a small volume in the probed material. Atoms in the sample subsequently emit characteristic X-ray radiation, which can be analysed by means of energy dispersive (EDX) or more accurate wavelength-dispersive (WDX) X-ray spectroscopy. EDX is usually performed to quickly obtain a list of elements of which the concentrations are determined precisely via WDX method. Using the latter, element characteristic X-rays are coherently scattered at crystal lattice planes of known d-spacing and orientation in the detector module following Bragg's law ($\lambda = 2d \sin\theta$). The detected intensity gives information about the concentration of emitting atoms in the sample.

7.2. Thermal behaviour

7.2.1. Heat capacity at $T \leq 298 \text{ K}$

Heat capacity is a measurement quantity highly sensible to sample inherent temperature dynamics as a function of the ambient temperature. Heat dissipation and assimilation caused by first order phase transitions, recrystallisation processes, or sample amorphisation give rise to discontinuities resolved as exothermic and endothermic anomalies.

Heat capacity between 2 K and 298 K was measured using a Physical Properties Measurement System (PPMS) from *Quantum Design*. The heat capacities of the measuring apparatus and the sapphire sample stage are determined first to be subtracted

from the sample heat capacity. Samples of exactly determined weight are attached to the sample stage with grease of good heat transport properties. Using *short pulse method*, samples are heated in short time periods and temperature intervals and heat capacity is derived from the time required for cooling to the initial ambient temperature.

7.2.2. Thermogravimetry (TGA) and differential scanning calorimetry (DSC) at $T \geq RT$

Combined TGA and DSC analyses above 300 K provide respective information about weight loss and heat capacity of the sample. Quantifying the total weight loss determines the content of volatile structure constituents, such as OH or OHO groups being extracted upon heating the samples. The temperature dependent weight loss in combination with the heat capacity curve from DSC gives insights into decomposition steps of the material under investigation.

Two tiny platinum vessels identical in size and weight are placed close together in the heating chamber of a thermo-microbalance such that thermal ambience is assumed uniform for both. A sample of exactly determined weight (≈ 10 mg) is placed in one vessel and the chamber is heated by certain rate under a constant flow of inert gas. TGA provides the loss of sample weight as function of the temperature. Via DSC the heat capacity of the sample is evaluated through its thermal dissipation or admission in comparison to the empty reference Pt vessel.

7.3. Magnetometric characterisation

Magnetic behaviour of materials is characterised through magnetic susceptibility (χ) and magnetisation (M) curves as a function of temperature. As magnetic spins order in the course of a phase transition, these quantities are direction dependent properties. Using crystals of known orientation, χ and M provide a variety of information on the kind and behaviour of magnetic spin alignments in the specimen, which is highly desirable for solving their structure using neutron diffraction methods.

The magnetic susceptibility $\chi = \frac{\delta M}{\delta H}$ is a very sensible measure of the sample's ability to be magnetised by an external magnetic field H . At magnetic transition temperatures, $\chi(T)$ measurements exhibit anomalies which serve as temperature markers, e.g. Curie Temperature (T_c), or Néel Temperature (T_N).

Transitions from paramagnetic to ferromagnetic, ferrimagnetic, or antiferromagnetic states are identified by the course of $\chi(T)$ curves covering paramagnetic and magnetically ordered temperature regions. Plotted inversely, i.e. ($\chi^{-1}(T)$), the paramagnetic Curie Temperature (θ_p) can be assessed by extrapolating the paramagnetic region of the curve towards the temperature-axis (Fig. 7.1). Following the *Curie-Weiss-law* in the PM region, $\theta_p < 0$ K indicate AFM and ferrimagnetic spin alignments, whereas $\theta_p > 0$ K is typical for ferromagnetism [117]:

$$\text{ferromagn.} : \chi = \frac{C}{T - \theta_p}$$

$$\text{ferri- / antiferromagn.} : \chi = \frac{C}{T + \theta_p}$$

Zero field cooled $M(T)$ and $\chi(T)$ data between 2 K and 350 K were recorded using two different devices:

1. PPMS

A sample stage is situated within the centre of a coil which produces an alternating magnetic field of 1 kHz and 10 mT. Altered by the magnetic properties of the sample, the field induces an alternating current within a second coil, from which χ_{AC} can be computed.

2. MPMS (Magnetic Properties Measurement System, *Quantum Design*)

The sample is oscillated at 1 Hz nearby a detection coil in which a current is induced depending on the magnetic state and the strength of sample magnetisation. Time-dependent voltage is measured of which DC magnetic moment $M(T)$ can be inferred.

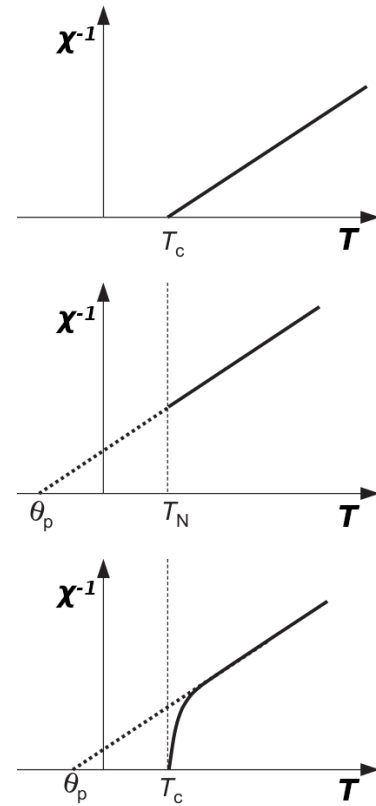


Fig. 7.1.: Schematic $\chi^{-1}(T)$ curves for FM, AFM, and ferrimagnetic transitions (top to bottom). Figure revised from [117].

7.4. Spectroscopy

7.4.1. Fourier Transformed Infrared (FTIR) Spectroscopy

The principle of (FTIR) spectroscopy is the absorption of infrared electromagnetic radiation by molecular vibrations. Substances can be identified by their fingerprint spectra. In oxides and oxyhydroxides, spectra include cation-oxygen bond vibrations, e.g. in Fe–O and P–O coordinations, but are particularly valuable resolving bands typical for O–H and H–O–H groups replacing oxygen ligands.

About 1 mg of sample is pressed into pellets with non-absorbing KBr and screened repeatedly in transmission mode in CO₂ inert atmosphere.



Fig. 7.2.: Clamp-cell to apply isostatic pressure while recording dielectric response: outer screws are tightened during pressure adjustment through a piston (left) pushing the stencil (mid-left) on the white Teflon sample capsule (mid-right) inserted into the pressure chamber (centre). Teflon vessels are filled up with pressure transmitting daphne oil.

7.4.2. Dielectric spectroscopy

Capacitance $C(T)$ and loss tangent

Frequency dependent dielectric response is sensitive to the development of polar states or conductivity phenomena in sample materials. For example, spontaneous (anti-)ferroelectric phase transitions in crystals are observable as anomalies at transition temperatures. Also the frequency and temperature dependent local and long range dynamics of polarisable species can be investigated, such as proton conduction or their dynamics in HBs.

The dielectric response is measured by applying alternating electric fields (kHz - MHz) to electrodes attached oppositely to polished surfaces of thin samples (≈ 0.1 mm). The real part of the dielectric permittivity ϵ' is calculated from the measured capacitance C and evaluated as a function of the sample thickness (d) and the areas (A) of the electrodes. The *loss tangent* is proportional to the imaginary part ($i\epsilon''$) of the complex dielectric constant:

$$\epsilon = \epsilon' + i\epsilon'' \quad (7.1)$$

$$\epsilon' = \frac{d \times C}{A \times \epsilon_0} \quad (7.2)$$

In the kHz range, ϵ' represents stored (capacitive) energy in the form of reorientation processes of polarisable species or charges following the alternation of the applied electric field (E_{AC}). The loss factor, being proportional to ϵ'' is a measure of lost energy through ionic charge transfer, i.e. electrical conductivity. [97]

To scan for lattice distortion related effects, these dielectric response can be recorded while isostatic pressure ($p \leq 1.6$ GPa) is applied using a clamp cell (Fig. 7.2).

Impedance spectroscopy (IS)

Charge transport capability of ion-conductors is characterised by applying alternating electric fields (E_{AC}) to electrodes attached to the sample surface and scanning the

complex electrical resistance, i.e. the impedance Z [Ω],

$$Z = Z' + iZ'' \quad (7.3)$$

The real part impedance, Z' represents the resistance occurring due to charge transport, whereas Z'' represents the capacitive properties of the sample [120]. The frequency dependence of Z' and Z'' are meaningfully illustrated in complex-plane plots (*Nyquist plots*), where Z' and Z'' are equally scaled as ordinate and as abscissa, respectively. Typically for ionic conductors, the frequency dependent (Hz - MHz) measuring points describe at least one semicircle in the complex plain. Charge transfer at the sample electrode interface is indicated by an increase of Z'' in the low-frequency range of the spectra [121]. The intersection of the semicircle with Z' axis gives a fair estimate on the bulk electrical sample resistance (R), which is transformed to the bulk sample conductivity σ_{bulk} knowing the specimen thickness (l) and area (A) of the attached electrodes:

$$\sigma_{bulk} = \frac{1}{\rho} = \frac{l}{RA} \quad (7.4)$$

7.4.3. ^{57}Fe Mössbauer spectroscopy

The present study deals with oxyhydroxide structures containing more than one crystallographic site available for mixed valence occupation by Fe^{2+} and Fe^{3+} . The proper analysis of their nuclear and magnetic structures requires to determine the contents and siting of Fe with different oxidation states. However, mixed valence site occupations are not accurately accessible by structure analysis using diffraction methods, nor by chemical analysis. The particularly sensitive Mössbauer spectroscopy allows to distinguish electronic configurations of Fe cations as a function of the local ligand environment and oxidation state. This even enables to assign Fe of equal oxidation states to unique crystallographic structure sites [122].

The method represents a combination of recoil-less core resonance absorption of γ -rays and the Doppler-effect. Unstable $^{57}_{26}\text{Fe}$ nuclei in the source material decay under the emission of high-energy electromagnetic waves of ≈ 14.4 keV. In the sample material, these γ -rays are resonantly absorbed exclusively by exciting Fe cores with identical electronic configuration. The sample absorbance is quantified straightforwardly by a counting detector situated behind the sample. A range of electronic configurations of different energy states is scanned by tiny modulations of the γ -ray wavelength. This is introduced by the Doppler-effect of emitter source and sample moving towards and apart from each other with certain velocities in the mm/s range. Hence, velocity dependent absorption spectra are obtained. Crystal-chemical information on Fe and its environment can be extracted from spectral parameters arising from interactions between the Fe core and its electron-shell [122]:

1. Isomer shift (IS) [mm/s]

The energy difference, i.e. IS, between core ground state in the source material and excited state in absorbing sample material is represented by an absorption

maximum at $v \neq 0$ mm/s. Due to the electronic environment of the core, IS is indicative for Fe oxidation states, the type of ligand bonding, as well as their electron negativity.

2. Quadrupol splitting (QS) [mm/s]

Fe cores have a non-spherical charge distribution, i.e. quadrupol, which interacts with a local inhomogeneous electric field. The latter is present because electrons are asymmetrically arranged around the Fe core, and influenced by the type of ligands and bonding geometry. Excited Fe cores in non-cubic symmetries exhibit a quadrupol splitting with two possible quadrupol orientations of disparate energies relative to the electric field. As a result, absorption doublets are observed rather than single IS for each Fe core in a unique electronic environment. The energy difference ΔE_Q between two quadrupol orientations is reflected by a velocity difference QS [mm/s] within the absorption doublet. From QS values, geometry and symmetry of the ligand environment can be inferred, as well as the oxidation state of Fe.

3. Area fractions [%]

Knowing the total content of Fe in the sample from chemical analysis, the area fractions of the doublets are proportional to the respective unique Fe configurations. Hence, abundance of Fe^{2+} and Fe^{3+} oxidation states and their relative crystallographic sites distribution can be quantised.

7.5. Structure analysis using X-ray and neutron diffraction techniques

The scaffold for optical, dielectric, or magnetic properties is the type and symmetric order of atoms arranged in the crystal lattice. Understanding the crystal structure is the vital basis to explain underlying mechanisms of condensed matter physical properties. Only marginal reconfigurations in the crystal structure, i.e. shift or disorder of atoms, may change the crystal symmetry and can involve phase transitions accompanied by dramatic changes of physical behaviour. Crystal structures are commonly analysed using X-ray/neutron diffraction techniques, revealing the atomic arrangement and its local or long range dynamics. The basic principle of diffraction techniques is the reflection of coherent electromagnetic waves or neutrons of a fixed wavelength ($\lambda \approx 0.2 - 20 \text{ \AA}$) by periodically arranged atoms in the crystal lattice. The atomic order describes sets of parallel lattice planes running quasi-infinitely through the crystal structure. An angle (2θ) between incident and reflected beam under which elastically scattered reflections are observed depends on the spacing d_{hkl} between parallel lattice planes:

$$\frac{\lambda}{2d_{hkl}} = \sin \theta \quad (\text{Bragg's law}) \quad (7.5)$$

Only those reflected photons (neutrons) fulfilling Bragg's law interfere constructively and are observed by a detector placed at an angle 2θ from the incident beam (Fig.

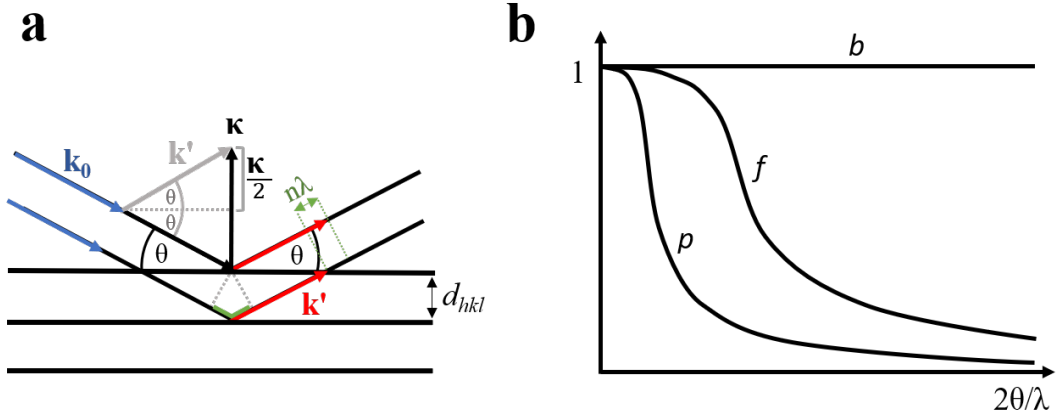


Fig. 7.3.: (a) Schematic drawing of elastic scattering where the modulus of the wavevectors $|\mathbf{k}| = \frac{2\pi}{\lambda}$ is constant for incoming (blue) and reflected (red) rays. Reflections occur under an angle 2θ when the d_{hkl} dependent change of path lengths (green) of parallel incoming rays equals an integer multiple of their wavelength λ . (b) Comparison of normalised nuclear (b) and magnetic (p) neutron scattering lengths with atomic scattering factor (f) used for X-ray diffraction as a function of $2\theta/\lambda$.

7.3a). Thereby the scattering vector ($\kappa = \mathbf{k}' - \mathbf{k}_0$) is constructed through the wavevectors of incoming and outgoing rays ($|\mathbf{k}_0| = |\mathbf{k}'| = \frac{2\pi}{\lambda}$), and is perpendicular to the reflecting lattice planes in elastic scattering. Being equal to the reciprocal lattice spacing $|\kappa| = \frac{2\pi}{d_{hkl}}$ the relation to Eq. 7.5 is established by:

$$\kappa = 2k \sin\theta = \frac{4\pi}{\lambda} \sin\theta = \frac{2\pi}{d_{hkl}} \quad (7.6)$$

From the 2θ positions and the combination of observed reflections, lattice parameters and symmetry of the structure can be obtained. The intensity is a function of atoms in the unit cell constituting the reflecting lattice planes. It is proportional to the square of the structure factor F_{hkl}

$$F_{hkl} = \sum_{i=1} f_i e^{i\kappa \cdot \mathbf{r}_i} = \sum_{i=1} f_i e^{-2\pi i(hx_i + ky_i + lz_i)} \quad (7.7)$$

with the sum over the i th atom at position $\mathbf{r}_i = x_i \mathbf{a} + y_i \mathbf{b} + z_i \mathbf{c}$ in the unit cell ($\mathbf{a}, \mathbf{b}, \mathbf{c}$: basic vectors). f_i are the element specific atomic scattering factors depending on $2\theta/\lambda$ using X-ray diffraction. The electron density distribution $\rho(\mathbf{r})$ in the unit cell is obtained from the inverse Fourier Transform of the structure factor:

$$\rho(\mathbf{r}) = \frac{1}{V} \sum_{h,k,l=-\infty}^{+\infty} F_{hkl} e^{-2\pi i(hx + ky + lz)} \quad (7.8)$$

Maxima in $\rho(\mathbf{r})$ evaluated from relation Eq. 7.8 lack the phase information, i.e. the contribution of varying scatterers to $\rho(\mathbf{r})$. To solve the *phase problem* of the Fourier Transform, a variety of methods, i.e. *Direct methods*, *Patterson method*, or

Charge flipping [123, 124], are applied allowing to solve 3D crystal structures. Subsequently, structure parameters are refined using a least square algorithm minimising weighted (w_h) discrepancies between observed structure factors and those of the calculated model [125]:

$$S = \sum_{hkl} w_{hkl} (|F_{hkl}|_o - |F_{hkl}|_c)^2 \quad (7.9)$$

To identify missing atoms in the structure model, difference Fourier (ΔF) synthesis is a powerful method to find residuals in the electron density distribution,

$$\Delta\rho(\mathbf{r}) = \rho_o(\mathbf{r}) - \rho_c(\mathbf{r}) = \frac{1}{V} \sum_{h,k,l=-\infty}^{+\infty} (|F_o| - |F_c|) e^{i\alpha_c} e^{-2\pi i(hx+ky+lz)} \quad (7.10)$$

where F_c and F_o are structure factors of calculated model and observed intensities, respectively. $\Delta\rho(\mathbf{r})$ calculations are particularly effective to find missing atoms near to heavy species, as well as to errors in the siting and temperature factor of refined structure models [125]. ΔF synthesis are conveniently represented in ΔF maps. These allow to graphically include new atoms with proper bonding distance in the existing structure model framework, but are also useful to resolve diffusion pathways of mobile ions.

Other than X-rays, neutrons interact with the core of atoms, as well as with the magnetic spin of unpaired electrons as neutrons carry a magnetic moment themselves. This allows for the detection of light elements invisible to X-rays, e.g. Li and H, and makes neutron scattering the most important tool to solve magnetic spin structures. As the analogue to the atomic scattering power f_i using X-rays, the neutron scattering capability of nuclei is given by the coherent scattering length b_i [fm]. Whereas f_i increases with the number of electrons Z of an atom, the isotope specific b_i varies erratically across the periodic table and has negative values for H, Li, Mn, Ti, V, ^{52}Ni , and Sm. Therefore, element ratios at shared lattice sites can be determined for crystal chemically similar species with little difference in Z , which are indistinguishable for X-rays, e.g. Mn and Fe with $b(\text{Mn}) < 0 < b(\text{Fe})$.

Similarly, the neutron scattering by unpaired electron spins is defined by a magnetic scattering length p_i [fm]. Magnetic spin order can be inferred from magnetic Bragg reflections representing their symmetrical arrangement with respect to the nuclear unit cell. Along with a magnetic interaction vector μ_i giving the direction of a magnetic spin relative to the scattering vector κ , the nuclear and magnetic contributions to $|F_{hkl}|^2$ add up to:

$$|F_{hkl}|^2 = \left| \sum_{i=1} b_i e^{(-i\kappa \cdot r_i)} \right|^2 + \left| \sum_{i=1} p_i \mu_i e^{(-i\kappa \cdot r_i)} \right|^2 \quad (7.11)$$

The relatively weak scattering of neutrons in solids, as well as the little flux compared to conventional laboratory X-ray sources requires samples of comparably large volume about $> 1\text{cm}^3$. Another distinct advantage of neutrons in diffraction experiments is the independence of b_i from the scattering angle 2θ (Fig. 7.3b). This allows for the proper evaluation of atomic displacement parameters best expressed in intensity variations at high 2θ angles [125], which is important to evaluate at-site dynamics of ions.

7.5.1. X-ray single crystal diffraction (XSD)

Single crystal X-ray diffraction (XSD) is the most common method for structure analysis. The reciprocal lattice of the crystal structure is obtained by step-wise rotating the crystal ($\approx 100 \times 100 \times 100 \mu\text{m}^3$) positioned in a fixed X-ray beam using a κ -four-circle geometry (Fig. 7.4). Supported by modern software packages, crystals are rotated such that reflections are detected by a CCD area detector scanning 2θ angles in plane with the beam source. Symmetry equivalent reflections are redundantly scanned to increase statistics and enhance integrity of data sets. Structure information is obtained from the reciprocal lattice metrics and the integrated intensities of its nodes represented by the observed reflections. Highly reliable structure models are achieved by least-square (LS) refinements of atomic parameters i.e. position, site occupation, displacement, giving accurate inter-atomic bonding-lengths and good approximations of atomic at-site motions.

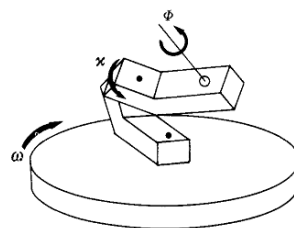


Fig. 7.4.: Geometry of a κ -four-circle goniostat. Crystals are attached to a goniometer rotating about Φ (fourth angle: 2θ) [126]

7.5.2. Powder diffraction methods

X-ray powder diffraction (XPD) and high resolution neutron powder diffraction (HRNPD) are used if no crystals large enough for single crystal diffraction are available, or to perform qualitative and quantitative phase analysis of mixed powders. Powders are packed in capillaries for transmission mode (*Debye-Scherrer*) or, for XPD only, in flat surface sample holders for reflection geometry (*Bragg-Brentano*). Intensities are recorded by static or mobile detectors in the 2θ plane of the incoming beam. For any 2θ angle scanned, various crystallites in the probed volume are oriented such that Eq. 7.5 is satisfied. Observable intensity is enhanced by rotating the sample holders by a constant rate while scanning. The emerging diffraction cones give rise to 2D diffraction patterns which are regarded as fingerprints for the substance under investigation. Structural information is obtained by analysing 2θ position of diffraction peaks and their intensity distribution. Similar to XSD, structure solution can be performed analysing peak positions and intensities. A disadvantage compared to XSD arises from the folding of the 3D reciprocal diffraction pattern into one 2θ dimension [125]. This may lead to peak overlap and ambiguity in the assignment of peak intensities.

Provided a reasonable starting structure model exists, the *Rietveld-method* is a powerful least-squares refinement algorithm to perform structure analysis with powder diffraction data. Typically, sample offset, background, and peak shape are refined together with starting values for the structure model, i.e. lattice parameters, atomic positions, thermal displacement factors and occupational parameters of atoms. With high resolution datasets, a properly applied Rietveld-analysis can quantify phase fractions with an accuracy below 1 wt% [125]. The applied Rietveld software packages

Fullprof-suite [127] and *Jana2006* [119] also include the refinement of magnetic spin order models.

7.6. Laue method

Anisotropic physical behaviour in crystalline materials is determined by comparing property measurements in distinct crystallographic directions. These assessments require orientedly-cut single crystal samples for the respective analysis.

The Laue-method enables the precise orienting of single crystals. Crystals are placed in a polychromatic X-ray beam at a fixed distance to a photographic plate detecting backscattered reflections of the sample. Using a continuous wavelength spectrum, the Bragg-condition (Eq. 7.5) is fulfilled for multiple lattice plane spacings in the analysed crystal. From the observed reciprocal pattern, the orientation of the crystal's inherent symmetry elements with respect to the photographic plate, and therefore, the relative orientation of the crystal is inferred. Imaging and re-orienting procedures are repeated until the desired crystal orientation is obtained in the pattern. The sample stage can be transferred and adapted to a sawing device for producing crystal cuts normal to the adjusted crystallographic direction.

Part IV.
Case studies

8. Na⁺/Li⁺-ionic conductivity in Fe₂Na₂K[Li₃Si₁₂O₃₀]

8.1. Hydrothermal synthesis

A hydrothermal synthesis route was established to produce the synthetic counter-part of natural sugilite, Fe₂Na₂K[Li₃Si₁₂O₃₀]. Synthesis were performed in an alkali environment to enhance the solubility of α -Fe₂O₃ and SiO₂ in the starting mixtures: NaOH (99%, *Riedel-de Haen AG*), LiOH·H₂O (56.6%, *Alfa Aesar*), KOH (85%, *Merck*), Fe₂O₃ (*Merck*), SiO₂ colloidal dispersion (40 wt% in H₂O, *Alfa Aesar*) were added step by step to deionised water and aged for 4 hours to be heated subsequently in sealed Teflon-lined steel autoclaves at 500 - 540 K for 5 - 14 days.

Rietveld structure analysis using X-ray powder diffraction data of the as-synthesised products confirmed the successful formation of synthetic sugilite analogue Fe₂Na₂K[Li₃Si₁₂O₃₀]. The best yield was obtained from a starting mixture of molar ratios Na:K:Fe:Li:Si:H₂O = 1:1:1:3:7:1000, resulting in 94.6(5) wt% Fe₂Na₂K[Li₃Si₁₂O₃₀] besides a minor impurity of 5.4(1) wt% α -Fe₂O₃.

8.2. Impedance Spectroscopy

Impedance spectra acquired between 963 - 723 K reveal clear high-frequency (HF) relaxation modes expressed by semicircles in complex plane plots of Z'' against Z' . As shown in Fig. 8.1a, the decrease of fitted semicircle diameters with increasing temperature reflects an increase of the bulk conductivity (σ_{bulk}) with rising temperatures. The highest σ_{bulk} value of $1.2 \times 10^{-5} \text{ S cm}^{-1}$ at 963 K is comparable to $4.1 \times 10^{-5} \text{ S cm}^{-1}$ at 923 K [22] acquired with an isostructural sodgianite single crystal

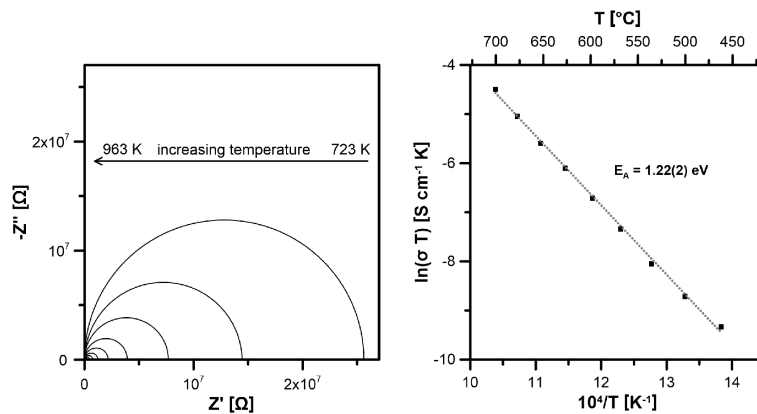


Fig. 8.1.: Fittings of HF semicircles obtained in IS spectra between 963 K and 723 K show the decrease of the bulk resistance with increasing temperature (left); σ_{bulk} values evaluated from the calculated HF semicircles are transferred in an Arrhenius (b). An activation energy E_A of 1.22(2) eV for σ_{bulk} is determined from the slope in a temperature range of 963 - 723 K (right).

measured \perp [001]. Natural polycrystalline sugilite shows a conductivity of 1.7×10^{-3} S cm⁻¹ already at 943 K (Park et al., to be published). The discrepancy compared to the as-synthesised powder is ascribed to strong extrinsic grain boundary conduction effects in the less dense powder pellets of Fe₂Na₂K[Li₃Si₁₂O₃₀].

The inferred temperature dependent conductivity values give rise to linear a progression in the Arrhenius diagram confirming a thermally activated process with an activation energy $E_A = 1.22(2)$ eV (Fig. 8.1b). In sogdianite with proven Li⁺-ionic conductivity \perp [001], a similar value of 1.26(2) eV was observed. These values are much larger than those attributed to electronic or even more energy consuming local motions of Li in aluminosilicates (0.1 - 0.5 eV [121]) and are therefore attributed to long-range ionic conduction.

8.3. Structure analysis

Rietveld refinements of HRNPD data sets acquired at 298 K, 573 K, 723 K, 923 K, and 1123 K show good agreements of observed and calculated intensities and confirm the sugilite-type structure of the main phase [128–132]. The final structure model is supported by proper bonding lengths to oxygen and BVS values of Fe³⁺, Na, K, Si, and Li at their respective sites *A*, *B*, *C*, *T1*, and *T2*, respectively.

Special attention was put on the disorder of potential charge carrying species, i.e. Na at *B* and Li at *T2*. Below 400 K, Na is predominantly statically disordered in [001] over two split sites at $z \approx \pm 0.016$. Dominant dynamical disorder of Na at higher temperatures is discernible from diffuse neutron scattering length density residuals at 1123 K in ΔF maps (Fig. 8.2). In accordance, the refinement of ADPs revealed a strongly anisotropic at-site motion of Na above 400 K parallel to the *c*-axis, expressed by $U^{33} \gg U^{11} = U^{22}$ (Fig. 8.3). In fact, refinement of U^{33} at 1123 K gave values of one magnitude larger than at 923 K, indicating a depletion of Na at the *B* site, possibly due to site exchanges. On the other hand, the regression of U^{33} curve towards 0 K leaves a residual indicating static disorder over split sites in the ground state. A partial depletion for the static disorder is also derived from BVS of ≈ 0.86 at *B* site being

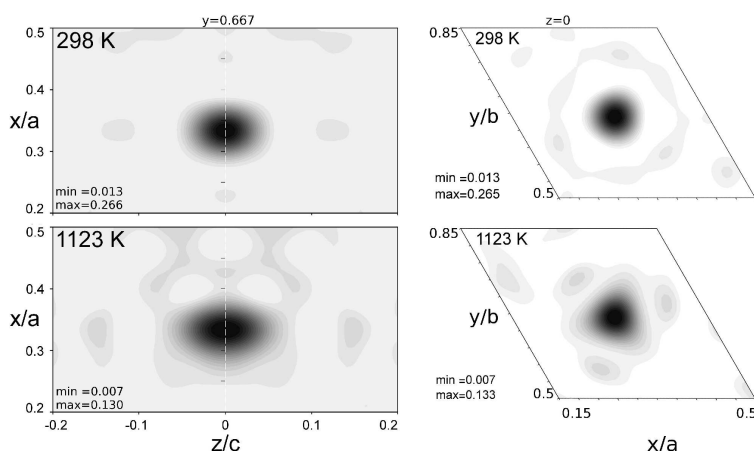


Fig. 8.2.: ΔF maps around the split sites *B* on the (*a-c*) plane (left) and the (*a-b*) plane (right), evaluated with HRNPD data at 298 K and 1123 K with OCC of Na set to 0. Large diffuse residuals around the expected site of Na indicate pathways for Na⁺ in the sugilite-type topology.

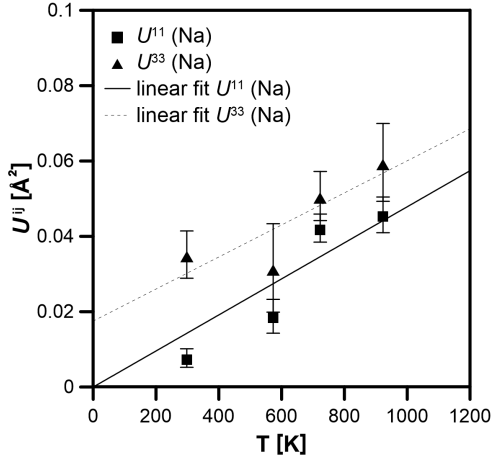


Fig. 8.3.: Anisotropic ADPs for Na refined with HRNPD data between 298 K and 923 K.

significantly lower than the charge of the occupying Na⁺. Albeit it was not possible to refine ADPs of Li below 723 K, Li⁺/Na⁺ dynamics at higher temperatures will be demonstrated in detail in the following section.

8.4. Mechanisms of ionic conduction

ΔF maps were carefully examined for residuals of neutron scattering length densities in order to find interstitial sites for Na and Li (Coh b (Na) = 3.63 fm; Coh b (Li) = -1.91 fm). Negative residuals were found in tetrahedral voids at $\frac{1}{6}, \frac{1}{3}, \frac{1}{4}$ (Fig. 8.4) providing optimal bonding distance of 1.981(3) Å and BVS of ≈ 1.03 for Li. These sites were assigned to Li' sites over which Li⁺ can conduct site exchanges from one $T2$ site to another. The motions of Li in the (a - b) plane is supported by its ADPs at 1123 K. Pronounced motion of Li at $T2$ pointing at Li' sites, i.e. $U^{11} = U^{22} > U^{33}$, is graphically illustrated by thermal ellipsoids in Fig. 8.5a. Fairly short hopping distances of about 2.91 Å are confined by $O3$ - $O3$ edges, which constitute the bottlenecks of $T2$ - Li' site hopping. Site exchanges are favoured at high temperatures considering the strong $O3$ at-site motions perpendicular to the hopping path, as well as the strong increase of $d(O3-O3)$ from RT (3.646 Å) to 1123 K (3.706 Å). Hence, an infinite 2D conduction network via alternating $T2$ and Li' sites is established \perp [001] along the LiO₄ - FeO₆ framework (Fig. 8.5b). Na interstitial sites (Na') were assigned by positive neutron scattering length density residuals at $\frac{1}{2}, \frac{1}{2}, 0$ in the middle between two Na bearing B sites (Fig. 8.6a). These sites provide a fairly suitable average oxygen bonding distance of 2.648(3) Å and BVS of 1.024(6). Interestingly, Na' sites are linked to B sites via continuous positive residuals at $z = 0.08$ marking a diffusion pathway B - Na' - B . The offset of the hopping pathway from the z coordinate of the B site ($z = 0$) is a result of the pronounced dynamic disorder of Na along [001] at B site, i.e. $U^{33} \gg U^{11} = U^{22}$. Furthermore, the oxygen framework offers the widest opening through trapezoidal voids (Fig. 8.6b) with $d(O1-O3) = 4.53$ Å, whereas a direct site exchange is confined by $d(O1-O1)$ only 4.25 Å apart. It is assumed, that the Na⁺ hopping is promoted by temporary widening of the trapezoidal bottleneck through the

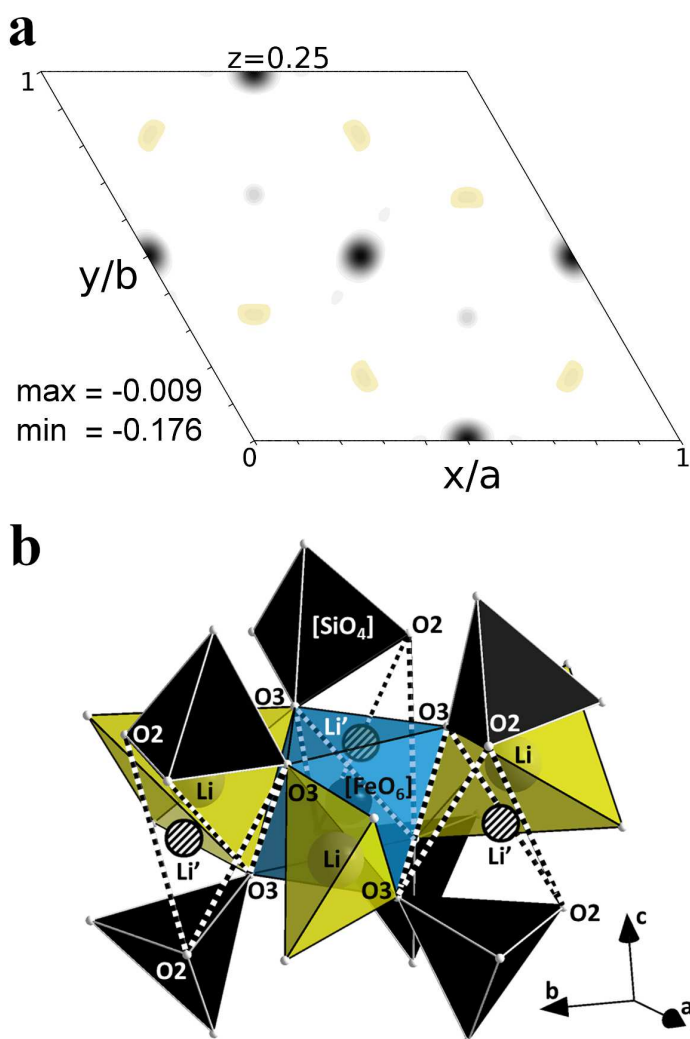


Fig. 8.4.: Negative residuals (yellow) in the ΔF map evaluated from the analysis with 1123K HRNPD data were assigned to a new interstitial site Li' enclosing the centred FeO_6 octahedron (a). Large dark spots represent regular Li sites ($T2$) when its occupancy is set equal to zero. The new Li' sites occupy tetrahedral voids with suitable bonding lengths between two $[SiO_4]$ tetrahedra (b).

significant at-site motions of $O1$ and $O3$. Furthermore, the Na' site exhibits a too short bonding distance to $O1$, i.e. $d(Na'-O1) = 2.132(4)$ Å. Thus, the transient residence of Na^+ at Na' is bound to thermal motions of the oxygen environment causing temporary widening of the cavity. As similarly observed for Li, this gives rise to a 2D Na^+ conduction network $\perp [001]$, wedged in between two $LiO_4 - FeO_6$ framework layers.

The significance of Na^+ charge transport is obvious by comparing σ_{bulk} values obtained with isostructural sogdianite [22] and a massive piece of polycrystalline natural sugilite (Park et al., to be published) (Tab. 8.1). Sogdianite comprises considerably less Na (0.36 *pfu*) compared to sugilite and synthetic $Fe_2Na_2K[Li_3Si_{12}O_{30}]$ (each 2 *pfu*), while Li content 3 (*pfu*) is equal in the solid solution. This is well reflected in that conductivity values of 10^{-3} S cm^{-1} are reached at far lower temperatures (943 K) in polycrystalline sugilite compared to single crystals of sogdianite (1219 K). Surprisingly, synthetic $Fe_2Na_2K[Li_3Si_{12}O_{30}]$ powder and the sogdianite single crystal show similar conductivity values in the range of 10^{-5} S cm^{-1} around 923 - 943 K, despite σ_{bulk} in sogdianite was acquired within the 2D plane of conduction pathways of Li^+

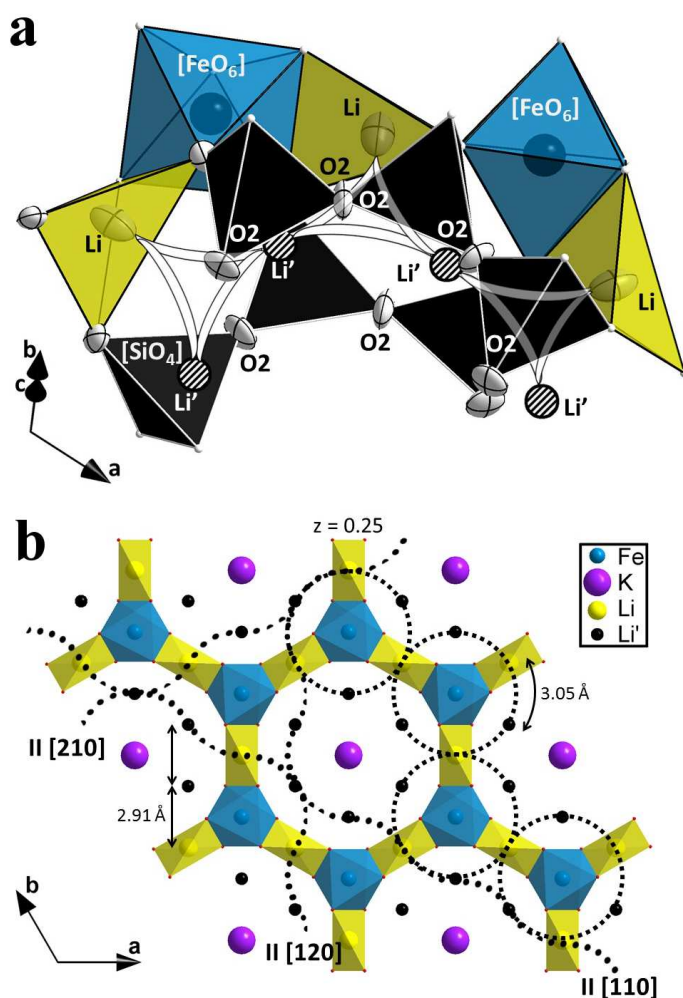


Fig. 8.5.: Schematic illustration of Li⁺ site-exchanges at 1123 K over an interstitial Li' site (a). Hopping pathways constitute an infinite 2D network through regular and interstitial sites in the (a-b) plane (b).

and Na⁺, i.e. \perp [001]. Fe₂Na₂K[Li₃Si₁₂O₃₀] shows σ_{bulk} values about 10^{-2} lower at 963 K compared to the massive natural sugilite sample. This is attributed to extrinsic contributions such as grain boundary charge transfer in the less densely pressed powder pellets of the synthetic counterpart.

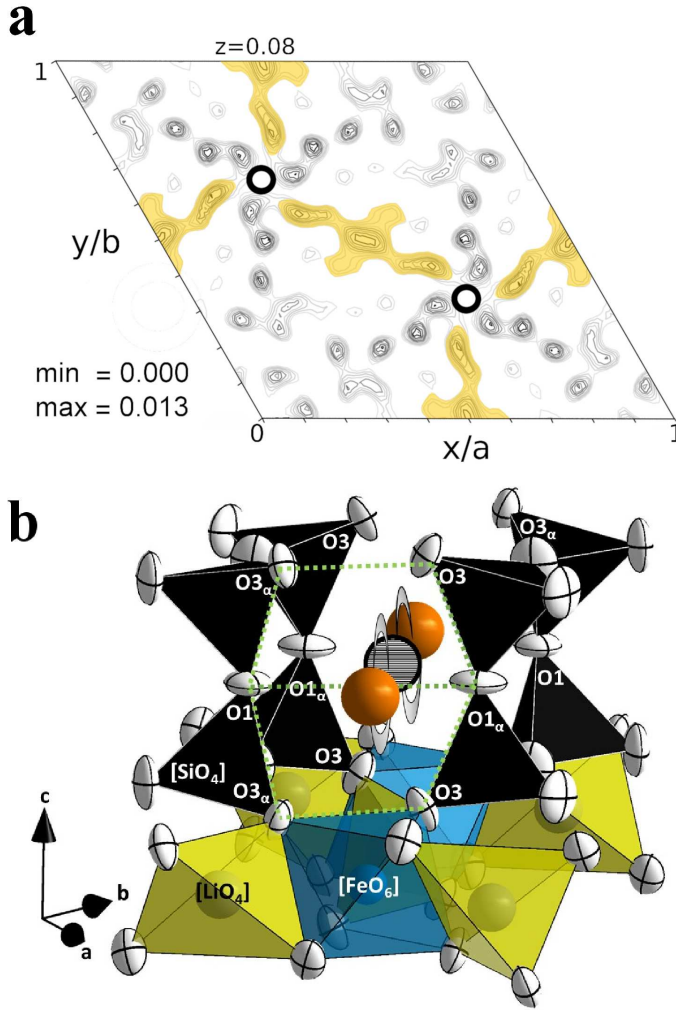


Fig. 8.6.: ΔF maps from HRNPD analysis at $z = 0.08$ slightly above the site B at $z = 0$ (bold black circles) at 1123 K (a). Continuous positive residuals of nsI densities indicate possible Na⁺ diffusion pathways, as highlighted in pale yellow, over the new interstitial site Na' at $(\frac{1}{2}, \frac{1}{2}, 0)$ slightly below the centre of this plot. (b) Side view of [FeO₆-LiO₄] chains upon which the Na⁺ pathway for site-exchanges via $B - Na' - B$ sites is established through $O1-O1-O3-O3$ trapezoidal voids (dashed lines in green) in (b).

Table 8.1.: Comparison of conductivity values and contents of Na and Li in natural sugilite, synthetic sugilite-type powder (Fe₂Na₂K[Li₃Si₁₂O₃₀]), and a sogdianite single crystal.

	σ_{bulk} [S cm ⁻¹]	Na [pfu]	Li [pfu]
sugilite (Park et al., to be published)	1.7×10^{-3} (943 K)	2	3
Fe ₂ Na ₂ K[Li ₃ Si ₁₂ O ₃₀]	1.2×10^{-5} (923 K)	2	3
sogdianite \perp [001] [22]	4.1×10^{-5} (923 K)	0.36	3
	1.2×10^{-3} (1219 K)		

8.5. Conclusion

The study established a synthesis route for the synthetic counterpart of sugilite, Fe₂Na₂K[Li₃Si₁₂O₃₀], via mild hydrothermal conditions. The comprehensive structural analysis using neutron powder diffraction at variable temperature revealed combined and strictly anisotropic 2D Li⁺/Na⁺-ionic conductivity at starting at temperatures of ≈ 720 K. A bulk conductivity value of 1.2×10^{-5} S cm⁻¹ was detected at 923 K from impedance spectra. The unexpected contribution of Na to ionic charge transfer in the milarite-type structure family explains the enhanced bulk conductivity values observed in sugilite compared Na-poor sogdianite. Large single crystals of Fe₂Na₂K[Li₃Si₁₂O₃₀] are desired to exclude extrinsic effects in direction dependent impedance spectroscopy. High ionic conductivity at elevated temperatures in these highly stable compounds makes them interesting candidates for solid electrolytes in long-term storage high-voltage electrochemical cells.

9. Anomalous dielectric response of short hydrogen bonds under pressure: the case of eosphorite, $(\text{Mn}_{0.5}, \text{Fe}_{0.5})^{2+} \text{AlPO}_4(\text{OH})_2 \text{H}_2\text{O}$

9.1. Hydrogen bonds

OH and HOH groups in eosphorite $(\text{Mn}_{0.5}, \text{Fe}_{0.5})^{2+} \text{AlPO}_4(\text{OH})_2 \text{H}_2\text{O}$ give rise to the occurrence of three independent HBs, resolved by detailed structure analysis using neutron scattering methods [21, 35], denoted as HB1, HB2, and HB3 (Fig. 9.1). The strong hydrogen bond HB2 ($\text{O4}-\text{H2}\cdots\text{O4}$) is of particular interest, being very short (2.480(3) Å) and almost linear ($\angle(\text{O4}-\text{H2}-\text{O4}) = 170.1(5)^\circ$). Structure analysis indicated that protons in HB2 are statically disordered between two equally abundant H2 split-sites only 0.35 Å apart. The even distribution of the configurations $\text{O4}-\text{H2}\cdots\text{O4}$ and $\text{O4}\cdots\text{H2}-\text{O4}$ throughout the crystals is in accordance with its centrosymmetric space group $Cmce$, preventing spontaneous polarisation due to proton ordering.

9.2. Dielectric response

Despite the short intrabond distance of HB2, nearly zero *rms* ADP parameter U_1 parallel [100], imply little to absent proton at-site motion along the donor/acceptor axis O4-O4. On the other hand, increased dynamics perpendicular to the latter were resolved at RT [21] impeding proton transfer within HB2. Therefore, spontaneous, or thermally activated site exchanging of protons among H2 split sites is excluded. A correlated disorder-order transition of protons in HB2 hydrogen bonds would give rise to (anti-)ferroelectric transitions. However, phase transition of the title compound between 10 and 300 K is ruled out by the absence of anomalies in the heat capacity curve (Fig. 9.2a).

In materials which do not undergo (anti-)ferroelectric phase transitions, capacitance usually decreases while cooling, since reorientation processes of polar species are aggravated at low temperatures. In this sense, the real part of dielectric response measured in a (ϵ'_a), i.e. parallel to HB2, is remarkable (Fig. 9.2b): ϵ'_a steadily increases between 300 K and a maximum around 70 K. Below 70 K ϵ'_a drops rapidly showing a frequency dispersion around 40 K. The anomaly is ascribed to stimulated proton transfer in the very short HB2 due to the applied alternating electric field (E_{AC}). The applied kHz frequency range is suitable to shift protons in their highly polarisable HBs [97]. The increase of the ϵ'_a curve is explained by the temperature dependence of the length of HB2 ($d(\text{O4}-\text{O4})$) and the root mean square (*rms*) ADPs of protons at H2: As temperature decreases from 300 to 70 K, $d(\text{O4}-\text{O4})$ is significantly shortened (RT: 2.480 Å; 3 K: 2.474(5) Å) [21], lowering the barrier for E_{AC} stimulated proton transfer reactions. Meanwhile, dynamic disorder at H2 is reduced perpendicular to the O4-O4 axis as temperature decreases. The *rms* ADP values U_2 and U_3 are sig-

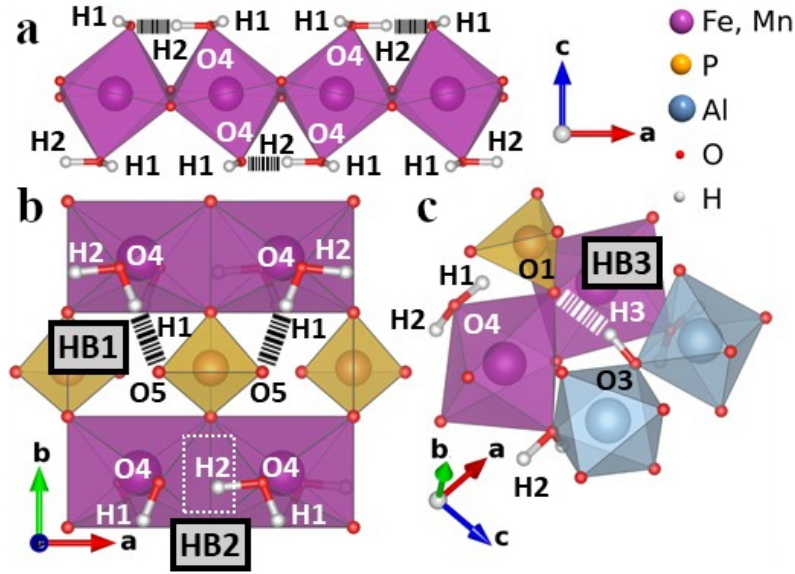


Fig. 9.1.:
 (a) $\text{MO}_4(\text{OH}, \text{H}_2\text{O})_2$ ($\text{M} = \text{Fe}^{2+}, \text{Mn}^{2+}$) octahedra chains with the hydrogen chains with the hydrogen bonds HB2 running quasi parallel in [100] (b) two hydrogen bonds HB1 and HB2 are related to the H_2O group in $\text{H1}-\text{O4}-\text{H2}\dots\text{O4}-\text{H1}$; (c) the long hydrogen bond HB3.

nificantly reduced at 3 K [21] facilitating proton transfer reaction parallel [001]. At temperatures below 70 K, the thermal potential barrier becomes dominant impeding E_{AC} assisted proton transfer within HB2 indicated by decrease of ϵ'_a . The frequency dispersion of the ϵ'_a curve around 40 K is attributed to the final freezing of proton motion at H2.

ϵ'_a seems to be highly sensitive towards small variations in $d(\text{O4}-\text{O4})$. The temperature corresponding to the maximum in ϵ'_a curves (T_m) varied by ± 10 K, depending on the specimen used for repeated measurements. Natural crystals of $(\text{Mn}, \text{Fe})^{2+} \text{AlPO}_4(\text{OH})_2 \text{H}_2\text{O}$ contain chemical zones enriched either in Mn^{2+} or Fe^{2+} [21]. The different ionic radii ($r(\text{Mn}^{2+}) = 0.83 \text{ \AA}$; $r(\text{Fe}^{2+}) = 0.78 \text{ \AA}$ [133]) affect bonding lengths to oxygen at O4 (Fig. 9.1) and consequently length $d(\text{O4}-\text{O4})$. This dependency was further examined by measuring ϵ'_a isobars at mild pressures below 1.6 GPa (Fig. 9.3). T_m could be continuously lowered only slight increments of pressure. As $d(\text{O4}-\text{O4})$ is compressed, E_{AC} field stimulated proton transfer among H2 split sites is continued at lower temperatures. The ϵ'_a curve at 1.51 GPa does not decrease at lowest temperature (2 K), i.e. the loss of polarisability of the hydrogen bond HB2 is not accomplished in the applied temperature and pressure conditions. However, the variation of T_m with pressure is clearly smaller for higher pressures (inset Fig. 9.3), possibly reflecting the onset to symmetrisation of HB2 with $d(\text{O4}-\text{O4})$ close to the critical HB symmetrisation length of 2.39 \AA [29].

9.3. Conclusion

The dielectric response in eosphorite shows the remarkable phenomenon of increasing ϵ'_a values upon cooling from RT in the absence of a ferroelectric phase transition. The ϵ'_a curve is strikingly reminiscent of those measured in compounds undergoing

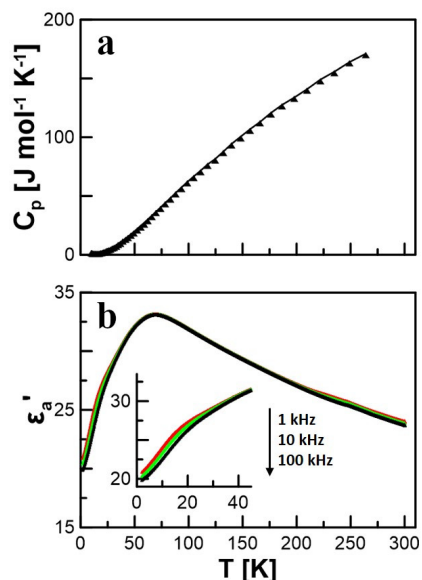


Fig. 9.2.: (a) Heat capacity curve confirms the absence of a phase transition between 10 and 300 K; (b) real part permittivity ϵ'_a recorded from 2 to 300 K with a rate of 2 K min^{-1} along the [100] direction.

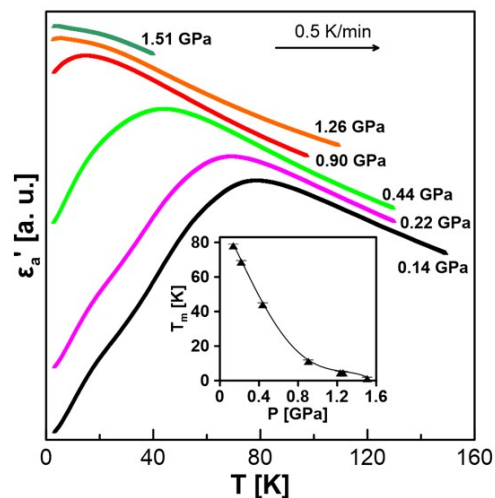


Fig. 9.3.: ϵ'_a (100 kHz) isobars in [100]. Temperature of ϵ'_a maxima (T_m) is characterised by a strong pressure-dependence attributed to the compression of $\text{O4-H2}\cdots\text{O4}$. The inset highlights the shift of T_m as a function of the applied isostatic pressure. Isobars are off-shifted using arbitrary units for clarity.

(anti)-ferroelectric proton order-disorder transitions, e.g. squaric acid ($\text{H}_2\text{C}_2\text{O}_4$) [30, 31]. Further resemblances are provided by $\text{K}_3\text{H}(\text{SeO}_4)$ -type compounds [134, 135], showing similar dielectric response curves in the absence of phase transitions. Having a very similar HB geometry compared to HB2, involvement of proton related quantum-phase transitions are discussed [136–138]. Interestingly, eosphorite showed a Schottky anomaly in heat capacity at $\approx 2.5 \text{ K}$ [21] pointing to finely quantised energy ground states near the absolute temperature minimum. Such anomaly might be related to quantum-effects in HB2, e.g. proton tunnelling. Synthetic counterparts with substitution of H by deuterium with larger ionic radius are desired, to study geometrical effects on the ground state of proton dynamics in HB2.

10. Determination of the hydrogen-bond network and the ferrimagnetic structure of a rockbridgeite-type compound, $\text{Fe}^{2+}\text{Fe}_{3.2}^{3+}(\text{Mn}^{2+}, \text{Zn})_{0.8}(\text{PO}_4)_3(\text{OH})_{4.2}(\text{HOH})_{0.8}$

10.1. A new structure for rockbridgeite-type compounds

A rockbridgeite-type specimen with the relative cationic ratio of Fe: Mn: Zn: P = 4.24(4): 0.58(3): 0.18(3): 3.1(1) was identified using XPD and chemical analysis [36–38].

As shown by structure analysis using XSD, the topology is described by a TO framework made of $3d$ TM octahedra and PO_4 tetrahedra (Fig. 10.1). Face sharing trimers of Fe1-Fe2-Fe1 clusters (*h-cluster*) are interlinked via edges forming infinite chains in *c*. Half occupied Fe3 octahedra and PO_4 tetrahedra connect *h-clusters* in the (*b-c*) and (*a-c*) plains. ^{57}Fe Mößbauer spectroscopy evinced that Fe1 and Fe3 sites with respective multiplicities (*M*) of 1 *pfu* and 2 *pfu*, are completely occupied by Fe^{3+} . 50 % of Fe2 (*M* = 2 *pfu*) are occupied by Fe^{2+} , besides 0.17(1) Fe^{3+} , 0.58(3) Mn and 0.18(3) Zn^{2+} .

These important structural informations were included in XSD and HRNPD data refinements to complete the structure model with hydrogen sites for the first time. Residuals of negative neutron scattering length densities ($\text{Cohb}(\text{H}) = -3.73$ fm) were identified at distances of $\approx 1\text{Å}$ from O3, O5, and O6 sites. The residuals were included into the refinements as four unique hydrogen positions H1, H2, H3, and H4, as illustrated in Fig. 10.2 & Fig. 10.3. H1 shows a full occupation (*M* = 1 *pfu*). Half occupied H2 and H4 sites, each giving rise to *M* = 2 *pfu*, are only present in vacancies due to the 50% occupation of Fe3 sites. Hydrogen is also statically disordered over H3 split sites only 0.64 Å apart, showing a refined occupation of 0.22, i.e. *M* = 0.8 *pfu*. Besides the OH ligands O3-H1, O5-H2, O5-H3 and O6-H4, the configuration of $\angle(\text{H}_3 - \text{O}_5 - \text{H}_3) = 106^\circ$ realises a HOH ligand group. The relative weight of the sum of 5.88 hydrogen *pfu* (≈ 7.76 wt%), fits well to the loss observed in TGA by heating up to 800 K (7.8 wt%). Further anomalies in TGA/DSC curves at higher temperatures were ascribed to small amounts of impurity phases contained in the sample.

Two relevant conclusions could be drawn to suggest a revised mineral formula:

- i) The structure contains statically disordered HOH and OH ligand groups.
- ii) The revelation of a total of 5.88 hydrogen *pfu* fits well to the charge deficit due to selective Fe^{3+} substitution by divalent cations at Fe2: *M* of H3 is equal to 0.88 *pfu*, compensating for the charge deficit of 0.8 *e pfu* induced by replacing Fe^{3+} by Mn^{2+} and Zn^{2+} . Hence, a new general mineral formula for rockbridgeite-type compounds is proposed, $\text{Fe}^{2+}\text{Fe}_{4-x}^{3+}(\text{Mn}^{2+}, \text{Zn})_x(\text{PO}_4)_3(\text{OH})_{5-x}(\text{HOH})_x$, with $x \approx 0.8$ in the present case.

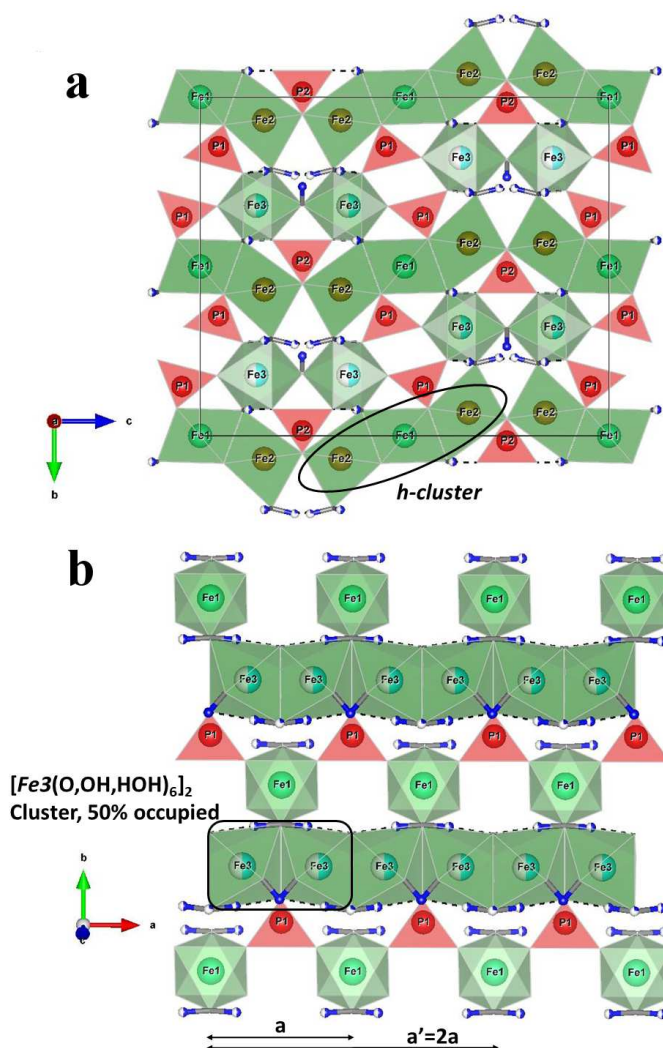


Fig. 10.1.: Structure of Rockbridgeite in the (*b-c*) plane featuring infinite chains of edge-linked trimers of face-sharing $\text{Fe}_3(\text{O}, \text{OH}, \text{HOH})_6$ -octahedra (*h*-clusters) (**a**). Vacancies due to the half occupation of Fe_3 sites in infinite chains running in *a*, host hydrogen bonds forming a network for proton conduction (**b**).

Structural disorder

The structure comprises a high abundance of structural defects. In combination with forbidden weak reflections $h, l = \text{odd}$ in $h0l$ layers, the presence of allowed reflections $h + k = \text{even}$ in $hk0$ layers points at the presence of two polymorphs: Type **A** in space group $Cmcm$ and Type **B** in the subgroup $Pmnm$ causing $h, l = \text{odd}$ reflections in $h0l$. These polymorphs build up stacking faults in the (*b-c*) plane. It is not clear whether these 2D structural defects are in conjunction with the observation of intense diffuse scattering: diffuse streaks were observed $\parallel l$ and $\parallel k$ in $h0l$ and $hk0$ planes, respectively, forbidden to space group $Cmcm$. These streaks point to structural defects in *a*-direction, which are probably related to structural defects at Fe_3 sites.

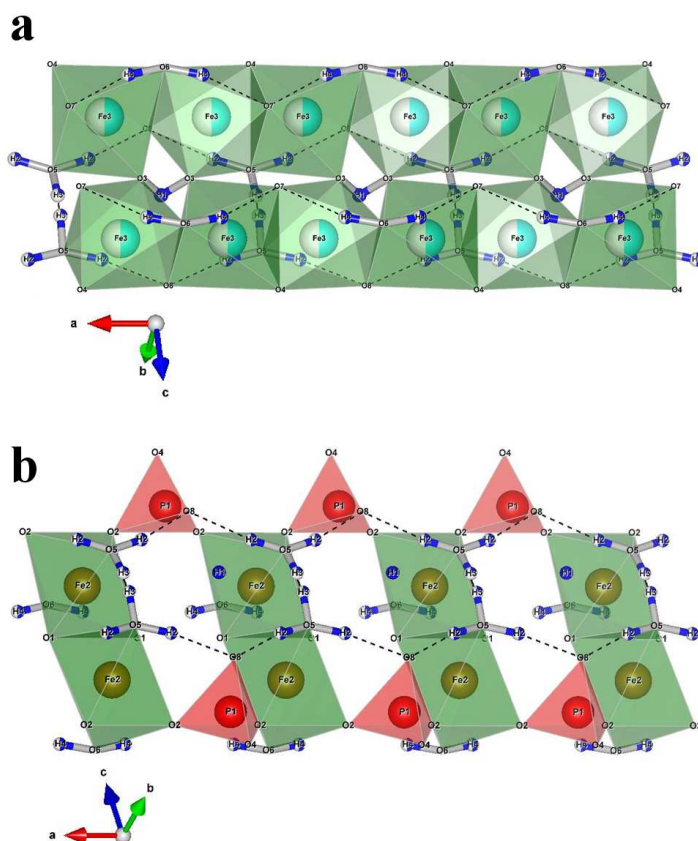


Fig. 10.2.: Honeycomb shaped HBN shown from top (a) and bottom (b) view of $\text{Fe}_3(\text{O}, \text{OH}, \text{HOH})_6$ octahedral chains running in [100].

10.2. Proton conduction in the hydrogen bond network

Structural defects including unoccupied Fe3 sites are particularly interesting in terms of proton conductivity. This is proven from the dramatic increases of real and imaginary parts of the dielectric response above RT (Fig. 10.4).

The newly discovered OH and HOH groups are involved in moderately to strong anisotropic HBs with $d(\text{O}-\text{O}) \approx 2.53 - 2.85 \text{ \AA}$. They form a continuous honeycomb-like HBN extending $\parallel \mathbf{a}$ - direction serving as a basis for proton conduction (Fig. 10.2 and Fig. 10.3). Such network is highly resembling of a so-called *dynamically disordered HBN* (DDHBN) [106] found in superprotonic phases of sulphate and selenite compounds: Protonic conduction through alternately defective Fe3 sites is established by thermally activated fast rotations in the TO framework causing permanent fading, reorientation and re-establishment of hydrogen bonds through which protons are transferred. In this network, the occupation of H2, H3, and H4 by statically disordered protons is strongly dependent on the occurrence of defects at Fe3. In accordance, protonic conduction pathways $\parallel \mathbf{a}$ are meaningfully indicated in bond-valence sum (BVS) mismatch maps (Fig. 10.5), showing cylindrical potential surfaces over which protons would move fast to assure proper BV.

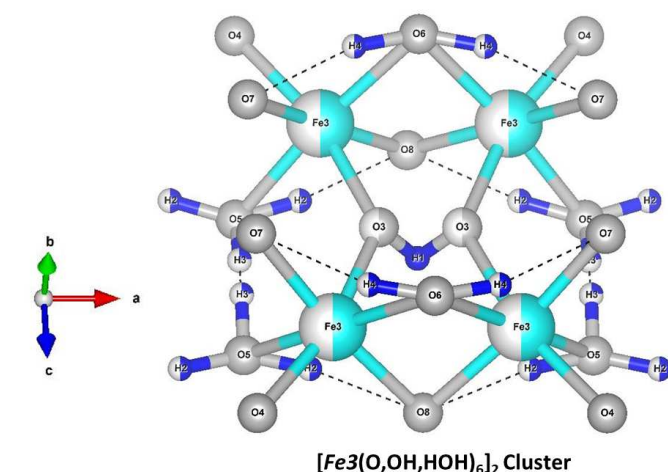


Fig. 10.3.: New H1, H2, H3, and H4 sites among which hydrogen is statically disordered around the quartet of half occupied Fe₃-sites.

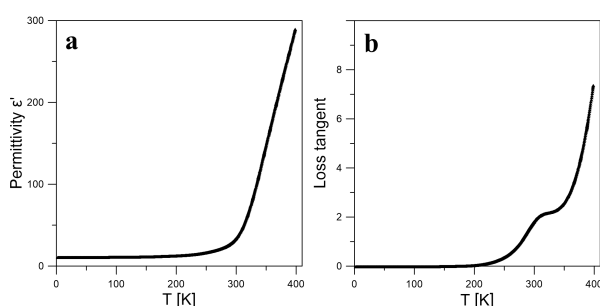


Fig. 10.4.: Simultaneous dramatic increases of real (a) and imaginary (b) parts of the dielectric response at 100 kHz mark the onset of proton conductivity starting around RT.

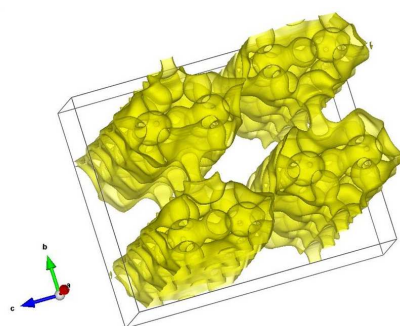


Fig. 10.5.: Possible proton conduction pathways $\parallel a$ are implied from the surface ($V_{\text{pot}} = 1.2 \text{ eV}$) of BV energetic landscape maps. Protons move fast on the surface finding proper BV.

10.3. Ferrimagnetic spin structure below 25 K

The title compound undergoes a paramagnetic to ferrimagnetic phase transition at 81 - 83 K (Fig. 10.6). In accordance, the neutron diffraction pattern evaluated at 25 K contained a modified intensity distribution compared to the pattern collected at 298 K. In the absence of new reflections, the propagation vector $\mathbf{k} = (0,0,0)$ leaves eight possible magnetic space groups (MSGs) for the parental space group Cmcm . Among these, only three MSGs allow net magnetisation for absence of time-reversal along the main crystallographic directions, i.e. $\text{Cmc}'m'$, $\text{Cm}'cm'$, $\text{Cm}'c'm$. In refinements with HRNPD data using these MSGs, $\text{Cm}'c'm$ resulted in the best agreement factors and is regarded as correct (Fig. 10.7).

Regarding the occupation of Fe1 and Fe3 by Fe^{3+} , and Fe2 by mainly Fe^{2+} , the spin-only moments for Fe^{2+} ($4.90 \mu_{\text{B}}$) and Fe^{3+} ($5.92 \mu_{\text{B}}$), are reflected only using MSG $\text{Cm}'c'm$: these values fit well to grading of the refined magnetic moments (\mathbf{M}) at the respective sites, i.e. $\mathbf{M}(\text{Fe}2) = 3.0 \mu_{\text{B}}$ and $\mathbf{M}(\text{Fe}1) = \mathbf{M}(\text{Fe}3) = 4.3 \mu_{\text{B}}$. The complex

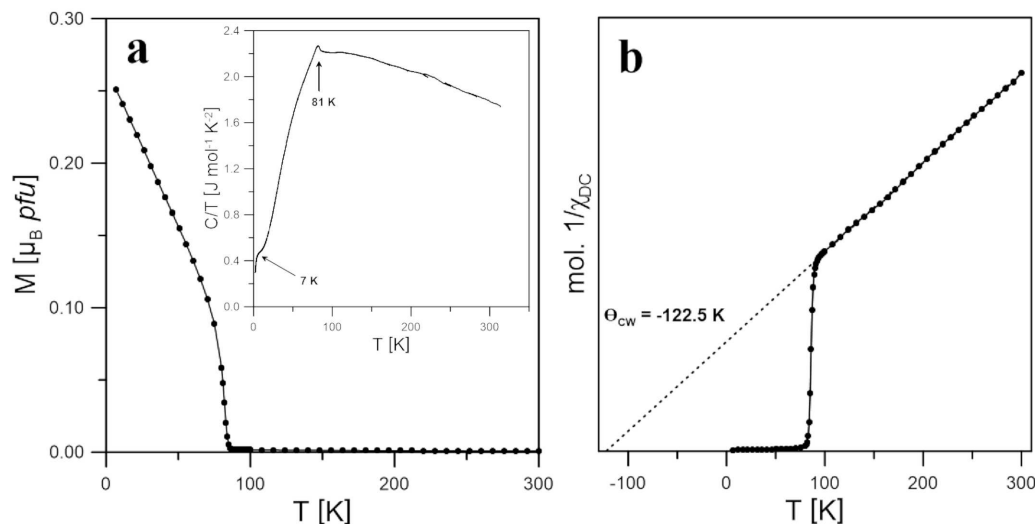


Fig. 10.6.: (a) In accordance with an anomaly in heat capacity curve (inset), ZFC magnetisation curve between 8 K and 300 K indicates a magnetic transition at around 81 - 83 K. The spontaneous net magnetic moment is associated with a ferrimagnetic ordering, as inferred from the negative Curie-Weiss Temperature obtained from extrapolation of the inverse magnetic susceptibility χ^{-1} (b).

final spin structure built up by three sublattices is shown in Fig. 10.8. It is the product of various competing magnetic exchange interactions (see. Sec. 6.2) among which two seem to be dominant (Fig. 10.9):

i) Spins in Fe1-Fe2-Fe1 trimers (*h-clusters*) are ferromagnetically aligned. The coupling could be ascribed to direct exchange interactions through overlap of $3d$ orbitals of the very narrow Fe atoms (2.78 Å) [139]. On the other hand, DE mechanism through the oxygens at O2 and O6 are conceivable within pairs of Fe1 and Fe2 [2]. Interestingly, the involved $\text{Fe}^{2+}/\text{Fe}^{3+}$ intervalence charge transfer was proven via UV/VIS absorption bands which intensified around the magnetic transition temperature [43, 44].

ii) The second endemic correlations are strong superexchange interactions causing AFM couplings in Fe3-Fe3 octahedra and in chains of Fe3-Fe1 and Fe3-Fe2 octahedra running in [010] [113]. These superexchange interactions via octahedral corners, e.g. $\angle(\text{Fe2-O5-Fe3}) = 132.0^\circ$, are responsible for the ferromagnetic coupling of two adjacent *h-clusters* in [010]. They are also the reason for the unusual AFM coupling of two *h-clusters* in [001] via Fe2-O1-Fe2 interactions ($\angle(\text{Fe2-O1-Fe2}) = 99.2^\circ$): 90° superexchange interactions are usually FM [140], but much weaker compared to AFM superexchange coupling via octahedral corners, as mentioned above.

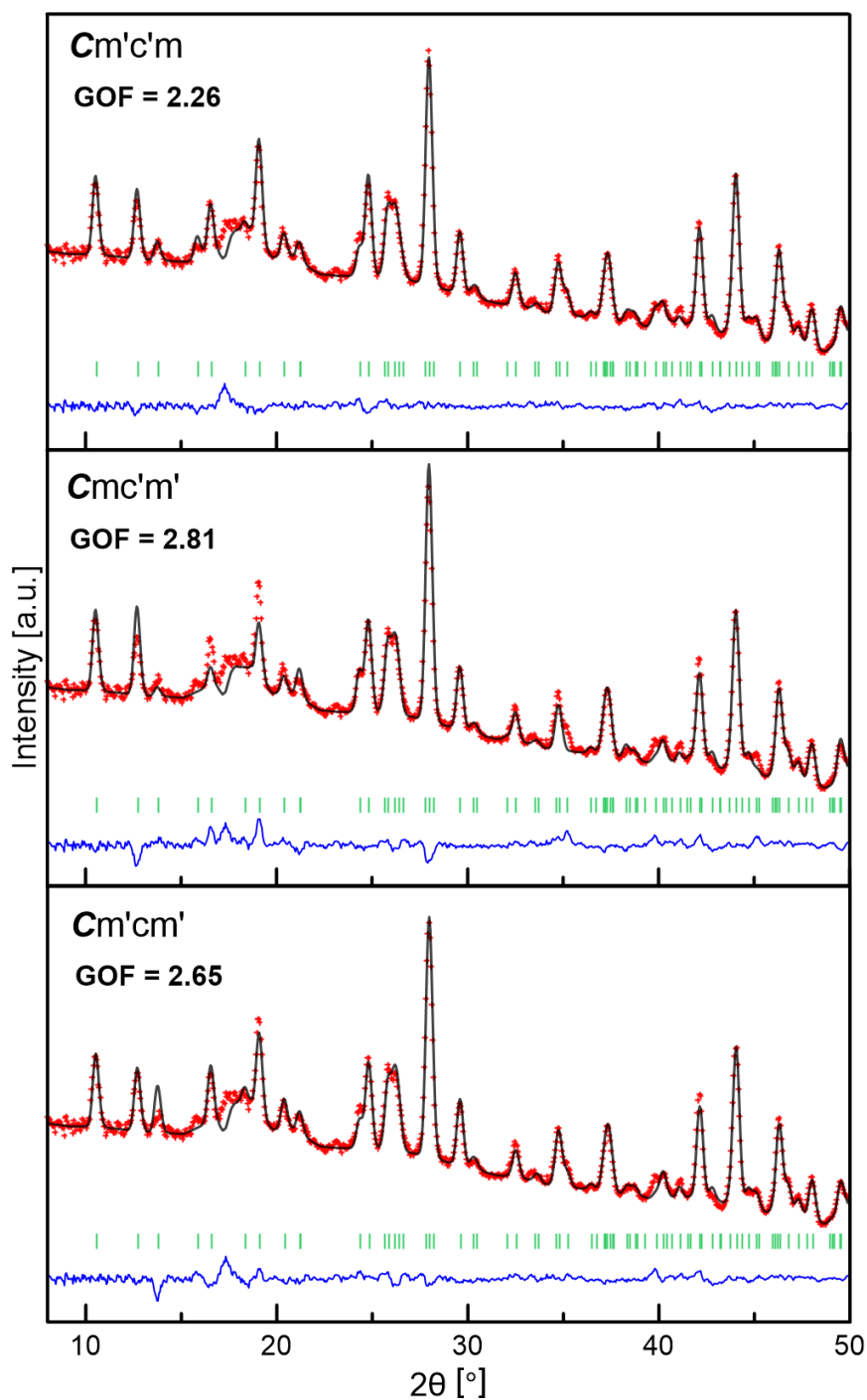


Fig. 10.7.: Refinements with HRNPD data ($\lambda = 1.5483 \text{ \AA}$) from 25 K using those three possible MSGs which allow net magnetisation. Best agreement factors (GOF) were obtained for $\text{Cm}'\text{c}'\text{m}$ with net magnetisation in c -direction.

10. Determination of the hydrogen-bond network and the ferrimagnetic structure of a rockbridgeite-type compound, $\text{Fe}^{2+}\text{Fe}_{3.2}^{3+}(\text{Mn}^{2+}, \text{Zn})_{0.8}(\text{PO}_4)_3(\text{OH})_{4.2}(\text{HOH})_{0.8}$

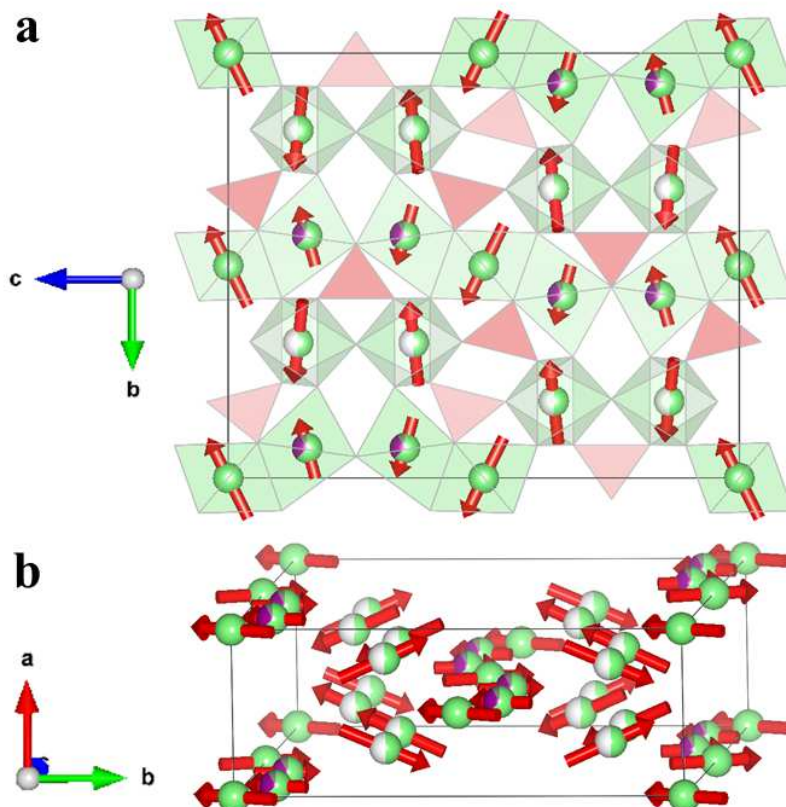


Fig. 10.8.: Magnetic spin order from the refinement in MSG $Cm'c'm$ discloses three magnetic sublattices from Fe1 (filled spheres), Fe2 (mixed occupation), and Fe3 (half filled spheres) in the $(b-c)$ plane (a) and roughly $(a-b)$ plane (b). A net magnetisation in c -direction is established.

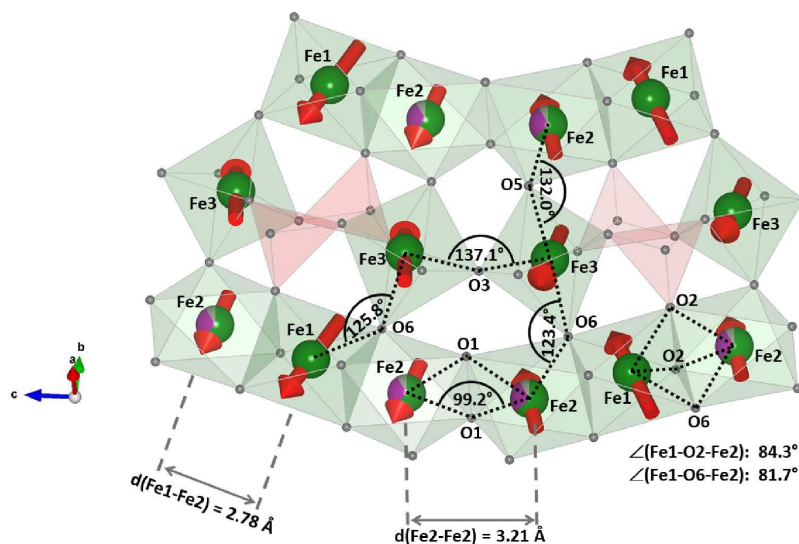


Fig. 10.9.: Geometrical review on possible superexchange interactions among FeO_6 octahedra and double exchange within h -clusters.

10.4. Conclusion

Comprehensive investigations of magnetic and dielectric properties of the rockbridgeite-series were performed and reconciled with results from neutron powder diffraction data analyses. For the first time hydrogen sites were determined, completing the structure model. The abundance of hydrogen appears to be strictly correlated with the substitution of Fe^{3+} by divalent $3d$ TM cations, suggesting a new general formula for this series: $\text{Fe}^{2+}\text{Fe}_{4-x}^{3+}(\text{Mn}^{2+}, \text{Zn})_x(\text{PO}_4)_3(\text{OH})_{5-x}(\text{HOH})_x$.

High proton conductivity is indicated by a dramatical increase of the dielectric response starting at RT. It is expected that the newly revealed dynamically disordered hydrogen bond network gives rise to superprotonic behaviour. The ferrimagnetic structure was solved below the transition temperature of 81 - 83 K as the first in a row of closely related phosphatic oxyhydroxides, such as barbosalite and lipscombite. Additional investigations are required to illuminate the nature of another transition around 7 K. With proton conductivity starting around RT, the title compound deserves further investigation as a suitable electrolyte material for PEMFCs .

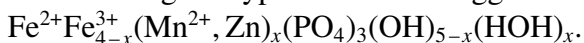
11. Conclusion

The present thesis demonstrates the relevance of mineral prototype structures for material engineering of electrochemical active materials, but also in exploratory research of proton dynamics and magnetism. Three case studies cover specific to comprehensive descriptions of diverse physical properties which can be understood by subtle nuclear and magnetic structure analyses.

The synthetic analogue to sugilite, $\text{Fe}_2\text{Na}_2\text{K}[\text{Li}_3\text{Si}_{12}\text{O}_{30}]$, could be synthesised for the first time using hydrothermal method below 240°C . It could be shown that the bulk conductivity in the sogdianite-sugilite solid solution can be increased with higher concentration of Na. Bulk ionic conductivity with an activation energy of $\approx 1.22(2)$ eV started at around 723 K and peaked in 10^{-5} S cm^{-1} at 923 K as shown via impedance spectroscopy. These findings were supported by structure analysis with neutron diffraction data recorded between 298 K and 1123 K: combined Na^+ and Li^+ charge migration in these materials is explained by hopping over interstitial sites found in ΔF maps. With its high thermal stability and chemical flexibility, these materials are considered interesting candidates for high-temperature high-voltage battery systems.

The real part of the permittivity (ϵ') obtained with Eosphorite, $(\text{Mn}, \text{Fe})^{2+}\text{AlPO}_4(\text{OH})_2 \cdot \text{H}_2\text{O}$, showed an exceptional increase while cooling to ≈ 70 K, despite the absence of an antiferroelectric phase transition. The anomaly arises for the interplay of electric field stimulated proton transfer within a very short hydrogen bond ($2.480(2)$ Å) and the temperature dependent at-site motions of its proton. The high sensitivity of stimulated proton transfer towards only small variations in the short hydrogen bond length is reflected in ϵ' isobars obtained at mild isostatic pressures. It was shown that the anomaly can be shifted below 2 K applying 1.51 GPa. This indicates extended field stimulated proton transfer at lower temperatures for the compression of the short hydrogen bond. These findings open new possibilities to investigate quantum effects in short hydrogen bonds.

Finally, this thesis comprises an extensive characterisation of a rockbridgeite-type compound, $\text{Fe}^{2+}\text{Fe}_{3.2}^{3+}(\text{Mn}^{2+}, \text{Zn})_{0.8}(\text{PO}_4)_3(\text{OH})_{4.2}(\text{HOH})_{0.8}$. For the first time, the complete structure model is presented, including four new sites for hydrogen using neutron powder diffraction. The presence of HOH groups is strictly correlated to the selective substitution of Fe^{3+} by divalent cations. Therefore, a new generic formula for rockbridgeite-type minerals is suggested:



An infinite honeycomb-like network of hydrogen bonds is established in the oxyhydroxide topology. Strongly depending on structural defects at octahedral Fe^{3+} sites, the HBN resembles those in superprotonic sulfates and selenites. Fast rotations in the TO framework accompanied by a permanent alteration of the HBN provide low-energy conduction pathways. High proton conductivity is reflected by steep increases in curves of real and imaginary parts of the permittivity starting slightly below RT.

Characterisation of magnetic properties show a paramagnetic to ferrimagnetic transition at 81 - 83 K. The magnetic structure could be solved from diffraction data acquired at 25 K showing a weak net magnetic moment.

The new findings on rockbridgeite-type compounds are interesting for various aspects:

- i) Ferrimagnetism is new to phosphatic oxyhydroxide structures. The evaluated spin structure is probably similar to a variety of related structures, e.g. lipscombite, barbosalite.
- ii) With its thermal stability of about 600°C in Ar, rockbridgeite is highly interesting for the development of novel proton exchange membranes.

These scientific cases can be divided in groups of application-oriented and fundamental research-oriented topics. Ionic and protonic conduction capabilities of the compounds in studies #1 and #3, respectively, are of relevance for ion battery and fuel cell applications as introduced in Cha. 3.

On the other hand, the new magnetic spin structure provided in study #3, as well as the dielectric anomaly for proton dynamics in study #2 rather address questions of fundamental material science. Prior to find suitable applications, these studies lay the groundwork for further investigations and material engineering.

The special relevance of finding novel tunable magnetic materials is readily apparent considering their ubiquity in consumer electronics, sensors and actuators, recording media, permanent magnets, random access memory, or microwave applications.

Study #2 is of importance to understand local proton dynamics in very short HBs as a key to order-disorder (anti-)ferroelectric transitions, quantum-critical proton behaviour, and proton conductors.

Engineering of functional materials rests upon the detailed structure analysis disclosing the underlying mechanisms of observed prototype properties. Therefore, detailed structure analysis via diffraction techniques is necessary using X-rays and neutrons. Nuclear and magnetic structures provide the frame for local or long-range interactions explaining physical behaviours. Comprehensive structure-property relations allow to design better performing materials.

Bibliography

- [1] J. M. D. Coey. Louis Néel: Retrospective (invited). *Journal of Applied Physics*, 93(10):8224–8229, 2003.
- [2] C. Zener. Interaction between the d-Shells in the Transition Metals. II. Ferromagnetic Compounds of Manganese with Perovskite Structure. *Physical Review*, 82(3):403–405, 1951.
- [3] J. M. D. Coey, M. Venkatesan, and H. Xu. Introduction to Magnetic Oxides. In *Functional Metal Oxides*, pages 1–49. Wiley-VCH Verlag GmbH & Co. KGaA, Weinheim, Germany, 2013.
- [4] Y. Meesala, A. Jena, H. Chang, and R. S. Liu. Recent Advancements in Li-Ion Conductors for All-Solid-State Li-Ion Batteries. *ACS Energy Letters*, 2(12):2734–2751, 2017.
- [5] L. Bindi, M. Evain, A. Pradel, S. Albert, M. Ribes, and S. Menchetti. Fast ion conduction character and ionic phase-transitions in disordered crystals: The complex case of the minerals of the pearceite-polybasite group. *Physics and Chemistry of Minerals*, 33(10):677–690, 2006.
- [6] J. Valasek. Piezo-Electric and Allied Phenomena in Rochelle Salt. *Physical Review*, 17(4):475–481, 1921.
- [7] S. Horiuchi and Y. Tokura. Organic ferroelectrics. *Nature materials*, 7(5):357–366, 2008.
- [8] W. D. Ratcliff and J. W. Lynn. Multiferroics. In F. Fernandez-Alonso and D. L. Price, editors, *Neutron Scattering - Magnetic and Quantum Phenomena*, volume 48, pages 291–338. Elsevier, 2015.
- [9] K. Taniguchi, N. Abe, H. Umetsu, H. Aruga Katori, and T. Arima. Control of the magnetoelectric domain-wall stability by a magnetic field in a multiferroic MnWO_4 . *Physical Review Letters*, 101:2–5, 2008.
- [10] K. Taniguchi, N. Abe, S. Ohtani, and T. Arima. Magnetoelectric memory effect of the non-polar phase with collinear spin structure in multiferroic MnWO_4 . *Physical Review Letters*, 102(14):1–4, 2009.
- [11] T. Kimura, J. C. Lashley, and A. P. Ramirez. Inversion-symmetry breaking in the non-collinear magnetic phase of the triangular-lattice antiferromagnet CuFeO_2 . *Physical Review B*, 73(22):220401, 2006.
- [12] M. Lorenz, M. S. Ramachandra Rao, T. Venkatesan, E. Fortunato, P. Barquinha, R. Branquinho, D. Salgueiro, R. Martins, E. Carlos, A. Liu, F. K. Shan, M. Grundmann, H. Boschker, J. Mukherjee, M. Priyadarshini, N. DasGupta, D. J. Rogers, F. H. Teherani, E. V. Sandana, P. Bove, K. Rietwyk, A. Zaban, A. Veziridis, A. Weidenkaff, M. Muralidhar, M. Murakami, S. Abel, J. Fompeyrine, J. Zuniga-Perez, R. Ramesh, N. A. Spaldin, S. Ostanin, V. Borisov, I. Mertig, V. Lazenka, G. Srinivasan, W. Prellier, M. Uchida, M. Kawasaki, R. Pentcheva, P. Gegenwart, F. Miletto Granozio, J. Fontcuberta, and N. Pryds. The 2016 oxide electronic materials and oxide interfaces roadmap. *Journal of Physics D: Applied Physics*, 49(43):433001, 2016.
- [13] N. Izyumskaya, Y. Alivov, and H. Morkoç. Oxides, Oxides, and More Oxides: High- κ Oxides, Ferroelectrics, Ferromagnetics, and Multiferroics. *Critical Reviews in Solid State and Materials Sciences*, 34(3-4):89–179, 2009.
- [14] Haibo Guo and Amanda S. Barnard. Thermodynamics of Iron Oxides and Oxyhydroxides in Different Environments. In D. Faivre, editor, *Iron Oxides*, pages 269–292. Wiley-VCH Verlag GmbH & Co. KGaA, Weinheim, Germany, 2016.
- [15] P. H. Domingues, L. de F. Moreira, E. Mattievich, and B. Sarkissian. Magnetism in the series $(\text{Fe}_x\text{Mn}_{1-x})_5(\text{PO}_4)_2(\text{PO}_4\text{H})_2(\text{H}_2\text{O})_4$. *Journal of Magnetism and Magnetic Materials*, 167(1-2):87–92, 1997.

BIBLIOGRAPHY

- [16] H.-I. Hsiang, L.-T. Mei, and Y.-H. Lin. Formation and growth of manganese phosphate passivation layers for NTC ceramics. *Journal of Alloys and Compounds*, 484(1-2):723–728, 2009.
- [17] C.-M. Wang, H.-C. Liao, and W.-T. Tsai. Effect of heat treatment on the microstructure and electrochemical behavior of manganese phosphate coating. *Materials Chemistry and Physics*, 102(2-3):207–213, 2007.
- [18] H. Yin, F. Liu, X. Chen, X. Feng, W. Tan, and G. Qiu. Synthesis of hureaulite by a reflux process at ambient temperature and pressure. *Microporous and Mesoporous Materials*, 153:115–123, 2012.
- [19] G. J. Redhammer, G. Tippelt, G. Roth, We. Lottermoser, and G. Amthauer. Mössbauer spectroscopy of barbosalite Structure and Mo. *Physics and Chemistry of Minerals*, 27(6):419–429, 2000.
- [20] Y. Song, P. Y. Zavalij, N. A. Chernova, and M. S. Whittingham. Synthesis, Crystal Structure, and Electrochemical and Magnetic Study of New Iron (III) Hydroxyl-Phosphates, Isostructural with Lipscombite. *Chemistry of Materials*, 17(5):1139–1147, 2005.
- [21] D. Behal, B. Röska, S.-H. Park, B. Pedersen, G. Benka, Ch. Pfeleiderer, Y. Wakabayashi, and T. Kimura. The first study of antiferromagnetic eosphorite-childrenite series $(\text{Mn}_{1-x}\text{Fe}_x)\text{AlPO}_4(\text{OH})_2\text{H}_2\text{O}$ ($x=0.5$). *Journal of Magnetism and Magnetic Materials*, 428:17–27, 2017.
- [22] S.-H. Park, M Hoelzel, H Boysen, and E Schmidbauer. Lithium conductivity in an Li-bearing double-ring silicate mineral, sogdianite. *Journal of Solid State Chemistry*, 180(4):1306–1317, 2007.
- [23] W. C. Forbes, W. H. Baur, and A. A. Khan. Crystal Chemistry of milarite- type minerals. *American Mineralogist*, 57:463–472, 1972.
- [24] O. C. Gagné and F. C. Hawthorne. Chemographic Exploration of the Milarite-Type Structure. *The Canadian Mineralogist*, 54(5):1229–1247, 2016.
- [25] N. Murakami, T. Kato, and Y. Miura. Sugilite, a new silicate mineral from Iwagi Islet, Southwest Japan. *Mineralogical Journal*, 8(2):110–121, 1976.
- [26] P. J. Dunn, J. J. Brummer, and H. Belsky. Sugilite, a second occurrence: Wessels mine, Kalahari manganese field, Republic of South Africa. *Canadian Mineralogist*, 18:37–39, 1980.
- [27] A. M. Clark, E. E. Fejer, A. G. Couper, G. S. Bearne, and V. K. Din. Additional data on Sugilite. *Mineralogical Magazine*, 43:947–949, 1980.
- [28] S. Horiuchi, R. Kumai, and Y. Tokura. Hydrogen-bonded donor–acceptor compounds for organic ferroelectric materials. *Chemical Communications*, 0(23):2321–2329, 2007.
- [29] T. Steiner. The hydrogen bond in the solid state. *Angewandte Chemie International Edition*, 41(1):49–76, 2002.
- [30] Y. Moritomo, Y. Tokura, H. Takahashi, and N. Mori. Quantum paraelectricity and subsequent disappearance of bond alternation of molecule caused by proton dynamics in squaric acid crystal. *Physical Review Letters*, 67(15):2041–2044, 1991.
- [31] E.J. Samuelsen and D. Semmingsen. Squaric acid, a two-dimensional hydrogen-bonded material with a phase transition. *Solid State Communications*, 17(2):217–219, 1975.
- [32] W. Xu, E. Greenberg, G. K. Rozenberg, M. P. Pasternak, E. Bykova, T. Boffa-Ballaran, L. Dubrovinsky, V. Prakapenka, M. Hanfland, O. Y. Vekilova, S. I. Simak, and I. A. Abrikosov. Pressure-induced hydrogen bond symmetrization in iron oxyhydroxide. *Physical Review Letters*, 111(17):1–5, 2013.
- [33] A. W. Hanson. The crystal structure of eosphorite. *Acta Crystallographica*, 13:384–387, 1960.
- [34] M. A. Hoyos, T. Calderon, I. Vergara, and J. Garcia-Solé. New Structural and Spectroscopic Data for Eosphorite. *Mineralogical Magazine*, 57(387):329–336, 1993.

BIBLIOGRAPHY

- [35] G. D. Gatta, G. Nenert, and P. Vignola. Coexisting hydroxyl groups and H₂O molecules in minerals: A single-crystal neutron diffraction study of eosphorite, MnAlPO₄(OH)₂·H₂O. *American Mineralogist*, 98(7):1297–1301, 2013.
- [36] P. B. Moore. Crystal Chemistry of the Basic Iron Phosphates. *American Mineralogist*, 55(1-2):135–169, 1970.
- [37] G. J. Redhammer, G. Roth, G. Tippelt, M. Bernroider, W. Lottermoser, G. Amthauer, and R. Hochleitner. Manganian rockbridgeite Fe_{4.32}Mn_{0.62}Zn_{0.06}(PO₄)₃(OH)₅: structure analysis and ⁵⁷Fe Mössbauer spectroscopy. *Acta Crystallographica Section C Crystal Structure Communications*, 62(3):i24–i28, 2006.
- [38] P. Elliott, U. Kolitsch, G. Giester, E. Libowitzky, C. McCammon, A. Pring, W. D. Birch, and J. Brugger. Description and crystal structure of a new mineral - plimerite, ZnFe₄³⁺(PO₄)₃(OH)₅ - the Zn-analogue of rockbridgeite and frondelite, from Broken Hill, New South Wales, Australia. *Mineralogical Magazine*, 73(1):131–148, 2009.
- [39] E. Mattievich, N. V. Vugman, L. M. A. Diehl, and J. Danon. Analytical interpretation of temperature dependent combined quadrupolar and magnetic hyperfine interaction in Fe²⁺Fe₃²⁺(PO₄)₂(OH)₂ (barbosalite). *Journal de Physique*, 40(12):1195–1198, 1979.
- [40] M. Grodzicki and G. Amthauer. Electronic and magnetic structure of vivianite: cluster molecular orbital calculations. *Physics and Chemistry of Minerals*, 27(10):694–702, 2000.
- [41] P. Y Song, Y. Zavalij, M. S., and M. S. Whittingham. New iron (III) phosphate phases: crystal structure and electrochemical and magnetic properties. *Inorganic Chemistry*, 41(22):5778–5786, 2002.
- [42] M. S. Whittingham, Y. Song, S. Lutta, P. Y. Zavalij, and N. A. Chernova. Some transition metal (oxy)phosphates and vanadium oxides for lithium batteries. *Journal of Materials Chemistry*, 15(33):3362, 2005.
- [43] G. Amthauer and G. R. Rossman. Mixed valence of iron in minerals with cation clusters. *Physics and Chemistry of Minerals*, 11(1):37–51, 1984.
- [44] S. M. Mattson and G. R. Rossman. Identifying characteristics of charge transfer transitions in minerals. *Physics and Chemistry of Minerals*, 14(1):94–99, 1987.
- [45] S. Singh. Selective CO oxidation over Fe₅(PO₄)₃(OH)₅ supported Pt catalyst: Kinetic and mechanistic studies. *Indian Journal of Chemistry*, 53A:511–515, 2014.
- [46] R. Hausbrand, G. Cherkashinin, H. Ehrenberg, M. Gröting, K. Albe, C. Hess, and W. Jaegermann. Fundamental degradation mechanisms of layered oxide Li-ion battery cathode materials: Methodology, insights and novel approaches. *Materials Science and Engineering B: Solid-State Materials for Advanced Technology*, 192(C):3–25, 2015.
- [47] J. Vetter, P. Novák, M.R. Wagner, C. Veit, K.-C. Möller, J.O. Besenhard, M. Winter, M. Wohlfahrt-Mehrens, C. Vogler, and A. Hammouche. Ageing mechanisms in lithium-ion batteries. *Journal of Power Sources*, 147(1-2):269–281, 2005.
- [48] B. Dunn, H. Kamath, and J.-M. Tarascon. Electrical Energy Storage for the Grid: A Battery of Choices. *Science*, 334(6058):928–935, 2011.
- [49] Y. Nishi. Lithium ion secondary batteries; past 10 years and the future. *Journal of Power Sources*, 100(1-2):101–106, 2001.
- [50] J.-Y. Hwang, S.-T. Myung, and Y.-K. Sun. Sodium-ion batteries: present and future. *Chemical Society Reviews*, 46(12):3529–3614, 2017.
- [51] P. Adelhelm, P. Hartmann, C. L. Bender, M. Busche, C. Eufinger, and J. Janek. From lithium to sodium: cell chemistry of room temperature sodium–air and sodium–sulfur batteries. *Beilstein Journal of Nanotechnology*, 6(1):1016–1055, 2015.
- [52] H. Pan, Y.-S. Hu, and L. Chen. Room-temperature stationary sodium-ion batteries for large-scale electric energy storage. *Energy & Environmental Science*, 6(8):2338, 2013.

- [53] C. Vaalma, D. Buchholz, M. Weil, and S. Passerini. A cost and resource analysis of sodium-ion batteries. *Nature Reviews Materials*, 3(18013), 2018.
- [54] G. Markl. *Minerale und Gesteine*. Springer, Berlin, Heidelberg, 2011.
- [55] D. Aurbach, Y. Talyosef, B. Markovsky, E. Markevich, E. Zinigrad, L. Asraf, J. S. Gnanaraj, and H.-J. Kim. Design of electrolyte solutions for Li and Li-ion batteries: a review. *Electrochimica Acta*, 50(2-3):247–254, 2004.
- [56] N. Yabuuchi, K. Kubota, M. Dahbi, and S. Komaba. Research Development on Sodium-Ion Batteries. *Chemical Reviews*, 114(23):11636–11682, 2014.
- [57] N. Kamaya, K. Homma, Y. Yamakawa, M. Hirayama, R. Kanno, M. Yonemura, T. Kamiyama, Y. Kato, S. Hama, K. Kawamoto, and A. Mitsui. A lithium superionic conductor. *Nature Materials*, 10(9):682–686, 2011.
- [58] Z. Zhang, E. Ramos, F. Lalère, A. Assoud, K. Kaup, P. Hartman, and L. F. Nazar. $\text{Na}_{11}\text{Sn}_2\text{PS}_{12}$: a new solid state sodium superionic conductor. *Energy & Environmental Science*, 11(1):87–93, 2018.
- [59] X. Lin, M. Salari, L. M. R. Arava, P. M. Ajayan, and M. W. Grinstaff. High temperature electrical energy storage: advances, challenges, and frontiers. *Chemical Society Reviews*, 45(21):5848–5887, 2016.
- [60] A. D. Robertson, A. R. West, and A. G. Ritchie. Review of crystalline lithium-ion conductors suitable for high temperature battery applications. *Solid State Ionics*, 104(1-2):1–11, 1997.
- [61] M. L. Di Vona and P. Knauth. Introduction and Overview: Protons, the Nonconformist Ions. In *Solid State Proton Conductors*, pages 1–4. John Wiley & Sons, Ltd, Chichester, UK, 2012.
- [62] S. J. Hamrock and M. A. Yandrasits. Proton Exchange Membranes for Fuel Cell Applications. *Journal of Macromolecular Science, Part C: Polymer Reviews*, 46(3):219–244, 2006.
- [63] A. Kraysberg and Y. Ein-Eli. Review of Advanced Materials for Proton Exchange Membrane Fuel Cells. *Energy & Fuels*, 28(12):7303–7330, 2014.
- [64] K. D. Kreuer, S. J. Paddison, E. Spohr, and M. Schuster. Transport in Proton Conductors for Fuel-Cell Applications: Simulations, Elementary Reactions, and Phenomenology. *Chemical Reviews*, 104(10):4637–4678, 2004.
- [65] S. Bose, T. Kuila, T. X. H. Nguyen, N. H. Kim, K.-t. Lau, and J. H. Lee. Polymer membranes for high temperature proton exchange membrane fuel cell: Recent advances and challenges. *Progress in Polymer Science*, 36(6):813–843, 2011.
- [66] Y. Jiang, Y. Xie, and H. Guo. A computational study of energy barriers of structural transformations and hydrogen transfer in boehmite. *RSC Advances*, 8(5):2377–2384, 2018.
- [67] X. Meng, H.-N. Wang, S.-Y. Song, and H.-J. Zhang. Proton-conducting crystalline porous materials. *Chemical Society Reviews*, 46(2):464–480, 2017.
- [68] P. Knauth and M. L. Di Vona. Inorganic Solid Proton Conductors. In *Solid State Proton Conductors*, pages 371–397. John Wiley & Sons, Ltd, Chichester, UK, 2012.
- [69] K. D. Kreuer, M. Hampele, K. Dolde, and A. Rabenau. Proton transport in some heteropolyacid-hydrates a single crystal PFG-NMR and conductivity study. *Solid State Ionics*, 28-30(583):589–593, 1988.
- [70] A. Orera and P. R. Slater. New Chemical Systems for Solid Oxide Fuel Cells. *Chemistry of Materials*, 22(3):675–690, 2010.
- [71] J. Wu, R. A. Davies, M. S. Islam, and S. M. Haile. Atomistic Study of Doped BaCeO_3 : Dopant Site-Selectivity and Cation Nonstoichiometry. *Chemistry of Materials*, 17(4):846–851, 2005.
- [72] A.-C. Dupuis. Proton exchange membranes for fuel cells operated at medium temperatures: Materials and experimental techniques. *Progress in Materials Science*, 56(3):289–327, 2011.

- [73] D. A. Boysen. High-Performance Solid Acid Fuel Cells Through Humidity Stabilization. *Science*, 303(5654):68–70, 2004.
- [74] P. Ramaswamy, N. E. Wong, and G. K. H. Shimizu. MOFs as proton conductors – challenges and opportunities. *Chem. Soc. Rev.*, 43(16):5913–5932, 2014.
- [75] J. L. Segura, M. J. Mancheño, and F. Zamora. Covalent organic frameworks based on Schiff-base chemistry: synthesis, properties and potential applications. *Chemical Society Reviews*, 45(20):5635–5671, 2016.
- [76] G. Alberti and M. Casciola. Solid state protonic conductors, present main applications and future prospects. *Solid State Ionics*, 145(1-4):3–16, 2001.
- [77] P. N. Oliveira, M. Catarino, C. M. O. Müller, L. Brandão, D. A. Pacheco Tanaka, J. R. Bertolino, A. M. Mendes, and A. T. N. Pires. Preparation and characterization of crosslinked PVAL membranes loaded with boehmite nanoparticles for fuel cell applications. *Journal of Applied Polymer Science*, 131(8):40148–40159, 2014.
- [78] R. L. Frost, Y. Xi, R. Scholz, F. M. Belotti, and L. E. Lagooniro. Chemistry, Raman and infrared spectroscopic characterization of the phosphate mineral reddingite: $(\text{MnFe})_3(\text{PO}_4)_2(\text{H}_2\text{O},\text{OH})_3$, a mineral found in lithium-bearing pegmatite. *Physics and Chemistry of Minerals*, 39(10):803–810, 2012.
- [79] R. L. Frost, Y. Xi, R. Scholz, A. López, R. M. F. Lima, and C. M. Ferreira. Vibrational spectroscopic characterization of the phosphate mineral series eosphorite–childrenite– $(\text{Mn},\text{Fe})\text{Al}(\text{PO}_4)(\text{OH})_2\cdot(\text{H}_2\text{O})$. *Vibrational Spectroscopy*, 67:14–21, 2013.
- [80] T. Köhler. Proton Dynamics in the Eosphorite-Childrenite Series. Master thesis, Ludwig-Maximilians-Universität München, 2017.
- [81] A. R. West. Crystalline solid electrolytes I: General considerations and the major materials. In Peter G. Bruce, editor, *Solid state electrochemistry*, pages 7–42. Cambridge University Press, Cambridge, 1995.
- [82] J. Maier. Solid State Electrochemistry I: Thermodynamics and Kinetics of Charge Carriers in Solids. In B. E. Conway, C. G. Vayenas, R. E. White, and M. E. Gamboa-Adelco, editors, *Modern Aspects of Electrochemistry*, volume 38, pages 1–173. Springer, Boston, MA, Boston, MA, 2005.
- [83] M. Avdeev, V. B. Nalbandyan, and I. L. Shukaev. Alkali Metal Cation and Proton Conductors: Relationships between Composition, Crystal Structure, and Properties. In Vladislav V. Kharton, editor, *Handbook of Solid State Electrochemistry - Volume 1*, chapter 7, pages 227–278. Wiley-VCH Verlag GmbH & Co. KGaA, Weinheim, 2009.
- [84] A. V. Chadwick and S. L. P. Savin. Ion-Conducting Nanocrystals: Theory, Methods, and Applications. In *Solid State Electrochemistry I*, pages 79–132. Wiley-VCH Verlag GmbH & Co. KGaA, Weinheim, Germany, 2009.
- [85] J. Maier. *Physical Chemistry of ionic materials: Ions and Electrons in Solids*. John Wiley & Sons, Ltd., Chichester, 2004.
- [86] J. B. Goodenough. Crystalline solid electrolytes II: Material design. In Peter G. Bruce, editor, *Solid state electrochemistry*, pages 43–73. Cambridge University Press, Cambridge, 1995.
- [87] J. Maier and W. Münch. Thermal Destiny of an Ionic Crystal. *Zeitschrift für anorganische und allgemeine Chemie*, 626(1):264–269, 2000.
- [88] J. Maier. Fundamentals, Applications, and Perspectives of Solid-State Electrochemistry: A Synopsis. In Vladislav V. Kharton, editor, *Handbook of Solid State Electrochemistry - Volume 1*, chapter 1, pages 1–14. Wiley-VCH Verlag GmbH & Co. KGaA, 2009.
- [89] P. Knauth and H. L. Tuller. Solid-State Ionics: Roots, Status, and Future Prospects. *Journal of the American Ceramic Society*, 85(7):1654–1681, 2002.

- [90] R. S. Rowland and R. Taylor. Intermolecular Nonbonded Contact Distances in Organic Crystal Structures: Comparison with Distances Expected from van der Waals Radii. *The Journal of Physical Chemistry*, 100(18):7384–7391, 1996.
- [91] K. Morokuma. Why do molecules interact? The origin of electron donor-acceptor complexes, hydrogen bonding and proton affinity. *Accounts of Chemical Research*, 10(8):294–300, 1977.
- [92] G. A. Jeffrey. *An Introduction to Hydrogen Bonding*. Oxford University Press, New York, 1997.
- [93] H. Ishikita and K. Saito. Proton transfer reactions and hydrogen-bond networks in protein environments. *Journal of The Royal Society Interface*, 11(91):20130518–20130518, 2013.
- [94] G. A. Samara. Vanishing of the Ferroelectric and Antiferroelectric States in KH_2PO_4 -Type Crystals at High Pressure. *Physical Review Letters*, 27(2):103–106, 1971.
- [95] G. A. Samara. Pressure dependence of the static and dynamic properties of KH_2PO_4 and related ferroelectric and antiferroelectric crystals. *Ferroelectrics*, 71(1):161–182, 1987.
- [96] P. S. Peercy and G. A. Samara. Pressure and Temperature Dependences of the Dielectric Properties and Raman Spectra of RbH_2PO_4 . *Physical Review B*, 8(5):2033–2048, 1973.
- [97] K. C. Kao. Electric Polarization and Relaxation. In *Dielectric Phenomena in Solids*, pages 41–114. Elsevier, San-Diego, 2004.
- [98] E. C. C. de Souza and R. Muccillo. Properties and applications of perovskite proton conductors. *Materials Research*, 13(3):385–394, 2010.
- [99] M. Saiful Islam. Ionic transport in ABO_3 perovskite oxides: a computer modelling tour. *Journal of Materials Chemistry*, 10(4):1027–1038, 2000.
- [100] M. Ivanova, S. Ricote, S. Baumann, W. A. Meulenber, F. Tietz, J. Serra, and H. Richter. Ceramic materials for energy and environmental applications: Functionalizing of properties by tailored compositions. In L. Yu, editor, *Doping: Properties, Mechanisms and Applications*, pages 221–276. Nova Science Publishers, Inc., 2013.
- [101] K. D. Kreuer. On the complexity of proton conduction phenomena. *Solid State Ionics*, 136-137(1-2):149–160, 2000.
- [102] K. D. Kreuer. Proton Conductivity: Materials and Applications. *Chemistry of Materials*, 8(3):610–641, 1996.
- [103] W. Münch, G. Seifert, K. D. Kreuer, and J. Maier. A quantum molecular dynamics study of the cubic phase of BaTiO_3 and BaZrO_3 . *Solid State Ionics*, 97(1-4):39–44, 1997.
- [104] W. Münch, K. D. Kreuer, Adams, G. Seifert, and J. Maier. The relation between crystal structure and the formation and mobility of protonic charge carriers in perovskite-type oxides: A case study of Y-doped BaCeO_3 and SrCeO_3 . *Phase Transitions*, 68(3):567–586, 1999.
- [105] B. C. Wood and N. Marzari. Proton dynamics in superprotonic CsHSO_4 . *Physical Review B*, 76(13):134301, 2007.
- [106] B. Merinov. Mechanism of proton transport in compounds having a dynamically disordered hydrogen bond network. *Solid State Ionics*, 84(1-2):89–96, 1996.
- [107] M. Finazzi, L. Duò, and F. Ciccacci. Low-Dimensional Antiferromagnetic Oxides: An Overview. In *Magnetic Properties of Antiferromagnetic Oxide Materials*, pages 1–23. Wiley-VCH Verlag GmbH & Co. KGaA, Weinheim, Germany, 2010.
- [108] M. Opel. Spintronic oxides grown by laser-MBE. *Journal of Physics D: Applied Physics*, 45(3):033001, 2012.
- [109] J. M. D. Coey. *Magnetism and Magnetic Materials*. Cambridge University Press, Cambridge, 2010.
- [110] J. Kanamori. Superexchange interaction and symmetry properties of electron orbitals. *Journal of Physics and Chemistry of Solids*, 10(2-3):87–98, 1959.

BIBLIOGRAPHY

- [111] J. B. Goodenough. Theory of the Role of Covalence in the Perovskite-Type Manganites [La,M(II)]MnO₃. *Physical Review*, 100(2):564–573, 1955.
- [112] P. W. Anderson. Antiferromagnetism. Theory of Superexchange Interaction. *Physical Review*, 79(2):350–356, 1950.
- [113] J. B. Goodenough. *Magnetism and the chemical bond*. John Wiley & Sons, Inc., New York/London, 1963.
- [114] R. M. Cornell and U. Schwertmann. *The Iron Oxides: Structure, Properties, Reactions, Occurrences and Uses*. Wiley-VCH, Weinheim, Germany, 2003.
- [115] P. W. Anderson and H. Hasegawa. Considerations on Double Exchange. *Physical Review*, 100(2):675–681, 1955.
- [116] R. E. Newnham. *Properties of materials*. Oxford University Press, New York, 2005.
- [117] M. Reis. *Fundamentals of magnetism*. Elsevier Ltd., Oxford, 1 edition, 2013.
- [118] D. B. Litvin. *Magnetic Group Tables*. International Union of Crystallography, Chester, England, 2013.
- [119] V. Petríček, M. Dušek, and L. Palatinus. Crystallographic Computing System JANA2006: General features. *Zeitschrift für Kristallographie - Crystalline Materials*, 229(5), 2014.
- [120] V. F. Lvovich. *Impedance Spectroscopy*. John Wiley & Sons, Inc., Hoboken, NJ, USA, 2012.
- [121] U. Simon and M.E. Franke. Electrical properties of nanoscaled host/guest compounds. *Micro-porous and Mesoporous Materials*, 41(1-3):1–36, 2000.
- [122] S. Nasu. General Introduction to Mössbauer Spectroscopy. In Yutaka Yoshida and Guido Langouche, editors, *Mössbauer Spectroscopy*, pages 1–22. Springer, Berlin, Heidelberg, 2013.
- [123] G. Oszlányi and A. Sütő. Ab initio structure solution by charge flipping. *Acta Crystallographica Section A Foundations of Crystallography*, 60(2):134–141, 2004.
- [124] Milanesio M. and D. Viterbo. Solution and refinement of crystal structures. In C. Giacovazzo, editor, *Fundamentals of Crystallography*, chapter 6, pages 417–511. Oxford University Press, Oxford, 3 edition, 2011.
- [125] C. Giacovazzo. Solution and refinement of crystal structures. In C. Giacovazzo, editor, *Fundamentals of Crystallography*, chapter 2, pages 66–156. Oxford University Press, Oxford, 3 edition, 2011.
- [126] H. L. Monaco and G. Artioli. Experimental methods in X-ray and neutron crystallography. In C. Giacovazzo, editor, *Fundamentals of Crystallography*, chapter 5, pages 301–416. Oxford University Press, Oxford, 3 edition, 2011.
- [127] J. Rodríguez-Carvajal. FullProf Suite, 2011.
- [128] T. Armbruster and R. Oberhänsli. Crystal chemistry of double-ring silicates: Structures of Sugilite and Brannockite. *American Mineralogist*, 73:595–600, 1988.
- [129] M.A.; Hawthorne Cooper F.C.; Grew, E.S. The crystal chemistry of sogdianite, a milarite-group mineral. *American Mineralogist*, 84:764–768, 1999.
- [130] F. C. Hawthorne, M. Kimata, P. Cerny, N. A. Ball, G. R. Rossman, and J. D. Grice. Crystal chemistry of the milarite-group minerals. *American Mineralogist*, 76:1836–1856, 1991.
- [131] T. Armbruster, V. Bermanec, M. Wenger, and R. Oberhänsli. Crystal structure of double-ring silicates: structure of natural and dehydrated milarite at 100 K. *European Journal of Mineralogy*, 1:353–362, 1989.
- [132] P. Cerny, F. C. Hawthorne, and E. Jarosewich. Crystal chemistry of milarite. *The Canadian Mineralogist*, 18(1):41, 1980.
- [133] I. D. Brown and R. D. Shannon. Empirical bond-strength–bond-length curves for oxides. *Acta Crystallographica Section A*, 29(3):266–282, 1973.

BIBLIOGRAPHY

- [134] K. Kohno, T. Matsuo, and M. Ichikawa. Tunneling Effect in Phase Transitions of $\text{K}_3\text{H}(\text{SeO}_4)_2$ and Its Deuterated Analogue. *Journal of the Korean Physical Society*, 32:393–396, 1998.
- [135] M. Endo, T. Kaneko, T. Osaka, and Y. Makita. Dielectric Study of the Phase Transition in $\text{K}_3\text{H}(\text{SeO}_4)_2$ and Isotope effect. *Journal of the Physics Society Japan*, 52(11):3829–3832, 1983.
- [136] Y. Moritomo, Y. Tokura, N. Nagaosa, T Suzuki, and K. Kumagai. Role of the proton tunneling in the phase transition of $\text{K}_3\text{D}_{1-x}\text{H}_x(\text{SO}_4)_2$. *Journal of Low Temperature Physics*, 99(1-2):55–70, 1995.
- [137] D. Merunka and B. Rakvin. Mechanism of quantum effects in hydrogen-bonded crystals of the $\text{K}_3\text{H}(\text{SO}_4)_2$ group. *Physical Review B*, 79(13):132108, 2009.
- [138] F. Fillaux and A. Cousson. Neutron scattering studies of $\text{K}_3\text{H}(\text{SO}_4)_2$ and $\text{K}_3\text{D}(\text{SO}_4)_2$: The particle-in-a-box model for the quantum phase transition. *The Journal of Chemical Physics*, 137(7):074504, 2012.
- [139] J. B. Goodenough. Direct Cation-Cation Interactions in Several Oxides. *Physical Review*, 117(6):1442–1451, 1960.
- [140] K. Motida and S. Miyahara. On the 90° exchange Interaction between cations (Cr^{3+} , Mn^{2+} , Fe^{3+} and Ni^{2+}) in oxides. *Journal of the physical society of Japan*, 28(5):1188–1196, 1970.

Part V.
Appendix

12. Publication on sugilite

Journal of Solid State Chemistry 264 (2018) 98–107



Contents lists available at ScienceDirect

Journal of Solid State Chemistry

journal homepage: www.elsevier.com/locate/jssc



Na⁺/Li⁺-ionic conductivity in Fe₂Na₂K[Li₃Si₁₂O₃₀]



B. Röska^a, I. Akter^a, M. Hoelzel^b, S.-H. Park^{a,*}

^a Department of Geo- and Environmental Sciences, Section of Crystallography, Ludwig-Maximilians-Universität München (LMU), Munich, Germany

^b Heinz Maier-Leibnitz Zentrum (MLZ), Technische Universität München (TUM), Garching, Germany

ARTICLE INFO

Keywords:

Combined ionic conductivity
Neutron powder diffraction
Hydrothermal synthesis
Impedance spectroscopy
Sugilite

ABSTRACT

A sugilite-type double 6-membered ring (D6MR) silicate, Fe₂Na₂K[Li₃Si₁₂O₃₀] could be obtained for the first time under mild hydrothermal conditions. Impedance spectra revealed a bulk conductivity of $1.2 \times 10^{-5} \text{ S cm}^{-1}$ at 923 K. Hopping pathways of Li⁺ and Na⁺ were indicated in difference Fourier (ΔF) maps parallel to the D6MRs network using neutron powder diffraction at 298–1123 K. The current study presents a promising prototype for combined 2-dimensional Li⁺/Na⁺-ionic conductors with crystal-chemical flexibility and thermally high stability.

1. Introduction

In exploring prototype structures for direction-dependent design and engineering of all-solid-state electrochemical cells, our attention was taken to the so-called sogdianite-sugilite series as promising stable high-temperature ionic conductors [1]. This consideration is based on the interesting structural property of this solid solution: the 3-dimensional (3D) topology stable up to about 1300 K with 2-dimensional (2D) anisotropic properties in the hexagonal metric ($a \approx 10 \text{ \AA}$ and $c \approx 14 \text{ \AA}$; $P6/mcc$). This geometrical flexible 3D structure type belongs to the milarite group showing an extremely wide range of chemical compositions, which is comparable to those of spinels and perovskites. Its high compositional diversity, as given in Table 1, is represented by the general formula for the milarite family $^{[6]}A_2^{[9]}B_2^{[12]}C^{[18]}D^{[4]}T_2^{[4]}T_{12}O_{30}$ [1–8]. Characteristically, D6MRs of $[TIO_4]$ tetrahedra form channels running along the *c*-axis (Fig. 1). Perpendicular to this, the layers of alternating, highly distorted $[T_2O_4]$ tetrahedra and $[AO_6]$ octahedra build up a rugged framework with a high degree of crystal-chemical flexibility (Fig. 1b) [9]. In between two such network layers, the nine-fold coordinated *B* site is bounded in by two $[AO_6]$ octahedra. The twelve-fold coordinated *C* site is found at the axis of the channels, wedged in between two D6MRs. Centred within the D6MRs, the eighteen-fold coordinated *D* site is mostly unoccupied [9]. In this sense, the milarite-type topology can be regarded as a pseudo-porous framework with 6MR-openings which are too small for reversible hydration-dehydration process, hence stable against moisture. A low sensitivity to thermal variation and hydration but with a high chemical flexibility for solid solution formation is one of the most relevant prerequisites in development of economically-ecologically friendly electrochemical materials.

For this purpose, the current study presents synthesis and characterisation of the synthetic counterpart of the mineral sugilite rarely occurring. Typically, natural sugilite samples from a few known deposits [2,10,11] are described by the generic formula $(Fe^{3+}, Al, Mn^{3+})_2Na_2K[Li_3Si_{12}O_{30}]$ [4]. The Zr-rich counter part sogdianite ($Zr, Ti, Fe^{3+}, Al)_2(Na, \square)_2K[Li_3Si_{12}O_{30}]$ [11] possesses considerably less Na for the presence of quadrivalent cations at the *A* site. In spite of the same amount of Li per formula unit (*pfu*) in sugilite and sogdianite, the former shows a much higher ionic conductivity mainly due to the high amount of mobile Na⁺. Hence, sugilite is considered as an interesting combined Li⁺/Na⁺-ion conductor. An extensive study of Li⁺/Na⁺ dynamics in the mineral sugilite will be reported elsewhere. We focus here on the investigation of sugilite analogue, $Fe_2^{3+}Na_2K[Li_3Si_{12}O_{30}]$ synthesized under mild hydrothermal conditions. The synthetic products were subject to variable-temperature impedance spectroscopy and high-resolution neutron powder diffraction (HRNPD). Subtle structure analysis and subsequent inspection of difference Fourier (ΔF) maps resolved the dynamic disorder of Li and Na. Their 2D hopping paths are strongly anisotropic perpendicular to $[001]$ direction.

2. Experimental

2.1. Hydrothermal synthesis

Hydrothermal syntheses were performed with varying starting compositions in alkali environment to enhance the solubility of $\alpha\text{-Fe}_2O_3$ and SiO_2 in the starting suspension. As given in Table 2, a series of synthesis mixtures were prepared with different ratios of

* Corresponding author.

E-mail address: sohyun.park@lmu.de (S.-H. Park).

<https://doi.org/10.1016/j.jssc.2018.05.008>

Received 16 April 2018; Received in revised form 4 May 2018; Accepted 7 May 2018
0022-4596/© 2018 Elsevier Inc. All rights reserved.

Table 1
Possible cation occupation at the respective sites in milarite-type structure, revealing the broad crystal-chemical flexibility (\square =vacancy) [1,4,12].

Sites	Multiplicity	Coordination	Element
T1	24	4	Si, Al
T2	6	4	Li, Be, B, Mg, Al, Si, Mn ²⁺ , Zn
A	4	6	Al, Fe ³⁺ , Sn ⁴⁺ , Mg, Zr, Fe ²⁺ , Ca, Na, Y, Sc, Mn ³⁺ , Ti ⁴⁺
B	4	9	Na, H ₂ O, \square , K
C	2	12	K, Na, Ba, \square
D	2	18	\square

reaction educts, i.e. NaOH (99%, Riedel-de Haen AG), LiOH·H₂O (56.6%, Alfa Aesar), KOH (85%, Merck), Fe₂O₃ (Merck), SiO₂ colloidal dispersion (40 wt% in H₂O, Alfa Aesar). These were added step-by-step to deionized H₂O while vigorously stirring. The starting gel was aged further for 4 h at room temperature (RT) and brought to the reaction under hydrothermal conditions in Teflon-lined steel autoclaves at 500–540 K for 5–14 days. The synthesis products were washed with deionized water and dried overnight at RT.

2.2. X-ray powder diffraction (XPD)

For phase identification of synthetic product XPD data were collected on a powder diffractometer (STOE STADI P) using Mo K α_1 radiation (Ge(111) monochromator) in Debye-Scherrer transmission geometry. XPD data was collected in a wide 2θ range of 2–75° on a linear position-sensitive detector (PSD) with a step with of 0.02° (2θ). For the use in Rietveld analysis several XPD data sets were added up to improve counting statistics. Rietveld calculations were performed with the software package FullProf Suite [13].

2.3. High resolution neutron powder diffraction (HRNPD)

HRNPD was conducted at the instrument SPODI [14] at the neutron facility FRM2, Garching near Munich, Germany. Using a wavelength of 1.463 Å (Ge(551) monochromator) a set of HRNPD data was collected on 80 vertically aligned PSDs with 300 mm high collimators. A powder sample (about 1 g) was packed into a Nb can and positioned within a Nb high-temperature (HT) furnace under vacuum. Data acquisition was made at 298 K, 573 K, 723 K, 923 K, and 1123 K, subsequently. A 2θ range of 1–160° in steps of 0.05° was recorded several times at each measuring temperature and summed up to increase the signal/noise ratio. With results from structure refinements with HRNPD data sets, ΔF maps, and bond valence sums (BVS) were evaluated using FullProf Suite [13]. BVS values with estimated standard deviations are derived from individual bonding distances of the refined structure model [15].

2.4. Impedance spectroscopy (IS)

A disc of 2 mm thickness and a radius of 2 mm ($A = 12.56 \text{ mm}^2$) was pressed with the selected sample. The flattened disc surface area

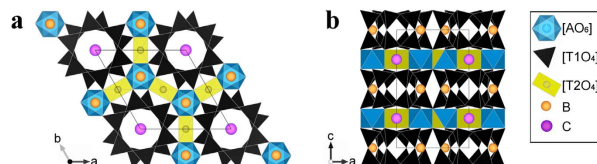


Fig. 1. Tetrahedral-octahedral framework topology of milarite-type compounds, plotted in [001] (a) and in [210] (b), where A=Fe³⁺, B=Na, C=K, T1=Si, and T2=Li in Fe₂Na₂K[Li₃Si₁₂O₃₀].

Table 2
Molar ratios of the educts in reaction gels and quantitative phase analysis using multipattern Rietveld analyses with XPD data of selected syntheses products (S: Fe₂Na₂K[Li₃Si₁₂O₃₀]; Qz: α -quartz; H: α -Fe₂O₃).

Molar ratios of educts Na: Fe: K: Li: Si: H ₂ O	Syntheses Products S: Qz: H [wt %]
1: 2: 1: 3: 12: 1000	93.1(5); 6.8(1); 0.0(1)
1: 2: 1: 3: 10: 1000	92(3); 5.4(3); 3.0(3)
1: 2: 1: 3: 10: 500	63.0(3); 29(1); 8.0(5)
1: 2: 1: 3: 7: 1000	86(1); 13.6(2); 0.1(1)
1: 1.5: 1: 3: 7: 1000	90(1); 8.6(2); 1.3(1)
1: 1.2: 1: 3: 7: 1000	88(2); 11.5(5); 0.0(0)
1: 1: 1: 3: 7: 1000	94.6(5); 0.0(0); 5.4(1)
1: 0.9: 1: 3: 7: 1000	92.1(3); 0.0(0); 7.9(2)
1: 0.8: 1: 3: 7: 1000	91.3(6); 0.5(1); 8.2(1)

was covered with Pt paste and tempered at 473 K to remove organic glue. The disc was locked between two Pt electrodes and brought into a home-constructed HT probe to acquire complex impedance spectra using a Hewlett Packard 4284A LCR meter. A NiCr-Ni thermocouple located immediately next to the sample (0.3 mm) was connected to a temperature controller maintaining a constant sample temperature with the accuracy of ± 1 K. For data evaluation with less grain boundary effect, we used the IS spectra recorded at cooling from 963 K down to RT in steps of 30 K in the frequency interval of 20 Hz to 1 MHz. We want to stress that the sample contained the minor phase α -Fe₂O₃ (5.3(1) wt%), but the intrinsic electron conductivity of α -Fe₂O₃ is out of the energy window probed [16,17].

3. Results and discussion

3.1. Syntheses products and phase analysis

As-synthesized products in a form of disc consisted of reddish fine crystallites rimmed with some coarse white agglomerates. According to XPD patterns, these white aggregates comprised crystalline Li₂Si₂O₅ and SiO₂ (α -quartz type), but they could easily be detached from the main phase segregation. Multi pattern Rietveld refinements with XPD data of the main product part (Fig. 2) agreed with the sugilite-type phase given in Ref. [4], i.e. Fe₂Na₂K[Li₃Si₁₂O₃₀].

In general, the content of quartz was suppressed by lowering the amount of Si in the starting gel. A tiny decrease of Fe₂O₃ in the reaction gel dramatically suppressed the formation of sugilite-type phase. Slight increments of NaOH, LiOH, or KOH concentrations, the HT aging of the starting suspension (320 K Ref. [18]), or the extension of aging period longer than 24 h at RT lead to the formation of Li₂Si₂O₅ as the main product. A short ageing time of 1 h gave rise to mixtures of undesired phases, such as Li₆Si₂O₇, Na₂FeO₄, KFeSi₃O₉ and Li₂Si₂O₅. Higher synthesis temperatures of 510–540 K favoured the formation of α -Fe₂O₃. The highest portion of sugilite-type phase was obtained from the starting mixture with the molar ratios Na:K:Fe:Li:Si:H₂O = 1:1:1:3:7:1000 in excess of Si, Li, K with respect to the ideal Fe-rich sugilite end-member composition (Table 2).

No single crystals of Fe₂Na₂K[Li₃Si₁₂O₃₀] large enough for single

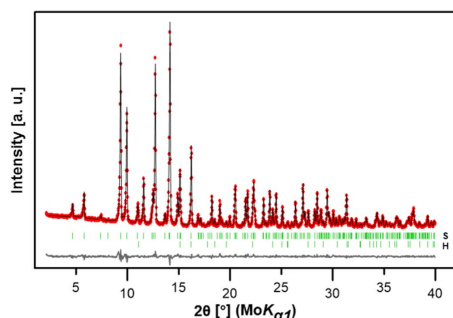


Fig. 2. Graphical representation of the Rietveld refinement with XPD data confirms the successful synthesis of the Fe-rich synthetic counterpart of sugilite, showing a high phase portion of S: H = 0.95: 0.05. (S = $\text{Fe}_2\text{Na}_2\text{K}[\text{Li}_3\text{Si}_{12}\text{O}_{30}]$; H = $\alpha\text{-Fe}_2\text{O}_3$).

crystal diffraction and direction-dependent IS spectra could be obtained in this study. Nonetheless, this study found a mild hydrothermal route to yield a high amount of the counterpart phase of rarely occurring sugilite.

3.2. Impedance spectroscopy

Fig. 3 shows Nyquist plots with exemplary IS data evaluated at 813

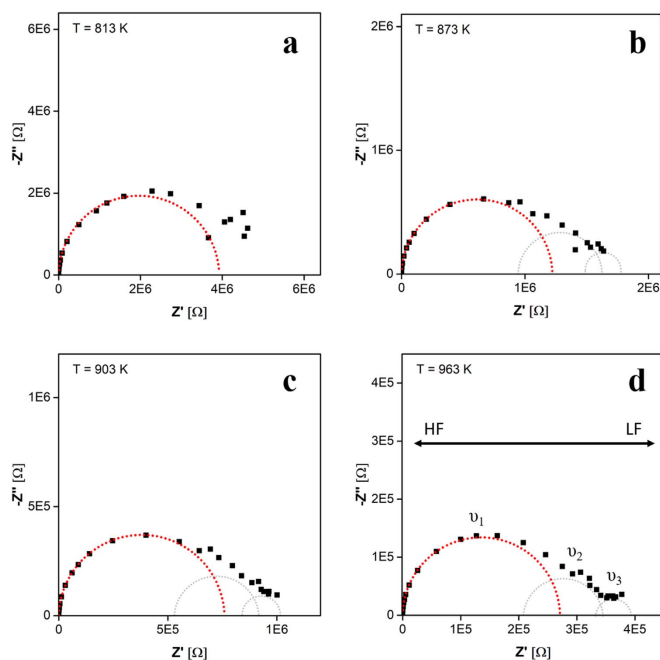


Fig. 3. Complex plane plots of IS spectra of the title compound in the range of 2 Hz - 10^6 Hz at 813 K (a), 873 K (b), 903 K (c), 963 K (d) with fitted high frequency semicircles of critical frequency ν_1 (red). Further relaxations (ν_2, ν_3) are adumbrated by grey semicircles.

K, 873 K, 903 K, and 963 K (further IS spectra are supplied in Suppl. 1). The high frequency (HF) relaxation mode was featured as a semicircle above 720 K and could be fitted well. In contrary, the low frequency (LF) semicircles were severely overlapped and recognized ambiguously. At the lowest frequency range at 963 K, there is no clear increase of Z'' , i.e. a LF spike typical for charge transfer at the sample electrode interface [19]. In contrary, we have observed a clear increase in Z'' at the LF range for compact mass of as-found natural sugilite (Park et al, to be published). Comparing impedance spectra of synthetic and natural sugilite samples, the former shows 100 times higher impedance at same probing temperatures and much higher counting errors. This comparison points to a high influence of grain boundary charge transfer on the bulk conductivity. On the other hand, the presence of further relaxation modes at the lowest frequency range and/or an electronic contribution to the bulk conductivity could not be excluded by the IS spectra probed.

As indicated by diminishing intersection values of the fitted HF semicircles with the real part Z' axis, the sample resistance strongly decreases with increasing temperature. At least three relaxation modes became obvious above 870 K in the imaginary part Z'' plotted vs frequency (f) (Fig. 4). These relaxation frequencies ν_1 , as well as ν_2 , and ν_3 were discernible, matching the critical frequencies of the HF and the esteemed LF semicircles, respectively (Fig. 3). Based on the intersection values of fitted HF semicircles with real Z' -axis in complex plane [20], temperature-dependent bulk DC conductivities ($\sigma_{DC}(T)$) from 963 K down to 723 K were evaluated (Fig. 5a). The obtained σ_{DC} value about $1.2 \times 10^{-5} \text{ S cm}^{-1}$ at 963 K is comparable to the value $4.1 \times 10^{-5} \text{ S cm}^{-1}$ determined with IS spectra of a sodgianite single

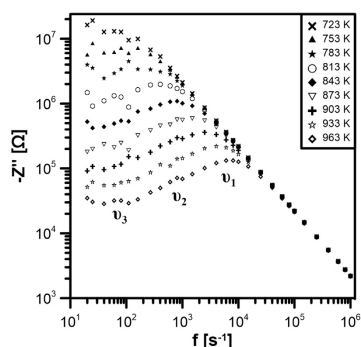


Fig. 4. At least three temperature-dependent relaxation processes with resonance frequencies ν_1 , ν_2 , and ν_3 are visible in Z'' values plotted vs $\log f$. ν_1 and ν_2 are discernible already at 813 K and are shifted to high frequency ranges at elevated temperatures, indicating thermally activated processes, as well.

crystal at 923 K perpendicular to [001] [1].

According to the Arrhenius relation, the linear progression of the $\ln(\sigma T)$ values as a function of the inverse temperature (Fig. 5b) stated the HF mode due to a thermally activated dynamic process with activation energy of 1.22(2) eV. An activation energy of 1.26(3) eV for a sodianite single crystal could be addressed to the HF relaxation due to Li^+ dynamics perpendicular to [001] [1]. A locally limited site-exchanging process requires much lower activation energy than the charge transfer over the lattice, i.e. ionic conductivity about 0.5–1 eV for dehydrated aluminosilicates Li^+/Na^+ conductors [19]. Hence, the activation energy 1.22(2) eV indirectly reflects the dominant contribution of the long-range ionic conductivity in the title compound, beside grain boundary effects. For the same reason, the electronic conductivity can be considered as a less relevant factor.

The evaluated conductivity and activation energy values evaluated from direction-averaged IS spectra of the synthetic sugilite-type compound indicate the presence of charge transport mechanisms common in the sugilite-sodianite series. This is elucidated by results from structure analyses with variable temperature neutron diffraction data sets in the following section.

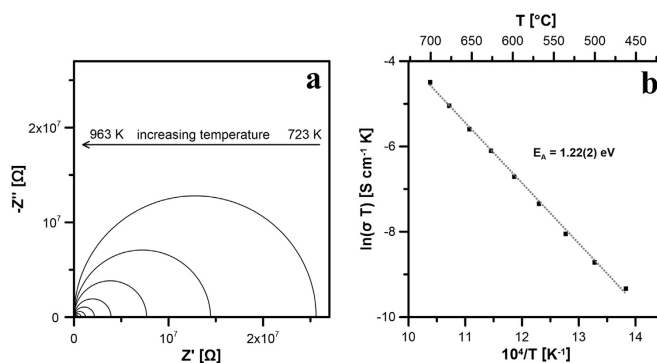


Fig. 5. Calculated HF semicircles of IS spectra between 963 K and 723 K show the decrease of the bulk resistance with increasing temperature (a); Arrhenius plot of the DC conductivity (σ) values evaluated from the fitted HF semicircles. The slope determines an activation energy E_a of 1.22(2) eV in a temperature range of 963–723 K for the bulk conductivity (b).

Table 3
Refined lattice parameters of $\text{Fe}_2\text{Na}_3\text{K}[\text{Li}_3\text{Si}_{12}\text{O}_{30}]$ and agreement factors of Rietveld calculations with HRNPD data sets.

	298 K	573 K	723 K	923 K	1123 K
a [Å]	10.0617(1)	10.0702(2)	10.0764(1)	10.0871(1)	10.0921(2)
c [Å]	14.0832(1)	14.1022(3)	14.1092(2)	14.1216(3)	14.1505(4)
V [Å ³]	1234.73(2)	1238.50(4)	1240.64(3)	1244.39(3)	1248.13(4)
Rp [%]	5.54	10.3	5.69	6.63	9.89
Rwp [%]	5.75	9.38	5.29	6.14	9.19
Rexp [%]	1.51	6.76	2.94	2.85	3.30
χ^2	14.5	1.92	3.23	4.65	7.75
DW	0.2024	0.8276	0.5760	0.4191	0.2933
p	98	148	134	113	130

$R_p = 100(\sum < y_i - y_{c,i} > / \sum y_i)$; $R_{wp} = 100(\sum \omega_i < y_i - y_{c,i} >^2 / \sum \omega_i y_i^2)^{1/2}$; $R_{exp} = 100(n - p) / \sum \omega_i y_i^2$; $\chi^2 = (R_{wp}/R_{exp})^2$; $\omega_i = 1/\sigma_i^2$, where σ_i is the standard deviation of the intensity y_i in the observed profile, $y_{c,i}$ are the calculated counts, n the total number of data points, and p the number of refined parameters. The high χ^2 value of the 298 K data refinement is mainly due to the extremely high counts and the smaller number of refined parameters compared to the other temperature data sets. Durbin-Watson statistics (DW) are an indicator for the amount of serial correlation of parameters [23].

3.3. Structure determination with HRNPD data

HRNPD data sets were acquired with a powder sample made at the very initial stage of investigation, where amounts of impurity phases could not be prevented, such as $\alpha\text{-Fe}_2\text{O}_3$ ($R\bar{3}c$), $\alpha\text{-quartz}$ ($P3_221$), and above 846 K $\beta\text{-quartz}$ ($P6_322$). In addition, the antiferromagnetic (AF) spin order of $\alpha\text{-Fe}_2\text{O}_3$ with the propagation vector $\mathbf{k} = (0,0,0)$ was taken into account using magnetic space group $R\bar{1}$ from the irreducible representation Γ^6 [21]. The intensity of the strongest magnetic reflection 003 ($2\theta \approx 18.2\text{--}18.4^\circ$) is continuously decreasing with increasing temperature but is still discernible in the pattern at 1123 K. Above its Néel temperature $T_N \approx 955$ K [22], there was weak intensity of the reflection 003 up to 1123 K possibly due to AF domains retaining. Besides, the Nb sample holder showed an anomalous microstructure, which could not be refined properly by Rietveld calculation and was treated by LeBail-fitting.

All lattice parameters and agreement factors of structure analyses with HRNPD data sets obtained at 298 K, 573 K, 723 K, 923 K, and 1123 K are listed in Table 3. The quantitative analysis gave rise to 91(1) wt% synthetic sugilite-type compound, 6.0(2) wt% quartz, and 3.0(4) wt% $\alpha\text{-Fe}_2\text{O}_3$. The synthetic sugilite is stable up to 1123 K, where the presence of weak peaks in the low 2θ -range indicate

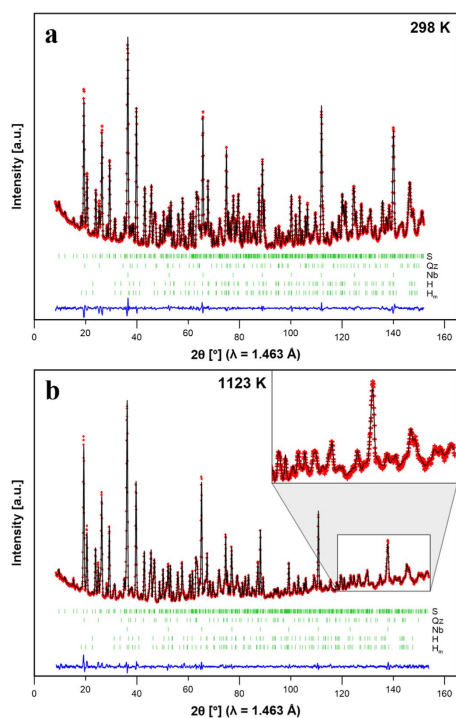


Fig. 6. Graphic presentation of Rietveld analysis with observed (+) and calculated (black line) HRNPD pattern at 298 K (a) and 1123 K (b). Short bars indicate the positions of reflections belonging to the respective phases: S = $\text{Fe}_2\text{Na}_2\text{KLi}_3\text{Si}_{12}\text{O}_{30}$, Qz = quartz, Nb = Niobium (sample can), H = $\alpha\text{-Fe}_2\text{O}_3$, H_m = magn. phase of $\alpha\text{-Fe}_2\text{O}_3$. The difference profile between observed and calculated intensities is plotted at the bottom.

recrystallisation processes starting around 1123 K. Rietveld refinements with HRNPD data acquired at 298 K and 1123 K are graphically demonstrated in Fig. 6 (573 K, 723 K and 923 K refinements provided in Suppl. 2), showing good agreements between observed and calculated patterns.

A volume expansion coefficient of $1.15 \times 10^{-5} \text{ K}^{-1}$ was determined from 298 K to 1123 K. The unit cell expands direction-dependently by 0.48% and 0.30% in [001] and [100], respectively (Table 3). This anisotropy is attributed to the 2D network of rigid D6MRs which are further fastened by $[\text{LiO}_4]\text{-}[\text{FeO}_6]$ chains in the (a-b) plane. Based on results from structure analyses, the title compound has the ideal formula of the Fe-rich end-member, $\text{Fe}_2\text{Na}_2\text{K}[\text{Li}_3\text{Si}_{12}\text{O}_{30}]$. Atomic positions of all phases except for Nb were refined initially with soft bond constraints which were released in subsequent refinement cycles (Table 4). Atomic displacement parameters (ADPs) were refined anisotropic whenever reasonable without high correlations. For instances, the atomic z-coordinate of Na at the B-site and its anisotropic ADPs were heavily correlated. The z-coordinates of Na refined with isotropic ADP were in accordance to those previously established [4,5,9,24,25] and hence fixed thereupon to refine anisotropic ADPs.

The pronounced motion of Na with rising temperatures was indicated when evaluating ΔF maps with zero occupancy (OCC) at B

site (Fig. 7). At low temperatures below 400 K Na behaves statically disordered at its split sites along the c-axis. However, the dynamic disorder of Na became dominant at higher temperatures not only in the c-direction, but also in the (a-b) plane, as indicated by the regression lines of ADPs towards 0 K (Fig. 8). More interestingly, the ADPs of Na could not be described by harmonic terms above RT, as showing triangle-like residual diffuse neutron scattering length (nsf) density around the B site in the (a-b) plane (Fig. 7). Furthermore, depletion of Na at B is reflected by $U^{33}(\text{Na})$ at 1123 K which is one magnitude larger than $U^{33}(\text{Na})$ at 923 K. For Li, it was not possible to refine anisotropic ADPs below 723 K. The Li dynamic disorder is however obvious in ΔF maps, as described in the next section in detail.

In general, the title compound as-synthesized has larger lattice parameters compared to the mineral sugilite which features partial substitutions of Fe^{3+} by Al^{3+} and Mn^{3+} with smaller bonding lengths to oxygens [26]. In this study, typical Fe^{3+} -O bonding distances are observed for the A site (Table 5). The sites B, C, T1, and T2 display characteristic bonding lengths between oxygens and the respective atoms Na, K, Si, and Li. The final structure model is further supported by proper BVS, exemplarily given for the structure model at 298 K in Table 5. Exceptionally, the BVS value 0.858(2) at B sites is less than the charge of the occupier, i.e. Na^+ . This observation is relevant in terms of Na migration in the (a-b) plane, promoted by strong local motion at B. Its depletion is confirmed indirectly by the high BVS 4.14(1) of Si for the extremely short bonding distance of Si to O3 where the charge of oxygen at O3 is not completely compensated by Na^+ . Details of Na dynamic disorder is dealt with ΔF maps further in the following section.

3.4. Mechanisms of ionic conduction

ΔF maps of HRNPD refinements were carefully investigated for residuals of nsf densities in order to find interstitial sites for Li (Coh b (Li) = -1.90 fm) and Na (Coh b (Na) = 3.63 fm). As shown in Fig. 9, negative residuals are clearly resolved in tetrahedral voids at $\frac{1}{2}, \frac{1}{3}, \frac{1}{6}$ providing optimal bonding distances [26] (average = 1.981 Å) and BVS ($\Sigma \approx 1.03$) for Li (Table 6). We assigned these residuals to the interstitial site L_i' over which Li atoms can hop from one to another T2 site. This mechanism over interstitial sites L_i' is realized by the relatively short hopping route $d(\text{T2-L}_i') \approx 3.05 \text{ \AA}$ [27,28], giving rise to a 2D network for conducting Li^+ . Furthermore, Li^+ hopping within the (a-b) plane is indicated by the strongly anisotropic ADPs of Li at T2 with $U^{11} = U^{22} > U^{33}$ at 1123 K, as visualised by main elongations of the corresponding thermal displacement ellipsoids in Fig. 10a. The O3-O3 edge of the $[\text{T2O}_4]$ tetrahedron can be considered as the bottleneck in this suggested hopping path. The increasing ionic-conductivity upon heating the compound can be explained by thermal effects on this structural constriction: i) the distance $d(\text{O3-O3})$ becomes significantly elongated from RT (3.646 Å) to 1123 K (3.706 Å); ii) the anisotropic thermal motions at O3 sites pronounced perpendicular to the Li passageway widen the bottleneck temporarily. Thus, a 2D long range charge transfer of Li^+ is suggested running in circular paths in the $[\text{LiO}_4]\text{-}[\text{FeO}_6]$ plane (Fig. 10).

In search of positive residuals of nsf densities an additional site at $\frac{1}{2}, \frac{1}{3}, 0$ was detected in ΔF maps at 1123 K. This site is located in a highly distorted octahedral cavity in the exact middle between two B sites in the (a-b) plane (Fig. 11b). We assigned this new site to an interstitial site Na' which is situated only at a distance of $\approx 2.91 \text{ \AA}$ from B (Fig. 12a). Coordinated by four O3 and two O1 sites, the average bonding length of 2.648(3) Å to oxygens and BVS of ≈ 1.02 are suitable for Na (Table 6). The temporary residence of Na at Na' explains the unsaturated BVS at the B site, as aforementioned. Interestingly, continuous positive residuals in ΔF maps at $z = 0.08$ trace the diffusion pathway $B \leftrightarrow \text{Na}' \leftrightarrow B$ (Fig. 11b). The offset of the hopping pathway from the z-coordinate of the B site is reflected by the strong anisotropic thermal site motion of Na at B ||

12. Publication on sugilite

B. Röska et al.

Journal of Solid State Chemistry 264 (2018) 98–107

Table 4
Refined atomic parameters for Fe₂Na₂K[Li₃Si₁₂O₃₀] between 298 K and 1123 K.

Atom	Parameter	298 K	573 K	723 K	923 K	1123 K
Fe	x	1/3	1/3	1/3	1/3	1/3
	y	2/3	2/3	2/3	2/3	2/3
	z	1/4	1/4	1/4	1/4	1/4
	B _{iso}	0.15(1)				
	U ¹¹		0.006(1)	0.008(1)	0.012(1)	0.015(2)
	U ²²		0.006(1)	0.008(1)	0.012(1)	0.015(2)
Na	x	1/3	1/3	1/3	1/3	1/3
	y	2/3	2/3	2/3	2/3	2/3
	z	0.0162	0.0199	0.0146	0.0213	0.0279
	B _{iso}					4.7(4)
	U ¹¹	0.008(2)	0.018(5)	0.042(4)	0.046(5)	
	U ²²	0.008(2)	0.018(5)	0.042(4)	0.046(5)	
K	x	0	0	0	0	0
	y	0	0	0	0	0
	z	1/4	1/4	1/4	1/4	1/4
	B _{iso}					
	U ¹¹	0.007(3)	0.019(7)	0.038(5)	0.047(7)	0.085(14)
	U ²²	0.007(3)	0.019(7)	0.038(5)	0.047(7)	0.085(14)
Si	x	0.2368(2)	0.2357(2)	0.2358(1)	0.2352(2)	0.2348(2)
	y	0.3556(2)	0.3551(3)	0.3547(2)	0.3541(2)	0.3548(3)
	z	0.3872(1)	0.3877(2)	0.3877(1)	0.3881(1)	0.3880(2)
	B _{iso}	0.02(2)	0.32(3)			
	U ¹¹			0.004(1)	0.008(1)	0.012(1)
	U ²²			0.007(1)	0.009(1)	0.015(2)
Li	x	1/2	1/2	1/2	1/2	1/2
	y	1/2	1/2	1/2	1/2	1/2
	z	1/4	1/4	1/4	1/4	1/4
	B _{iso}	0.32(1)	1.3(2)			
	U ¹¹			0.025(3)	0.026(4)	0.031(6)
	U ²²			0.025(3)	0.026(4)	0.031(6)
O1	x	0.1364(2)	0.1354(4)	0.1375(2)	0.1364(3)	0.1373(4)
	y	0.3958(2)	0.3962(4)	0.3953(2)	0.3930(3)	0.3931(4)
	z	0	0	0	0	0
	B _{iso}	0.72(3)				
	U ¹¹		0.026(2)	0.036(1)	0.048(2)	0.046(3)
	U ²²		0.032(2)	0.036(1)	0.049(2)	0.056(3)
O2	x	0.2216(1)	0.2227(3)	0.2217(2)	0.2224(2)	0.2226(3)
	y	0.2767(1)	0.2772(3)	0.2765(2)	0.2768(2)	0.2772(3)
	z	0.1372(1)	0.1367(1)	0.1367(1)	0.1362(1)	0.1363(2)
	B _{iso}	0.74(2)				
	U ¹¹		0.018(1)	0.021(1)	0.031(1)	0.036(1)
	U ²²		0.021(1)	0.028(1)	0.033(1)	0.041(2)
O3	x	0.1645(1)	0.1656(2)	0.1649(1)	0.1657(2)	0.1661(2)
	y	0.5067(1)	0.5058(2)	0.5055(1)	0.5047(2)	0.5048(2)
	z	0.1700(1)	0.1692(1)	0.1690(1)	0.1687(1)	0.1692(1)
	B _{iso}	0.38(2)				
	U ¹¹		0.008(1)	0.015(1)	0.020(1)	0.020(1)
	U ²²		0.011(1)	0.011(1)	0.016(1)	0.022(1)

(continued on next page)

Table 4 (continued)

Atom	Parameter	298 K	573 K	723 K	923 K	1123 K
	U^{33}		0.016(1)	0.023(1)	0.031(1)	0.040(1)
	U^{12}		0.002(1)	0.007(1)	0.008(1)	0.006(1)
	U^{13}		0.002(1)	-0.004(1)	-0.004(1)	-0.004(1)
	U^{23}		-0.008(1)	-0.011(1)	-0.011(1)	-0.011(1)

*Defined as $\beta^1 h^2 + \beta^{22} k^2 + \beta^{33} l^2 + 2\beta^{12} hk + 2\beta^{13} hl + 2\beta^{23} kl$ with $\beta^{11} = 2\pi^2 U^{11} a^2$, $\beta^{22} = 2\pi^2 U^{22} b^2$, $\beta^{33} = 2\pi^2 U^{33} a^2$, $\beta^{12} = 2\pi^2 U^{12} a^2 b \cos \gamma$, $\beta^{13} = 2\pi^2 U^{13} a^2 c \cos \beta$, $\beta^{23} = 2\pi^2 U^{23} b^2 c \cos \alpha$. U^{ij} is the mean square displacement of the atom with respect to equilibrium position, defining the atomic temperature factor $B = 8\pi^2 U$.

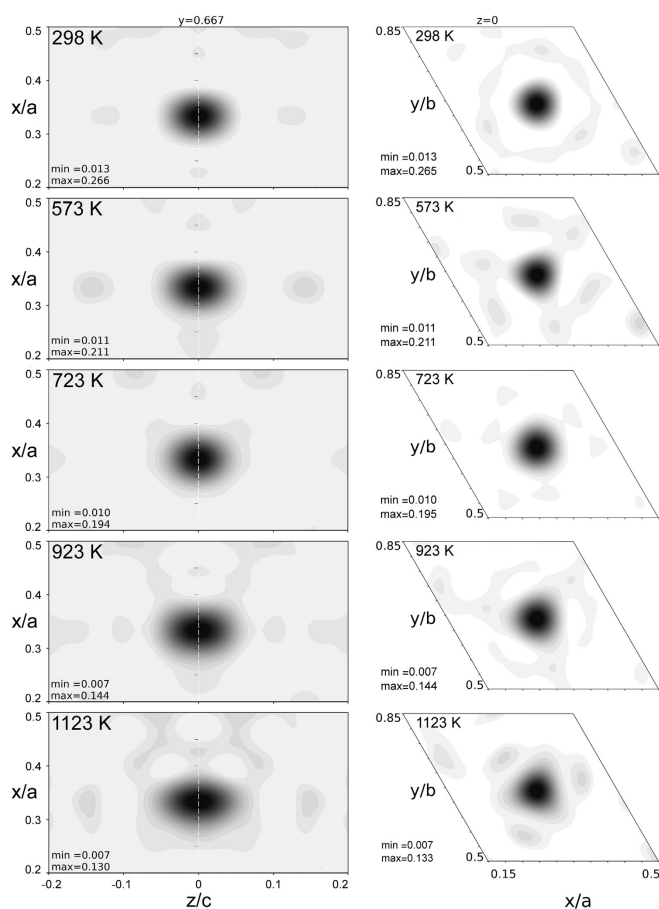


Fig. 7. ΔF maps around the split sites B on the $(a-c)$ plane (left) and the $(a-b)$ plane (right), evaluated from variable temperature HRNPD data with OCC of Na set to 0. Large diffuse nsf densities around the expected site of Na indicate pathways for conducting Na^+ in the sugilite-type topology.

B. Röska et al.

Journal of Solid State Chemistry 264 (2018) 98–107

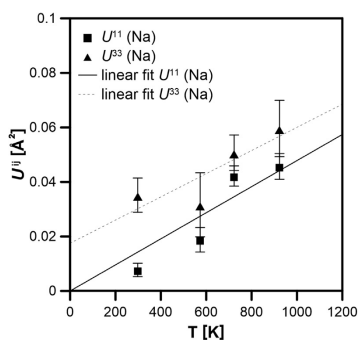


Fig. 8. Anisotropic ADPs for Na refined with HRNPD data between 298 K and 1123 K.

[001] with $U^{33} > U^{11} = U^{22}$ (Table 4). Furthermore, the trapezoidal void indicated in Fig. 12b spanned up by two O1 and two O3 offers a wider opening ($d(O1-O3) \approx 4.53 \text{ \AA}$) approximately at $z = 0.08$ whereas a direct site exchange near $z = 0$ is narrowed by two O1 sites only 4.25 \AA apart. It is expected that increasing transitory widening of this bottleneck through substantial thermal motions at O1 and O3 promotes Na^+ diffusion at higher temperatures. On the other hand, Na' site exhibits nominally to short oxygen bonding distances [26] for Na-cations ($d(\text{Na}'-O1) = 2.132 \text{ \AA}$), meaning that a temporary residence of Na at Na' is highly dependent on temperature induced dynamic disorder of the oxygen environment of Na' . In this way, the hopping pathways of Na are confined in the (*a-b*) plane.

Recall that the Na content (0.36 pfu) in sogdianite is significantly lower compared to sugilite-type compounds (2 pfu) whereas their Li contents are same (3 pfu). The charge transfer by both Li^+ and Na^+ in synthetic sugilite is obvious when comparing its bulk conductivity to those of mineral samples of sogdianite and sugilite (Table 7). In fact, a massive sugilite sample showed a σ_{DC} conductivity value of $1.7 \times 10^{-5} \text{ S cm}^{-1}$ already at 943 K, but sogdianite reached the same conductivity first at 1219 K in the (*a-b*) plane. It is expected that the ionic conductivity in the

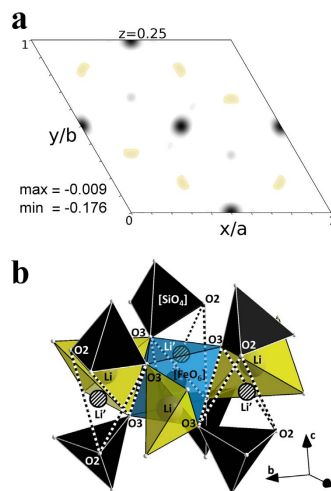


Fig. 9. Negative residuals (yellow) could be clearly observed in the ΔF map evaluated from the analysis with 1123 K HRNPD data and assigned to a new interstitial site Li' enclosing the centred A site (a). Large dark spots represent regular Li sites (T2) when its occupancy is set equal to zero. The new Li' sites fill tetrahedral voids between two $[\text{SiO}_4]$ tetrahedra (b).

pressed powder sample of the synthetic sugilite has much larger extrinsic contributions, such as grain boundary charge transfer. Therefore, its σ_{DC} values are two orders of magnitude smaller than those measured with a compact mass of natural sugilite sample. Nonetheless, its direction-averaged bulk conductivity is as high as that measured along the ionic conduction pathway in a sogdianite single crystal. To exclude extrinsic charge transfer phenomena, it is necessary to make large single crystals of synthetic counterparts to compare direction-dependent conductivity

Table 5
Interatomic distances resulting from HRNPD analyses between 298 K and 1123 K. BVS values are given for 298 K. (* = equivalent sites).

Site	ligands	Bonding distance [Å]					BVS (298 K)
		298 K	573 K	723 K	923 K	1123 K	
A (Fe)	O3 (x6)	2.002(1)	2.009(2)	2.017(1)	2.020(1)	2.016(3)	0.518(2) x6 $\Sigma = 3.108(4)$
B (Na)	O1 (x3)	2.450(2)	2.458(3)	2.453(2)	2.485(2)	2.496(4)	0.174(1) x3
	O3 (x3)	2.727(1)	2.679(2)	2.741(1)	2.665(1)	2.600(2)	0.082(1) x3
	O3* (x3)	3.101(2)	3.140(2)	3.078(1)	3.157(1)	3.247(3)	0.030(1) x3 $\Sigma = 0.858(2)$
C (K)	O2 (x12)	3.006(1)	3.020(2)	3.014(2)	3.024(2)	3.029(3)	0.094(1) x12 $\Sigma = 1.130(1)$
T1 (Si)	O1	1.626(1)	1.624(3)	1.623(2)	1.617(2)	1.621(3)	0.994 (4)
	O2	1.625(3)	1.620(5)	1.623(3)	1.617(3)	1.629(5)	0.998 (7)
	O2*	1.625(2)	1.623(4)	1.621(2)	1.622(2)	1.617(4)	0.998 (5)
	O3	1.573(2)	1.569(3)	1.568(2)	1.568(2)	1.568(3)	1.147(5) $\Sigma = 4.14(1)$
T2 (Li)	O3 (x4)	1.975(1)	1.996(2)	1.994(1)	2.008(2)	2.009(3)	0.253(1) x4 $\Sigma = 1.011(2)$

B. Röska et al.

Journal of Solid State Chemistry 264 (2018) 98–107

Table 6
Bonding distances and BVS of the interstitial sites Na' and Li' evaluated from HRNPD data collected at 1123 K.

Site	Bonding partner	Bonding distance [Å]	BVS
Li' ($\frac{1}{6}, \frac{1}{3}, \frac{1}{4}$)	$O2 \times 2$	1.887(3)	0.321(2) $\times 2$
	$O3 \times 2$	2.076(2)	0.192(1) $\times 2$
	av.: 1.981(3)		Σ 1.026(6)
Na' ($\frac{1}{2}, \frac{1}{2}, 0$)	$O1 \times 2$	2.132(4)	0.410(4) $\times 2$
	$O3 \times 4$	2.906(2)	0.051(1) $\times 4$
	av.: 2.648(3)		Σ 1.024(6)

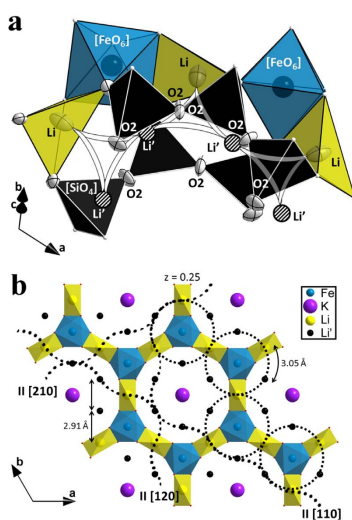


Fig. 10. Schematic representation of site-exchanges of Li at 1123 K over an interstitial Li' site (a). An infinite 2D network of hopping pathways is formed through regular and interstitial sites for Li in the (a-b) plane (b).

values in this system. This is indispensable not only to assign three resonance modes observed, but also to resolve intrinsic slow and fast relaxation modes due to charge transfer processes of Li^+ and Na^+ .

4. Conclusion

The synthesis parameters of the new Fe-pure end-member sugilite analogue, $Fe_2Na_2K[Li_3Si_{12}O_{30}]$ were determined for hydrothermal routes. Structural changes and charge transfer mechanism for Li^+ and Na^+ were analysed using neutron powder diffraction between 298 K and 1123 K. Its bulk ionic conductivity values between 723 K and 923 K are comparable to those determined with single crystal sodgianite parallel to the $[AO_6-T2O_4]$ chains. As proved in sodgianite, Li^+ cations site-exchange via interstitial sites of the $[FeO_6-LiO_4]$ network. Residual diffuse nsf densities in ΔF maps strongly point to anharmonic motion of Na and, more interestingly, an unexpected 2D network for conducting Na^+ . This route is located directly in-between two $[FeO_6]-[LiO_4]$ layers. Hence, the dynamic disorder of both charge carriers Na^+ and Li^+ is confined commonly in the (a-b) plane. This new finding explains

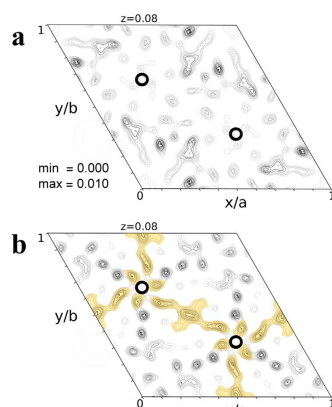


Fig. 11. ΔF maps from HRNPD analysis at $z = 0.08$ slightly above the site B at $z = 0$ (bold black circles) at 298 K (a) and at 1123 K (b). Continuous positive residuals of nsf densities indicate possible Na^+ diffusion pathways, as highlighted in pale yellow, over the new interstitial site Na' at $(\frac{1}{2}, \frac{1}{2}, 0)$ slightly below the centre of this plot.

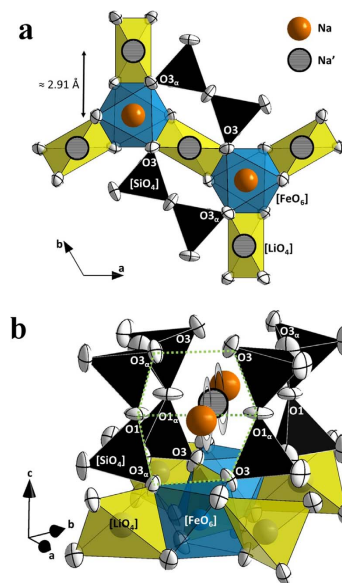


Fig. 12. Top view of the $[FeO_6-LiO_4]$ chains upon which the overlying network of Na at B and Na' interstitial sites (a). Side view of the pathway for site-exchanging Na through $O1-O1a-O3-O3a$ trapezoidal voids (dashed lines in green) in (b). The subscript α denotes symmetry-equivalent sites.

the enhanced conductivity in Na-enriched end-members in the sugilite-sodgianite solid solution. Along with its high moisture and thermal stability, $Fe_2Na_2K[Li_3Si_{12}O_{30}]$ deserves further investigation to develop stable and effective Li^+/Na^+ -ionic conductors.

B. Röska et al.

Journal of Solid State Chemistry 264 (2018) 98–107

Table 7
Comparison of conductivity values and potential charge carriers per Si_2O_3 unit in massive aggregates of sugilite crystal, the synthetic sugilite powder, and a sogdianite single crystal.

Compound	Ionic conductivity [S cm^{-1}]	Na [pfu]	Li [pfu]
sugilite (Park et al., to be published)	1.7×10^{-3} (943 K)	2	3
$\text{Fe}_2\text{Na}_2\text{K}[\text{Li}_3\text{Si}_2\text{O}_{10}]$	1.2×10^{-5} (923 K)	2	3
sogdianite \perp [001] [1]	4.1×10^{-5} (923 K)	0.36	3
	1.2×10^{-7} (1219 K)		

Acknowledgement

SHP acknowledges the financial support from German Federal Ministry of Education and Research (BMBF) via 05K13WMB and the exchange program JSPS/DAAD for BR via PE 15779.

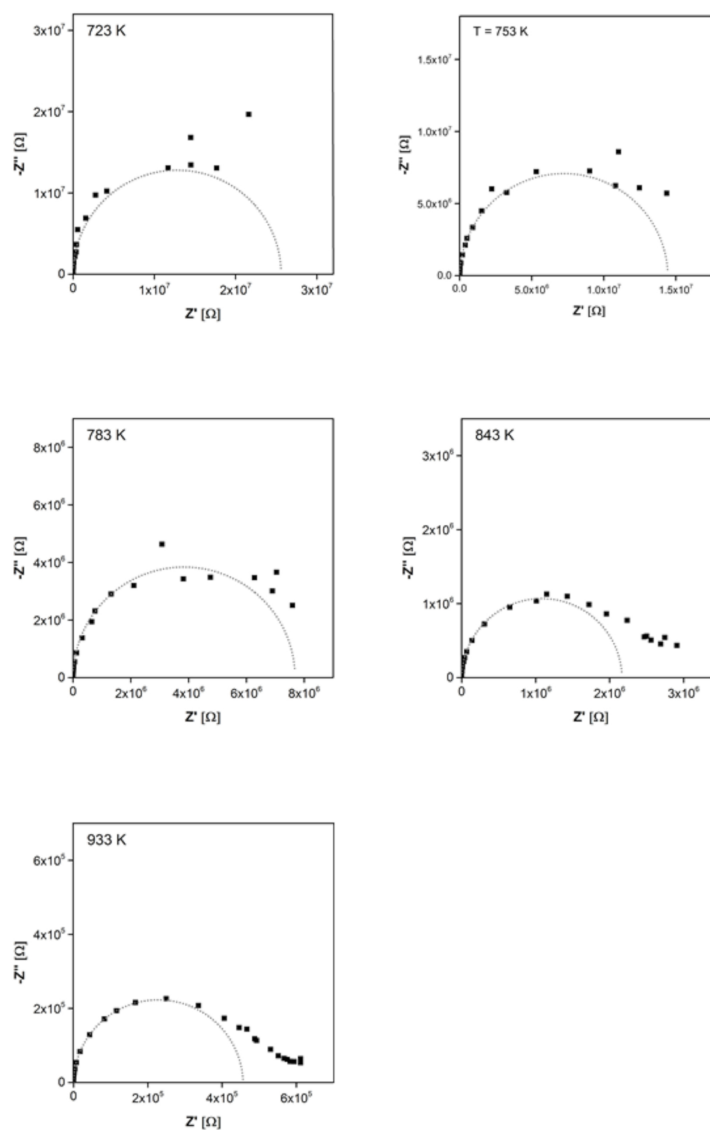
Appendix A. Supplementary data

Supplementary data associated with this article can be found in the online version at <http://dx.doi.org/10.1016/j.jssc.2018.05.008>.

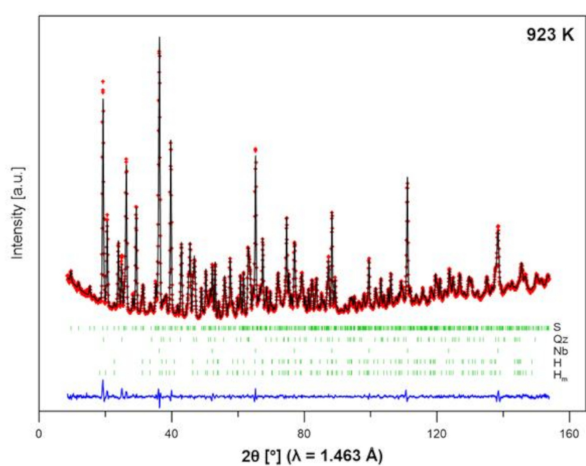
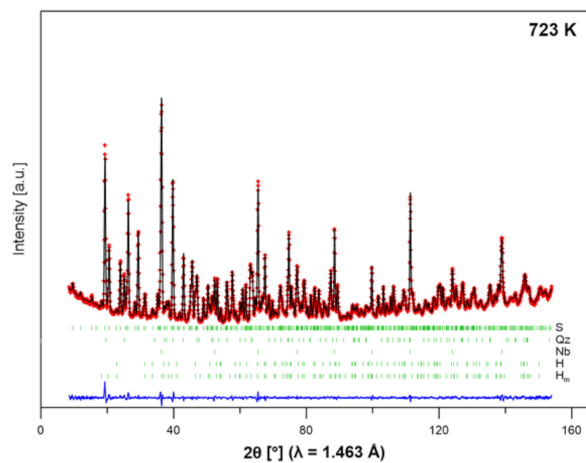
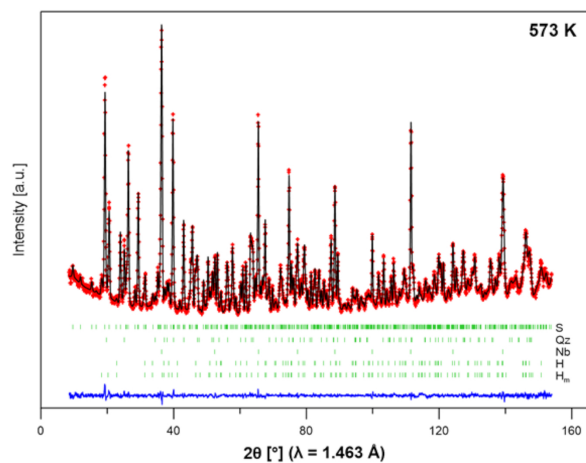
References

- [1] S.-H. Park, M. Hoelzel, H. Boysen, E. Schmidbauer, Lithium conductivity in a Li-bearing double-ring silicate mineral, sogdianite, *J. Solid State Chem.* 180 (4) (2007) 1306–1317. <http://dx.doi.org/10.1016/j.jssc.2007.02.001>.
- [2] N. Murakami, T. Kato, Y. Miura, Sugilite, a new silicate mineral from Iwagi Islet, Southwest Japan, *Mineral. J.* 8 (2) (1976) 110–121.
- [3] T.M. Kato, Y., Crystal structure of sugilite *Mineral. J.* 8, 8, 1976, 184–192.
- [4] T. Armbruster, R. Oberhänsli, Crystal chemistry of double-ring silicates: structures of Sugilite and Brannockite, *Am. Mineral.* 73 (1988) 595–600.
- [5] M.A. Cooper, F.C. Hawthorne, E.S. Grew, The crystal chemistry of sogdianite, a milarite-group mineral, *Am. Mineral.* 84 (1999) 764–768.
- [6] G. Ferraris, M. Frencipe, L.A. Pautov, E.V. Sokolova, The crystal structure of darapsite and a comparison with Li- and Zn-bearing minerals of the milarite group, *Can. Mineral.* 37 (3) (1999) 769–774.
- [7] E.V. Sokolova, F.C. Hawthorne, L.A. Pautov, The crystal chemistry of Li-bearing minerals with the milarite-type structure: the crystal structure of end-member sogdianite, *Can. Mineral.* 38 (2000) 835–859.
- [8] W.C. Forbes, W.H. Baur, A.A. Khan, Crystal Chemistry of milarite-type minerals, *Am. Mineral.* 57 (1972) 463–472.
- [9] F.C. Hawthorne, M. Kimata, P. Cerny, N.A. Ball, G.R. Rossman, J.D. Grice, Crystal chemistry of the milarite-group minerals, *Am. Mineral.* 76 (1991) 1836–1856.
- [10] P.J. Dunn, J.J. Brummer, H. Belsky, Sugilite, a second occurrence: Wessels mine, Kalahari manganese field, Republic of South Africa, *Can. Mineral.* 18 (1980) 37–39.
- [11] A.M. Clark, E.E. Fejer, A.G. Couper, G.S. Bearne, V.K. Din, Additional data on Sugilite, *Mineral. Mag.* 43 (1980) 947–949.
- [12] O.C. Gagné, F.C. Hawthorne, Chemographic exploration of the milarite-type structure, *Can. Mineral.* 54 (5) (2016) 1229–1247. <http://dx.doi.org/10.3749/canmin.1500088>.
- [13] J. Rodriguez-Carvajal, FullProf Suite, 2011.
- [14] M. Hoelzel, A. Senyshyn, N. Juenke, H. Boysen, W. Schmah, H. Fuess, High-resolution neutron powder diffractometer SPODI at research reactor FRM II, *Nucl. Instrum. Methods Phys. Res. Sect. A: Accel. Spectromet. Detect. Assoc. Equip.* 667 (2012) 32–37. <http://dx.doi.org/10.1016/j.nima.2011.11.070>.
- [15] I.D. Brown, D. Altermatt, Bond-valence parameters obtained from a systematic analysis of the Inorganic Crystal Structure Database, *Acta Crystallogr. Sect. B Struct. Sci.* 41 (4) (1985) 244–247. <http://dx.doi.org/10.1107/S0108768185002063>.
- [16] B. Warnes, F. Aplan, G. Simkovich, Electrical conductivity and seebeck voltage of Fe_2O_3 , pure and doped, as a function of temperature and oxygen pressure, *Solid State Ion.* 12 (1984) 271–276. [http://dx.doi.org/10.1016/0167-2738\(84\)90156-5](http://dx.doi.org/10.1016/0167-2738(84)90156-5).
- [17] H. Mansour, H. Letifi, R. Bargougui, S. De Almeida-Didry, B. Negulescu, C. Autret-Lambert, A. Gadi, S. Ammar, Structural, optical, magnetic and electrical properties of hematite (α - Fe_2O_3) nanoparticles synthesized by two methods: polyol and precipitation, *Appl. Phys. A* 123 (12) (2017) 787. <http://dx.doi.org/10.1007/s00339-017-1408-1>.
- [18] K. Ishikawa, T. Yoshioka, T. Sato, A. Okuwaki, Solubility of hematite in LiOH, NaOH and KOH solutions, *Hydrometallurgy* 45 (1–2) (1997) 129–135. [http://dx.doi.org/10.1016/S0304-386X\(96\)00688-0](http://dx.doi.org/10.1016/S0304-386X(96)00688-0).
- [19] U. Simon, M. Franke, Electrical properties of nanoscaled host/guest compounds, *Microporous Mesoporous Mater.* 41 (1–3) (2000) 1–36. [http://dx.doi.org/10.1016/S1387-1811\(00\)00291-2](http://dx.doi.org/10.1016/S1387-1811(00)00291-2).
- [20] V.F. Lvovich, Impedance Spectroscopy: Applications to Electrochemical and Dielectric Phenomena, 2012.
- [21] R.J. Harrison, Neutron diffraction of magnetic materials, *Rev. Mineral. Geochem.* 63 (1) (2006) 113–143. <http://dx.doi.org/10.2138/rmg.2006.63.6>.
- [22] R.M. Cornell, U. Schwertmann, *The Iron Oxides: Structure, Properties, Reactions, Occurrences and Uses*, Wiley-VCH, Weinheim, Germany, 2003.
- [23] C. Giacobozzo, H.L. Monaco, G. Artioli, D. Viterbo, M. Milanesio, G. Ferraris, G. Gilli, P. Gilli, G. Zanotti, M. Catti, C. Giacobozzo, *Fundamentals of Crystallography*, Oxford, University Press Inc., New York, 2011.
- [24] T. Armbruster, V. Bermanec, M. Wenger, R. Oberhänsli, Crystal structure of double-ring silicates: structure of natural and dehydrated milarite at 100 K, *Eur. J. Mineral.* 1 (1989) 353–362.
- [25] P. Cerny, F.C. Hawthorne, E. Jarosewich, Crystal chemistry of milarite, *Can. Mineral.* 18 (1) (1980) 41.
- [26] I.D. Brown, R.D. Shannon, Empirical bond-strength-bond-length curves for oxides, *Acta Crystallogr. Sect. A* 29 (3) (1973) 266–282. <http://dx.doi.org/10.1107/S0567739473000689>.
- [27] A. Robertson, A. West, A. Ritchie, Review of crystalline lithium-ion conductors suitable for high temperature battery applications, *Solid State Ion.* 104 (1–2) (1997) 1–11. [http://dx.doi.org/10.1016/S0167-2738\(97\)00429-3](http://dx.doi.org/10.1016/S0167-2738(97)00429-3).
- [28] M. Nakayama, Y. Ishida, L.H. M. Wakihara, Mixed conduction for the spinel type $(1-x)\text{Li}_{1/3}\text{Ti}_{5/3}\text{O}_{14}\text{LiCrTiO}_4$ system, *Solid State Ion.* 117 (3–4), 1999, 265–271. [http://dx.doi.org/10.1016/S0167-2738\(98\)00418-4](http://dx.doi.org/10.1016/S0167-2738(98)00418-4).

Supplementary 1: Complex plane plots measured at 723 K, 753 K, 783 K, 843 K, and 933 K with fittings of high-frequency semicircles (grey).



Supplementary 2: Graphical representations of Rietveld refinements of HRNPD data acquired at 573 K, 723 K, and 923 K.



13. Publication on eosphorite

IOP Publishing

Journal of Physics: Condensed Matter

J. Phys.: Condens. Matter **29** (2017) 365401 (5pp)

<https://doi.org/10.1088/1361-648X/aa7adf>

Anomalous dielectric response of short hydrogen bonds under pressure: the case of $(\text{Mn,Fe})^{2+}\text{AlPO}_4(\text{OH})_2\text{H}_2\text{O}$

B Röska¹, S-H Park^{1,3}, Y Yoshimori², K Kimura² and T Kimura²

¹ Department of Earth and Environmental Sciences, Section of Crystallography, Ludwig-Maximilians-Universität, Munich, Germany

² Division of Materials Physics, Graduate School of Engineering Science, Osaka University, Toyonaka, Osaka 560-8531, Japan

E-mail: sohyun.park@lmu.de

Received 8 May 2017, revised 20 June 2017

Accepted for publication 21 June 2017

Published 4 August 2017



CrossMark

Abstract

An anomalous increase in the real part of dielectric response is observed in $\text{Mn}_{0.5}\text{Fe}_{0.5}\text{AlPO}_4(\text{OH})_2\text{H}_2\text{O}$ while cooling to $\sim 70\text{ K}$. This is addressed to field-induced proton dynamics in a short hydrogen bond of $2.480(3)\text{ \AA}$. The absence of discontinuities in heat capacity curves above the Néel temperature ($T_N \approx 7\text{ K}$) excludes a paraelectric to antiferroelectric phase transition. Upon the application of mild hydrostatic pressures below 1.6 GPa , the maximum in the dielectric response is shifted from 70 K to lower temperatures near 2 K . This explains a narrow correlation between proton transfer and the compression of the short hydrogen bond length.

Keywords: proton motion, hopping polarisation, short hydrogen bonds, phosphatic oxyhydroxides, eosphorite-childrenite series

Supplementary material for this article is available [online](#)

(Some figures may appear in colour only in the online journal)

1. Introduction

Several H-bearing compounds undergo (anti-)ferroelectric transitions accompanied by proton ordering within short hydrogen bonds less than 2.50 \AA , such as KH_2PO_4 (KDP)-type structures, squaric acid ($\text{H}_2\text{C}_4\text{O}_4$), or mono-protonated diazabicyclo[2.2.2]octane (HdabcoH^+) derivatives [1, 2]. The proton order-disorder transition can be manipulated by applying pressure to alter the bonding distance between the donor and the acceptor. Short hydrogen bonds near the symmetrisation length of about 2.39 \AA [3] are regarded as a relevant prerequisite for which proton displacements are susceptible to manipulation under low pressures. For instance, a quantum paraelectric state occurs in antiferroelectric squaric acid crystals when applying $\sim 3\text{ GPa}$ to compress the short acceptor-donor distance of 2.55 \AA down to $\sim 2.45\text{ \AA}$ near to

the symmetric hydrogen bonding state $\text{O}\cdots\text{H}\cdots\text{O}$ [4]. The ferroelectricity in KDP-type salt crystals can be suppressed by retaining the disorder state of protons at 1.7 GPa [5]. In a rigid structure, goethite ($\alpha\text{-FeOOH}$), much higher pressures of about 20 GPa are necessary to shorten the hydrogen bonding distance from $\sim 2.7\text{ \AA}$ to $\sim 2.5\text{ \AA}$ [6]. Phosphatic oxyhydroxides exhibit a more flexible framework containing $(\text{OH})^-$, (H_2O) , and O^{2-} ligands. For example, the eosphorite-childrenite solid solution minerals $M\text{AlPO}_4(\text{OH})_2\text{H}_2\text{O}$ ($M = \text{Mn}^{2+}$ and Fe^{2+}) are built with strongly distorted $\text{MO}_4(\text{OH}, \text{H}_2\text{O})_2$ and more regular $\text{AlO}_2(\text{OH})_2(\text{OH}, \text{H}_2\text{O})_2$ octahedra [7–10], as illustrated in figure 1. Their OH^- and H_2O groups are involved in hydrogen bonds of varying strengths. For $(\text{Mn}_{0.5}\text{Fe}_{0.5})\text{AlPO}_4(\text{OH})_2\text{H}_2\text{O}$, its antiferromagnetic state was recently elucidated [10]; the magnetic order ($T_N = 6.5\text{--}6.8\text{ K}$) is described in the magnetic space group $\text{Pc}mn2_1$, maintaining the crystallographic unit cell size ($a \times b \times c$) with $a \approx 6.9\text{ \AA}$, $b \approx 10.4\text{ \AA}$, $c \approx 13.4\text{ \AA}$.

³ Author to whom any correspondence should be addressed.

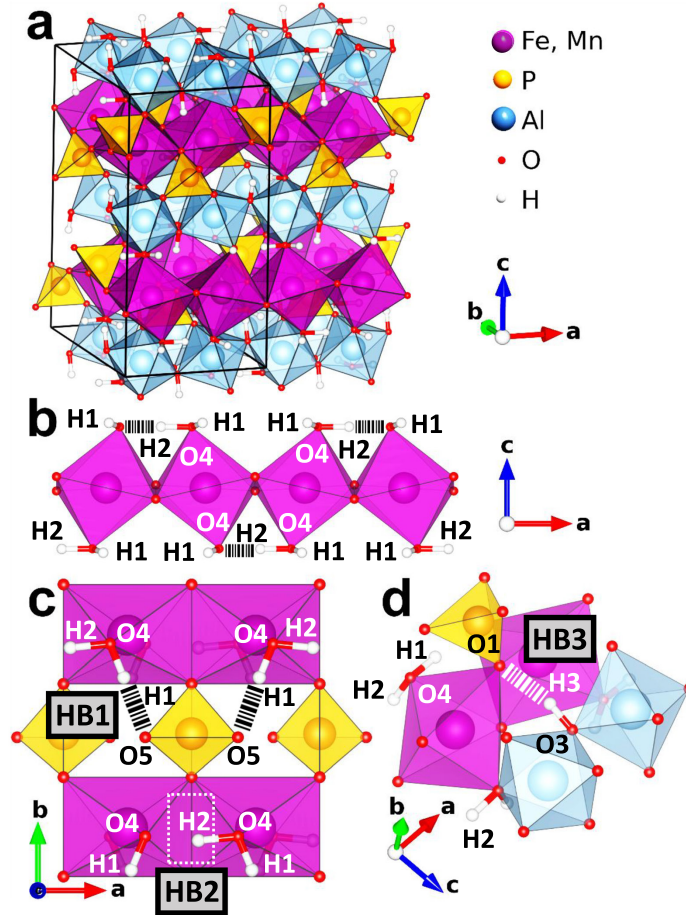


Figure 1. (a) Crystal structure of $MAIPO_4(OH)_2H_2O$ ($M = Fe^{2+}, Mn^{2+}$) consisting of $MO_4(OH, H_2O)_2$ and $AlO_4(OH, H_2O)_2$ octahedra chains; (b) $MO_4(OH, H_2O)_2$ octahedra chains with the hydrogen bond HB2 in H1-O4-H2...O4-H1; (c) two hydrogen bonds HB1 and HB2 are related to the H_2O group. The white dashed box marks the calculation area of difference Fourier maps depicted in figures 2(a) and (b); (d) the long hydrogen bond HB3.

Nothing is known about the subtle influence of proton disorder on dielectric properties of this compound, inheriting an unusually short hydrogen bond of 2.480(3) Å at ambient conditions. The present study reports a remarkable temperature-dependent dielectric response of $Mn_{0.5}Fe_{0.5}AlPO_4(OH)_2H_2O$. Its dielectric behaviour is highly sensitive to mild pressures below 2 GPa, so that alteration of hydrogen bonds could be resolved. To the best of our knowledge, this is the first study of anomalous dielectric behaviour of short hydrogen bonds in phosphatic oxyhydroxides.

2. Materials and methods

Large natural single crystals originating from Minas Gerais, Brazil were oriented-cut perpendicular to the main crystallographic directions using Laue camera. The heat capacity of $Mn_{0.5}Fe_{0.5}AlPO_4(OH)_2H_2O$ was measured between 10 and 300 K above T_N using the thermal relaxation method in a physical properties measurement system (PPMS) from Quantum Design. Using the PPMS, the samples were tempered between 2 and 300 K while recording dielectric responses along the a -,

Table 1. Three hydrogen bonds present in $(\text{Mn}_{0.5}\text{Fe}_{0.5})^{2+}\text{AlPO}_4(\text{OH})_2\text{H}_2\text{O}$ at 298 K, their geometries, and alignments with respect to the main crystallographic axes.

Name denoted as	Hydrogen bond (HB) sites	Distance between HB oxygens: $d(\text{O}-\text{O})$ (Å)	Angle $\angle(\text{O}-\text{H}\cdots\text{O})$ (°)	O–O elongation
HB1	O4-H1...O5	2.741(2)	163.1(3)	Preferred in the b -direction on the ab -plane
HB2	O4-H2...O4	2.480(3)	170.1(5)	$\parallel a$
HB3	O3-H3...O1	2.779(2)	154.7(4)	$\parallel c$

b -, and c -direction with an Agilent E4980 LCR meter. Silver electrodes were vacuum-evaporated on the crystal faces after polishing crystals to plates of 100 μm thickness. Hydrostatic pressure was produced within a clamp-cell using Daphne oil as a pressure-transmitting medium. The pressure-sensitive transition of Pb to its superconducting state was referred as *in situ* barometer by monitoring the inductance of a wire wrapped around a piece of Pb [11]. Auxiliary structural and chemical information was taken from our recent study using electron micro probe analysis and neutron single crystal diffraction (NSCD) [10].

3. Results and discussion

The eosphorite-childrenite series crystallize in the space group *Cmce* (#64) without structural phase transitions below 300 K [7–10]. In this topology, chains of $\text{MO}_4(\text{OH}, \text{H}_2\text{O})_2$ and $\text{AlO}_4(\text{OH}, \text{H}_2\text{O})_2$ octahedra are arranged parallel to the a -axis (figure 1(a)). These chains are linked to each other in the c -direction via bridging $(\text{OH})^-$ and (HOH) groups and connected to rigid PO_4 tetrahedra in both the a - and b -directions. As a result, a 3D framework which is thermally stable up to 715 K is created [10, 12]. As shown in figures 1(b)–(d), in this structure there are three independent hydrogen positions in hydrogen bonds which differ considerably in their geometries [9, 10]. These hydrogen bonds, i.e. O4-H1...O5, O4-H2...O4 and O3-H3...O1 are named HB1, HB2 and HB3, respectively. As given in table 1, HB1 and HB3 present much longer hydrogen bonds than HB2. The latter features a very short acceptor–donor distance of 2.480(3) Å at an almost linear alignment, i.e. $\angle(\text{O4-H2}\cdots\text{O4}) = 170.1(5)^\circ$. According to NSCD analyses [9, 10], protons are statically disordered at H2, showing a site splitting of ~ 0.35 Å. The half-occupation of H2 points to two equally abundant asymmetric configurations of HB2: O4-H2...O4 and O4...H2-O4. In difference Fourier maps (figure 2) evaluated with NSCD data at 298 and 3 K [10], the density of negative coherent neutron scattering lengths (Cohb for $H = -3.739$ fm) around H2 becomes increasingly diffuse, preferably perpendicular to the hydrogen bond direction at elevated temperatures. The respective root mean square atomic displacement parameters (*rms* ADPs) in [100], [010], and [001] show a high anisotropy, i.e. $U_1 \ll U_2 < U_3$ [10]. On the other hand, the *rms* ADPs of H2 in [100] at both 298 and 3 K are nearly equal to zero [10]. This flat tendency of *rms* ADPs towards the absolute zero temperature points to purely static disorder of protons over H2 sites. Thus, a thermally-activated proton transfer process could

be excluded in the strong hydrogen bond HB2 below 300 K despite the short distance of its split sites ~ 0.35 Å apart.

As presented in figure 3(a), the heat capacity curve shows no discontinuity above T_N in accordance with [10]. Therefore, a long-range order-disorder phase transition caused by correlated hydrogen ordering is excluded. Figure 3(b) demonstrates the temperature-dependent real part permittivity in the [100] direction (ϵ'_a). A steady increase in the range of 300–70 K is followed by a steep decrease below 70 K. Frequency-dispersive ϵ'_a curves are detected in a range of 300–200 K as well as below 40 K. The former cannot be assigned unequivocally to sample inherent properties, but might be related to artificial sample electrode interface effects. Similar dispersions are found in the same temperature interval in the real part permittivities along the [010] and [001] directions (supplementary 1) (stacks.iop.org/JPhysCM/29/365401/mmedia).

The dielectric response of $\text{Mn}_{0.5}\text{Fe}_{0.5}\text{AlPO}_4(\text{OH})_2\text{H}_2\text{O}$ along the a -direction in the kHz range can be attributed to the high polarizability of hydrogen bonds, where the proton transfer is stimulated by the applied alternating current electric field [13]. The unusual tendency of ϵ'_a (figure 3(b)) is related to the short length of HB2 of 2.480(3) Å at 298 K; 2.474(5) Å at 3 K [10]. These distances are, however, not small enough to form the symmetric hydrogen bond configuration O4...H2...O4 [3]. In addition, protons occupying the split H2 sites are at ease with hopping between two energetically equal configurations, i.e. H1-O4...H2-O4-H1 and H1-O4-H2...O4-H1. Nonetheless, as aforementioned, below and at room temperature thermal activation is not sufficient for protons to readily hop between the two bordering O4 atoms in the absence of external electric fields (E_{AC}). Thus the steady increase of ϵ'_a toward lower temperatures in the range of 300–70 K is explained by E_{AC} -induced proton transfer within the short hydrogen bond HB2. The response of the proton transfer within HB2 to the stimulus E_{AC} becomes more effective with decreasing temperature, as demonstrated by an uncommonly steady increase of ϵ'_a up to the maximum around 70 K (T_m). This is mainly for two reasons: (1) the shortening of the bonding distance $d(\text{O4}-\text{O4})$; (2) the reduced *rms* ADPs perpendicular to the bonding direction with decreasing temperatures [10]. At temperatures below ~ 70 K, however, the potential barrier becomes dominant and abates the E_{AC} -stimulated dipole alignment within HB2 as the continuous lowering of ϵ'_a is observed. A frequency-dispersive ϵ'_a drop near 40 K is attributed to the freezing of E_{AC} -induced proton transfer in HB2. Furthermore, the temperature for the maximum ϵ'_a value (T_m) varies about ± 10 K while repeating dielectric measurements with several specimens from the same batch. This variation is due to the presence of several

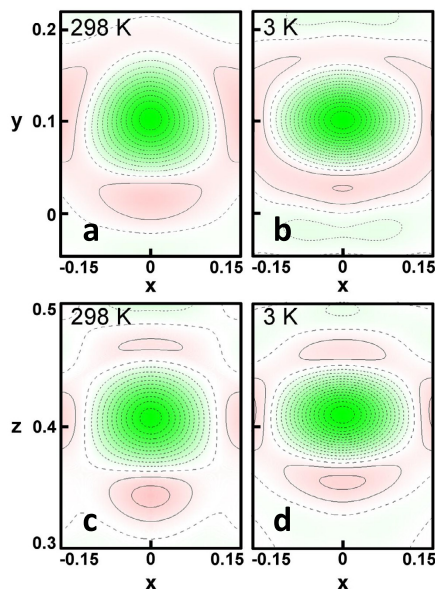


Figure 2. Difference Fourier ($\Delta F = F_o - F_c$) maps around the H2 split sites at $z = 0.48$ in the xy -plane (a) and (b) and at $y = 0.10$ in the xz -plane (c) and (d), evaluated using neutron single crystal diffraction data at 298 and 3 K [10]. The occupancy at H2 was set to zero for mapping protons with negative coherent neutron scattering length (Cohb). The averaged habitation area of protons is superposed by two close H2 split sites 0.35 Å apart. Negative (greenish marked with dashed lines) and positive (reddish marked with solid lines) densities are mapped between -13.7 and 3.2 (Cohb Å⁻³).

hundred μm -sized chemical zones with varying Mn/Fe ratios in our mineral samples [10]. Their different ionic radii r_i (for six-fold coordination: $r_i(\text{Mn}^{2+}) = 0.83$ Å; $r_i(\text{Fe}^{2+}) = 0.78$ Å [14]) influence the geometry of neighbouring $\text{MO}_4(\text{OH}, \text{H}_2\text{O})_2$ octahedra, and thus the bonding distance $d(\text{O4-O4})$ is affected. It is concluded that E_{AC} -induced proton transfer is very sensitive to a tiny change of the short $d(\text{O4-O4})$ distance.

This dependence is further examined by measuring ϵ'_a isobars up to 1.51 GPa as a function of temperature (figure 4). T_m is highly impacted by increasing pressure as shifting towards lower values. This inverse pressure proportionality of T_m indicates the compression of $d(\text{O4-O4})$. The more this distance is reduced with increasing pressure, the less thermal activation is required for aligning protons in HB2 by the electric field, accordingly. At 1.51 GPa, the ϵ'_a value steadily increases since the maximal polarizability is not reached even at 2 K. This means that the bond symmetrisation $\text{O4}\cdots\text{H2}\cdots\text{O4}$ is not obtainable in this pressure and temperature region. Otherwise the stimulated polarization represented by ϵ'_a would tend to zero. As illustrated in the inset of figure 4, the shift of the T_m values at elevated pressures shows two distinct overall

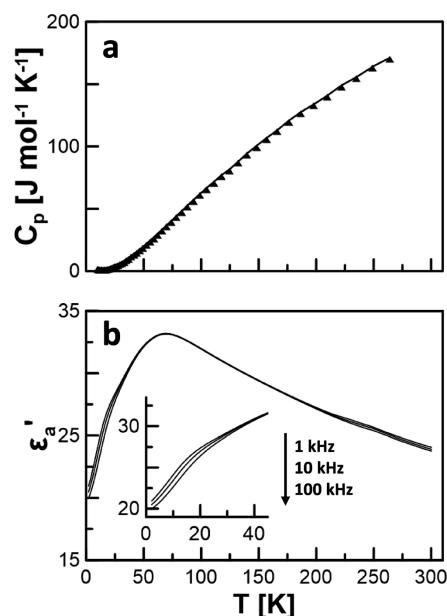


Figure 3. (a) Heat capacity which confirms no phase transition between 10 and 300 K; (b) real part permittivity ϵ'_a recorded from 2 to 300 K with a rate of 2 K min^{-1} along the [100] direction.

gradients: -90 K GPa^{-1} up to -0.9 GPa ; -20 K GPa^{-1} between 0.9 and 1.5 GPa. The flattened gradient points to a reduced compressibility above 0.9 GPa, which is possibly due to the incipient bond symmetrisation of HB2. Therefore, the steep gradient below 0.9 GPa reflects the delicate dependence of proton dynamics on minor changes of the distance between donor and acceptor within very short hydrogen bonds.

Although no phase transition was observed in our samples, their ϵ'_a curves are strikingly reminiscent of behaviours of some H-bonded antiferroelectric compounds. For example, ϵ'_a below ~ 1.5 GPa is very similar to the dielectric response of squaric acid at 1.2–2.9 GPa [4]. Thereby the order–disorder phase transition is shifted to lower temperatures through the abbreviation of hydrogen bond lengths. Another interesting case is the dielectric response of $\text{K}_3\text{H}(\text{SeO}_4)_2$ containing one single isolated hydrogen bond [15] of which the geometry is very similar to HB2 in $\text{Mn}_{0.5}\text{Fe}_{0.5}\text{AlPO}_4(\text{OH})_2\text{H}_2\text{O}$. No obvious discontinuity was resolved in the heat capacity data of $\text{K}_3\text{H}(\text{SeO}_4)_2$, also in [16]. However, according to the literature [16, 17], $\text{K}_3\text{H}(\text{SeO}_4)_2$ undergoes the antiferroelectric phase transition involving a proton ordering in the hydrogen bond at $\sim 20\text{ K}$. Further quantum effects are still debated to prove the role of the isolated proton dynamics in $\text{K}_3\text{H}(\text{SeO}_4)_2$ -type structures [18–20]. $\text{Mn}_{0.5}\text{Fe}_{0.5}\text{AlPO}_4(\text{OH})_2\text{H}_2\text{O}$ exhibits clusters of hydrogen bonds, e.g. $\text{O5}\cdots\text{H1-O4}\cdots\text{H2-O4-H1}\cdots\text{O5}$ (figure 1(c)). These clusters do not build up a percolating network

4

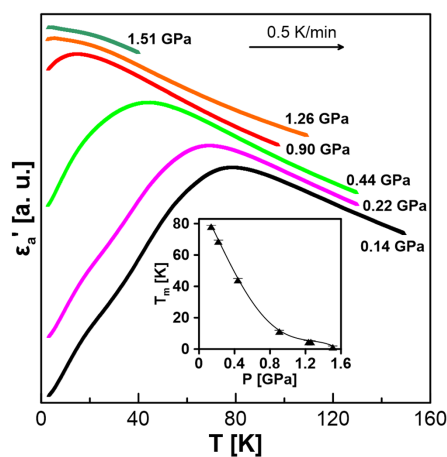


Figure 4. The dielectric permittivity (100kHz) isobars in [100]. The result shows a strong pressure-dependence of T_m , which is attributed to the compression of O4-H2...O4. The inset highlights the shift of T_m as a function of the applied isostatic pressure. For clarity, ϵ'_a isobars are off-shifted using arbitrary units.

where ferroelectric phase transitions due to the ordering of protons may not occur. The eosphorite-childrenite series provide unique conditions for proton dynamics in short hydrogen bonds. In this context, it is necessary to comprehend whether the tunnelling and quantum effects of protons in the hydrogen bond cluster contribute to anomalous dielectric behaviour.

4. Conclusion

The present study reports an anomaly in the dielectric response of $\text{Mn}_{0.5}\text{Fe}_{0.5}\text{AlPO}_4(\text{OH})_2\text{H}_2\text{O}$ which is not related to any (anti-)ferroelectric phase transitions. Two relevant conclusions are drawn: (1) proton freezing in the short hydrogen bond HB2 occurs in a non-collective manner; (2) the surprisingly high pressure-sensitivity of proton freezing relies on the confined geometry of the hydrogen bond HB2. Therefore, deuterated counterparts are desired to detect subtle changes of the bond geometry and (stimulated) transfer processes in short hydrogen bonds. Further spectroscopic and structural investigations in combined external fields are required to understand the nature and mechanism of proton dynamics in this family of structures.

Acknowledgments

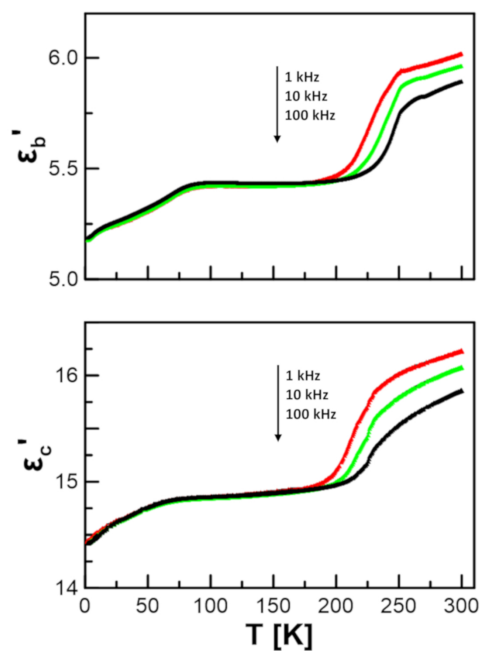
S H P acknowledges German Federal Ministry of Education and Research (BMBF) for the financial support via 05K13WMB. B R was funded in January to July 2016 by a scholarship from JSPS/DAAD (PE 15779). K K and T K

were supported by JSPS KAKENHI Grants 26610103 and 24244058, respectively.

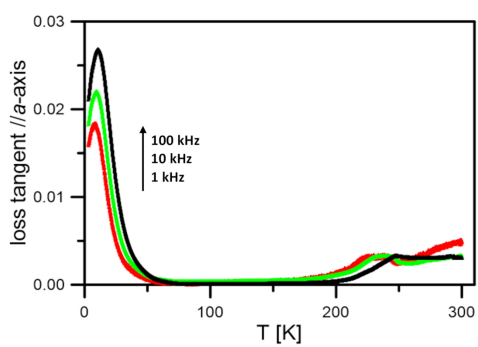
References

- [1] Horiuchi S, Kumai R and Tokura Y 2007 Hydrogen-bonded donor-acceptor compounds for organic ferroelectric materials *Chem. Commun.* **23** 2321–9
- [2] Horiuchi S and Tokura Y 2008 Organic ferroelectrics *Nat. Mater.* **7** 357–66
- [3] Steiner T 2002 The hydrogen bond in the solid state *Angew. Chem. Int. Ed.* **41** 49–76
- [4] Moritomo Y, Tokura Y, Takahashi H and Mōri N 1991 Quantum paraelectricity and subsequent disappearance of bond alternation of molecule caused by proton dynamics in squaric acid crystals *Phys. Rev. Lett.* **67** 2041–4
- [5] Samara G A 1971 Vanishing of the ferroelectric and antiferroelectric states in KH_2PO_4 -type crystals at high pressure *Phys. Rev. Lett.* **27** 103–6
- [6] Xu W et al 2013 Pressure-induced hydrogen bond symmetrization in iron oxyhydroxide *Phys. Rev. Lett.* **111** 175501
- [7] Hanson A W 1960 The crystal structure of eosphorite *Acta Cryst.* **13** 384–7
- [8] Hoyos M A, Calderon T, Vergara I and Garcia-Solé J 1993 New structural and spectroscopic data for eosphorite *Mineral. Mag.* **57** 329–36
- [9] Gatta G D, Nenert G and Vignola P 2013 Coexisting hydroxyl groups and H_2O molecules in minerals: a single-crystal neutron diffraction study of eosphorite, $\text{MnAlPO}_4(\text{OH})_2 \cdot \text{H}_2\text{O}$ *Am. Mineral.* **98** 1297–301
- [10] Behal D, Röska B, Park S-H, Pedersen B, Benka G, Pfeleiderer C, Wakabayashi Y and Kimura T 2017 The first study of antiferromagnetic eosphorite-childrenite series ($\text{Mn}_{1-x}\text{Fe}_x$) $\text{AlPO}_4(\text{OH})_2\text{H}_2\text{O}$ ($x = 0.5$) *J. Magn. Magn. Mater.* **428** 17–27
- [11] Bireckoven B and Wittig J 1988 A diamond anvil cell for the investigation of superconductivity under pressures of up to 50 GPa: Pb as a low temperature manometer *J. Phys. E* **21** 841–8
- [12] Frost R L, Xi Y, Scholz R, López A, Lima R M F and Ferreira C M 2013 Vibrational spectroscopic characterization of the phosphate mineral series eosphorite-childrenite- (Mn,Fe) $\text{Al}(\text{PO}_4)(\text{OH})_2 \cdot (\text{H}_2\text{O})$ *Vib. Spectrosc.* **67** 14–21
- [13] Kao K C 2004 *Dielectric Phenomena in Solids* (Amsterdam: Elsevier) pp 41–114
- [14] Shannon R D and Prewitt C T 1969 Effective ionic radii in oxides and fluorides *Acta Crystallogr. B* **25** 925–46
- [15] Onoda-Yamamuro N, Yamamuro O, Matsuo T, Ichikawa M, Ibberson R M and David W I F 2000 Neutron diffraction study on hydrogen bond structure in $\text{K}_3\text{H}(\text{SeO}_4)_2$ and $\text{K}_3\text{D}(\text{SeO}_4)_2$ crystals *J. Phys.: Condens. Matter* **12** 8559–65
- [16] Kohno K, Matsuo T and Ichikawa M 1998 Tunneling effect in phase transitions of $\text{K}_3\text{H}(\text{SeO}_4)_2$ and its deuterated analogue *J. Korean Phys. Soc.* **32** 393–6
- [17] Endo M, Kaneko T, Osaka T and Makita Y 1983 Dielectric study of the phase transition in $\text{K}_3\text{H}(\text{SeO}_4)_2$ and isotope effect *J. Phys. Soc. JPN* **52** 3829–32
- [18] Moritomo Y, Tokura Y, Nagaosa N, Suzuki T and Kumagai K 1995 Role of the proton tunneling in the phase transition of $\text{K}_3\text{D}_{1-x}\text{H}_x(\text{SO}_4)_2$ *J. Low Temp. Phys.* **99** 55–70
- [19] Merunka D and Rakvin B 2009 Mechanism of quantum effects in hydrogen-bonded crystals of the $\text{K}_3\text{H}(\text{SO}_4)_2$ group *Phys. Rev. B* **79** 132108
- [20] Fillaux F and Cousson A 2012 Neutron scattering studies of $\text{K}_3\text{H}(\text{SO}_4)_2$ and $\text{K}_3\text{D}(\text{SO}_4)_2$: the particle-in-a-box model for the quantum phase transition *J. Chem. Phys.* **137** 74504

Supplementary 1 Real parts of permittivities ϵ_b' and ϵ_c' recorded with a single crystal of $\text{Mn}_{0.5}\text{Fe}_{0.5}\text{AlPO}_4(\text{OH})_2\text{H}_2\text{O}$ from 2 to 300 K with a rate of 2 K/min.



Supplementary 2 Loss tangents in the crystallographic a -direction measured from 2 to 300 K with a rate of 2 K/min.



14. Publication on rockbridgeite

IOP Publishing

Journal of Physics: Condensed Matter

J. Phys.: Condens. Matter **30** (2018) 235401 (12pp)

<https://doi.org/10.1088/1361-648X/aac0cd>

Determination of the hydrogen-bond network and the ferrimagnetic structure of a rockbridgeite-type compound, $\text{Fe}^{2+}\text{Fe}_{3,2}^{3+}(\text{Mn}^{2+}, \text{Zn})_{0.8}(\text{PO}_4)_3(\text{OH})_{4.2}(\text{HOH})_{0.8}$

B Röska¹, S-H Park^{1,6}, D Behal¹, K-U Hess², A Günther², G Benka³, C Pfeleiderer³, M Hoelzel⁴ and T Kimura⁵

¹ Department of Geo- and Environmental Sciences, Section of Crystallography, Ludwig-Maximilians-Universität München (LMU), Munich, Germany

² Department of Geo- and Environmental Sciences, Section of Mineralogy, Ludwig-Maximilians-Universität München (LMU), Munich, Germany

³ Department of Physics, Chair E21, Technische Universität München (TUM), Garching, Germany

⁴ Heinz Maier-Leibnitz Zentrum (MLZ), Technische Universität München (TUM), Garching, Germany

⁵ Department of Advanced Materials Science, University of Tokyo, 5-1-5 Kashiwanoha, Kashiwa, Chiba 277-8561, Japan

E-mail: sohyun.park@lmu.de

Received 29 January 2018, revised 26 April 2018

Accepted for publication 27 April 2018

Published 17 May 2018



Abstract

Applying neutron powder diffraction, four unique hydrogen positions were determined in a rockbridgeite-type compound, $\text{Fe}^{2+}\text{Fe}_{3,2}^{3+}(\text{Mn}^{2+}, \text{Zn})_{0.8}(\text{PO}_4)_3(\text{OH})_{4.2}(\text{HOH})_{0.8}$. Its honeycomb-like H-bond network running without interruption along the crystallographic a axis resembles those in alkali sulphatic and arsenatic oxyhydroxides. They provide the so-called dynamically disordered H-bond network over which protons are superconducting in a vehicle mechanism. This is indicated by dramatic increases of dielectric constant and loss factor at room temperature. The relevance of static and dynamic disorder of OH and HOH groups are explained in terms of a high number of structural defects at octahedral chains alternately half-occupied by Fe^{3+} cations. The structure is built up by unusual octahedral doublet, triplet, and quartet clusters of aliovalent $3d$ transition metal cations, predicting complicate magnetic ordering and interaction. The ferrimagnetic structure below the Curie temperature $T_C = 81\text{--}83$ K could be determined from the structure analysis with neutron diffraction data at 25 K.

Keywords: hydrogen-bond network, proton conductivity, ferrimagnetism, mixed valence iron, rockbridgeite, phosphatic oxyhydroxides

Supplementary material for this article is available [online](#)

(Some figures may appear in colour only in the online journal)

⁶ Author to whom any correspondence should be addressed.

1. Introduction

The rockbridgeite-type series with an idealized formula reported so far, $M^{2+}Fe_4^{3+}(PO_4)_3(OH)_5$ ($M = Fe, Mn, Zn$) belongs to the class of mixed-valence iron-bearing phosphatic oxyhydroxides [1–3]. This solid solution series occurs as opaque polycrystalline aggregates at several pegmatitic deposits as fibrous secondary hydrothermal alteration products of primary iron phosphates [1–6]. 3d transition metal (3d TM) oxyhydroxide compounds are of interest for diverse magnetic properties, as well as proton behaviours in differently configured hydrogen bonds which are the basis for potential applications as catalytic, energy, or sensor materials. For examples: barbosalite ($Fe^{2+}Fe_2^{3+}(PO_4)_2(OH)_2$) [7–9] and eosphorite-childrenite series ($(Fe^{2+}, Mn^{2+})AlPO_4(OH)H_2O$) [10] develop antiferromagnetic ordering at around 160 K and 7 K, respectively. The latter showed an anomalous dielectric response related to short hydrogen bonds (H-bond) sensible to application of pressure [11]. The lipscombite-type compounds, $Fe^{2+}Fe_2^{3+}(PO_4)_2(OH)_2$, undergo magnetic transitions between 60 K and 90 K and they are electrochemically active [12, 13]. Pt-doped synthetic analogues of rockbridgeite-type structures may be considered as catalysts for selective CO oxidation [14]. The rockbridgeite-type topology encloses narrow atomic sites for mixed-valence 3d TM, over which $Fe^{2+}-Fe^{3+}$ intervalence charge transfer occurs [15, 16], resembling other iron phosphatic oxyhydroxides, e.g. lazulite ($(Mg, Fe)Al_2(PO_4)_2(OH)_2$) and vivianite ($Fe_3^{2+}(PO_4)_2 \cdot 8H_2O$). A magnetic phase transition at 83 K in rockbridgeite was reported in [16], but details of the spin ordering is unknown up to date.

The structure of rockbridgeite-type series in the space group symmetry $Cmcm$ (#63) was first solved by Moore in 1970 without siting OH groups [1]. Their hydrogen positions were estimated exclusively by local charge deficits at oxygen sites from bond valence sum (BVS) calculations [1–3]. In a recent study, their possible locations were adumbrated in difference Fourier (ΔF) maps evaluated with x-ray diffraction data [2]. Hence, the use of neutron single crystal diffraction (NSCD) techniques is more meaningful to accurately determine O, OH, and HOH groups. Unfortunately, it is nearly impossible to obtain high-quality single crystals of rockbridgeite large enough for NSCD. In the present study, we employed high-resolution neutron powder diffraction (HRNPD) and could identify four unique hydrogen positions for the first time. Of particular interest is the presence of a H-bond network in this interesting oxyhydroxide compound. Its configuration meets the desired condition for superprotonic conductivity. Static and dynamic disorder of OH and HOH groups in rockbridgeite-type compounds are explained in terms of a high abundance in defective sites for unusual octahedral clusters of aliovalent 3d TM cations. Their magnetic spins show a ferrimagnetic order below $T_c = 81-83$ K, as delivered from the structure analysis with HRNPD data at 25 K.

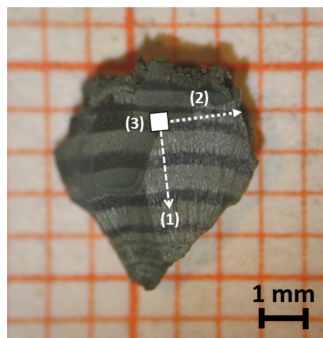


Figure 1. Typical polycrystalline specimen with strong pleochroism perpendicular to druse-like arranged fibrous crystallites. Direction marks indicate sample orientations used in magnetometric and dielectric response measurements: (1) preferably along crystal fibres, i.e. the crystallographic c axis, (2) in-plane and (3) out-of-plane direction mostly perpendicular to crystal fibre axes.

2. Experimental

2.1. Sampling

Polycrystalline sample masses from Hagendorf Süd, Germany, were provided by the *Museum Bayerische Staatssammlung München*. Large grains of quartz and further limited quantities of unidentified reddish impurities were carefully extracted from the crushed sample batch under an incident beam microscope. The rockbridgeite-type mineral sample comprises spherically arranged fibrous crystals conglomerating to druse-like entities (figure 1). Fibres grow parallel to the crystallographic c axis [3–5]. A strong pleochroism alternating from dark grey to olive-green is visible perpendicular to the elongated crystals. Crystals smaller than about $150 \times 150 \times 150 \mu m^3$ were selected for x-ray single crystal diffraction (XSD). A batch of platy crystal masses (about $5 \times 5 \times 1 mm^3$) was taken for phase analysis via x-ray powder diffraction (XPD) and to conduct all characterisation methods applied in this study. From the same batch 8 g of fine powder were saved for conducting variable temperature HRNPD.

2.2. X-ray powder diffraction

XPD was conducted on a *XRD3001* diffractometer (*GE*) in Bragg–Brentano geometry equipped with a semiconductor position sensitive linear detector (*Meteor1D*) using $Cu K_{\alpha 1}$ ($Ge(111)$ monochromator). Data sets acquired three times in a 2θ -range of $8^\circ-140^\circ$ with a scan step of 0.013° were added up to increase counting statistics. A LaB_6 standard (660d, NIST) was mixed to the sample powder to accurately determine the lattice parameters at room temperature (RT) by Rietveld refinements using the program package *FullProf* [17].

2.3. Chemical and thermal analysis

Chemical compositions were determined by electron probe micro analysis (EPMA) at 15 kV and 10 nA (*Cameca SX100*).

The specimens were embedded in resin and carbon coated to allow electric conductivity. Line scans consisting of 450 independent spots were measured on sample fragments. Energy-dispersive x-ray spectra were analysed first to probe constituent elements to be measured subsequently with angle-dispersive x-ray spectroscopy. Concentrations of Mn, Fe, P, and Ca were evaluated with respect to the standards ilmenite, Fe₂O₃, apatite, and wollastonite, respectively.

A sample of 10 mg was heated from 298 K up to 1073 K at a rate of 10 K min⁻¹ in Ar atmosphere using a thermomicrobalance, *Netsch Sta 449C* to simultaneously conduct differential scanning calorimetry (DSC) and thermogravimetric analysis (TG). Heat capacity between 2 K and 300 K was recorded via the short pulse method within a physical properties measurement system (PPMS) from *Quantum Design*.

2.4. Spectroscopy

⁵⁷Fe Mössbauer spectra were acquired at RT in transmission mode on a constant acceleration Mössbauer spectrometer. Hyperfine parameters were determined from a full Hamiltonian site analysis using software *Recoil*.

Fourier-transform infrared spectroscopy (FTIR) spectra were obtained from 1 mg of powder mixed and pressed with anhydrous KBr. Sixty-four scans at the resolution of 4 cm⁻¹ were acquired between 360 cm⁻¹ and 4000 cm⁻¹ on an *EQUINOX55 Spectrometer (Bruker)*. The spectrum was subsequently corrected for absorptions related to the CO₂ inert gas atmosphere.

The real and imaginary part of the permittivity at 1 kHz was recorded at 1 V with an *Agilent E4980* LCR meter while heating the sample with 5 K min⁻¹ from 2 K to 400 K within a PPMS. Silver electrodes were vacuum-evaporated on the polycrystalline plates of 100 μm in thickness perpendicular to the crystal fibre axes, i.e. ⊥ [001].

2.5. Magnetic characterisation

AC magnetic susceptibility (χ_{AC}) data were acquired in the temperature range 2–350 K in a PPMS at the excitation frequency and amplitude of 1 kHz and 10 mT, respectively. Zero-field-cooled magnetisation was evaluated with a magnetic properties measurement system (MPMS, *Quantum Design*) in vibrating sample mode between 8 K and 300 K applying a field of 10 mT. As illustrated in figure 1, magnetic properties were evaluated along three directions of platy shaped specimen: in-plane direction predominantly measured along crystal fibre axes, i.e. the crystallographic *c* axis (1); preferably perpendicular to *c* axis in-plane (2) and out-of-plane (3).

2.6. X-ray single crystal diffraction

XSD was performed at 298 K on a κ -four-circle single crystal diffractometer (*Gemini-A-Ultra*) equipped with a charge-coupled detector (*Atlas*), provided by *Rigaku Oxford Technologies*. A crystal of 80 × 80 × 120 μm³ in size was attached to a glass fibre and mounted onto a goniometer head

positioned at 60 mm from the detector. Using Mo *K*_{α1} radiation (graphite(002) monochromator) the full reciprocal space was scanned in 2D frames with a step size of $\phi = 0.5^\circ$ up to the resolution $d = 0.58 \text{ \AA}$. Data reduction including numerical absorption correction [18] was made in the data reduction process using the software *CrysAlis (Agilent)*. Structure solution was performed by the Superflip method [19], followed by structure refinements by the least-square algorithm in ΔF syntheses, and searching for residual electron densities using the program package, *Jana2006* [20]. Experimental parameters and results from data reduction are shown in supplementary 1 (stacks.iop.org/JPhysCM/30/235401/mmedia).

2.7. High-resolution neutron powder diffraction

HRNPD data collection was carried out with a constant wavelength of 1.5483 Å using a Ge(551) monochromator at the instrument SPODI at FRM II, Garching, Germany [21]. The powder sample was packed in a vanadium can in a closed cycle He refrigerator. For the data collection above RT a niobium sample can was used with a vacuum high-temperature oven. Data sets were collected by 80 vertically position-sensitive detectors with 300 mm-high collimators in a 2θ -range of 8°–160° with a step width of 0.05° at 25 K, 298 K, and 493 K. Using *Jana2006* Rietveld calculations for the nuclear and magnetic structures were conducted.

The HRNPD pattern acquired at 298 K exhibit extremely high background mainly due to inelastic scattering from protons in OH groups. As aforementioned, the presence of nano-crystalline impurity phases at the 2θ -region 16.8°–18.0°, was disregarded in the refinements because the rockbridgeite structure does not exhibit Bragg reflections in this range. For the problem with fitting background parameters, atomic displacements were treated isotropically.

3. Results and discussion

3.1. Phase identification

LeBail fitting with XPD data (supplementary 2) of our sample confirmed the rockbridgeite-type structure in the space group *Cmcm* [1–3] with the refined cell parameters $a = 5.1772(1) \text{ \AA}$, $b = 13.9828(1) \text{ \AA}$, and $c = 16.8647(4) \text{ \AA}$. EPMA line scans resulted in a homogeneous chemical composition. Based on the total of 17 O per formula unit (*pfu*), the ratio of cationic constituents was calculated: Fe: Mn: Zn: P = 4.24(4): 0.58(3): 0.18(3): 3.1(1). A trace of about 0.05(1) Ca was often observed in rockbridgeite samples [1–3, 5, 15] but is not considered as its structure constituent due to its size is too large at atomic sites for Fe^{2+/3+}.

3.2. Thermal behaviours

A strong endothermal peak about 600 K with the first weight loss in TG/DSC curves (figure 2) points to the onset of decomposition. Further stepwise discontinuities in TG correspond to the sequential weight loss of 8.1 wt% up to 850 K. An

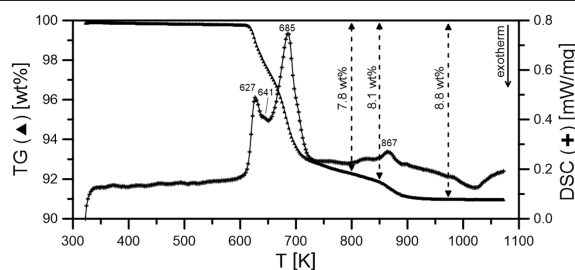


Figure 2. TG/DSC between 325 K and 1080 K reveal dehydration and decomposition between 600 K and 850 K accompanied by a weight loss of 8.1 wt%.

additional weight loss of 0.7 wt% above 850 K was detected. The broad exothermic hump centred at 1022 K could be addressed to recrystallisation processes. Indeed, XPD pattern of the sample obtained after the TGA/DSC analysis exhibited a variety of iron phosphates: $\text{Fe}_2\text{P}_2\text{O}_7$, $\text{Fe}_{1.5}\text{Mn}_{1.5}\text{P}_2\text{O}_8$, Fe_2O_3 , ZnP_2O_6 , and ZnMn_2O_4 . In the 493 K HRNPD data, there were reflections from lipscombite-type compound ($\text{Fe}^{2+}\text{Fe}_2^{3+}(\text{PO}_4)_2(\text{OH})_2$) and several minor compounds only. This phase transition/recrystallization temperature (493 K) observed under high vacuum is much lower than the decomposition point starting above 600 K observed in TGA/DSC under Ar atmosphere. In fact, the 493 K HRNPD pattern exhibited much lower background compared to that at 298 K for the reduced amount of OH-groups in the batch sample.

3.3. Crystal structure at 298 K

The XSD data showed typical patterns from two individual single crystals with the same lattice metrics of $5.127(1) \times 13.971(2) \times 16.845(2) \text{ \AA}^3$ in Cmcm . As shown in reconstructed reciprocal layers (figure 3), these two crystals are intergrown around the b axis only with a small misfit of 1° . Reflections integrated only for the crystal with the higher volume fraction (68 vol%) showed an internal consistency value of $R_{\text{int}} = 5.8\%$ and an average redundancy of 8.1 (supplementary 1).

The structure solution immediately suggested all sites for cations and eight oxygens. Three $3d$ TM atoms sites are octahedrally coordinated, Fe1, Fe2 and the half-occupied Fe3 site. Like Fe3, the O3 site is 50% occupied while all oxygen sites are fully occupied (figure 4). The Fe1 and Fe2 sites are present in a triplet of face-sharing octahedra cluster, $[\text{Fe}_2\text{O}_6]-[\text{Fe}_1\text{O}_6]-[\text{Fe}_2\text{O}_6]$ (figure 4(a)). These so-called h -clusters [1] are connected to each other via edges of the strongly distorted outer $[\text{Fe}_2\text{O}_6]$ octahedra to build infinite zigzag-like chains along the c -direction. Along a , h -clusters are connected by a quartet of half-occupied $[\text{Fe}_3\text{O}_6]$ octahedra (figure 5(a)). Over O3, two $[\text{Fe}_3\text{O}_6]$ octahedra are linked to each other cornerwisely (figures 6 and 5(b)). These major units are stabilized by connecting with rigid PO_4 tetrahedra at the sites P1 and P2 to form a 3D mixed tetrahedral–octahedral (TO) network.

According to [1, 2] and our Mössbauer spectra, as discussed below, Mn and Zn were sited exclusively at Fe2 in

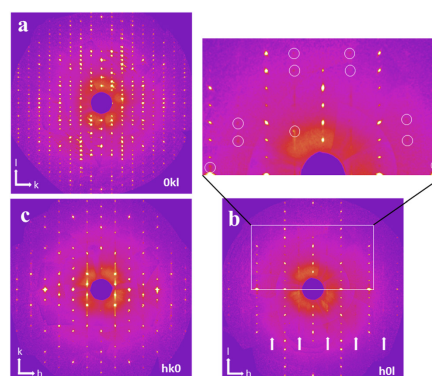


Figure 3. Reciprocal lattice planes of XSD data. (a) $0kl$ layer indicates the presence of two individual single crystals. (b) $h0l$ layer reveals diffuse streaks along l -direction at $h = \text{odd}$. Weak reflections forbidden to Cmcm are highlighted within circles. (c) hko layer shows intense diffuse scattering in k -direction at $h = \text{odd}$.

the model refinement, and their occupancies were fixed to the respective values obtained from chemical analysis. All atomic parameters (supplementary 3) including anisotropic thermal displacement parameters (ADPs) (supplementary 4) were refined to be used as a starting model for subsequent refinements with HRNPD data.

The short mean oxygen bonding lengths to Fe1 and Fe3 sites, i.e. $d(\text{Fe1-O}) = 2.017(6) \text{ \AA}$ and $d(\text{Fe3-O}) = 2.022(14) \text{ \AA}$ (table 1), indicate Fe^{3+} preferably present at Fe1 and Fe3. The longer bonding length $d(\text{Fe2-O}) = 2.117(9) \text{ \AA}$ indicates preference to Fe^{2+} [22]. This assignment is in accordance with Mössbauer spectral bands with five Lorentzian doublets (figure 7), similar to observations in [2]: two absorption doublets with large values of quadrupole splitting (QS) and isomer shift (IS) are assigned to octahedrally coordinated Fe^{2+} cations; three doublets with smaller QS and IS values are attributed to six-fold coordinated Fe^{3+} species. As summarized in table 2, the total of 4.24 Fe pfu comprises of 1.02(2) Fe^{2+} and 3.23(5) Fe^{3+} . The Fe^{3+} doublets with the area fractions of 1.02(1) and 2.03(2) Fe^{3+} atoms pfu are fitting well

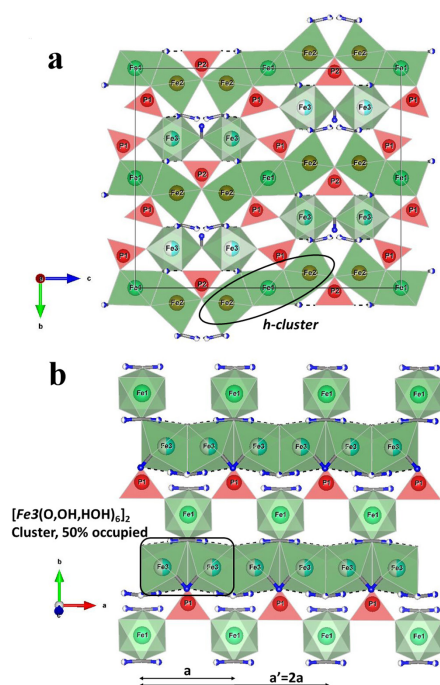


Figure 4. The rockbridgeite-type TO framework topology with $[\text{FeO}_6]$ (green) and $[\text{PO}_4]$ (red) entities and H-sites forming OH and HOH groups (blue/white). $\text{Fe}_2\text{-Fe}_1\text{-Fe}_2$ octahedra are connected via faces to form *h-clusters* being edge-linked to form infinite chains in $[001]$ (a). *h-clusters* linked to each other via alternately occupied Fe_3 octahedral doublets in $[100]$, giving rise to superposition with doubled a cell parameter (b). Oxygens are omitted for clarity.

to the respective ideal occupation values at Fe1 and Fe3. The larger Fe^{3+} doublet possesses a smaller QS value, i.e. the less distorted character of $[\text{Fe}_3\text{O}_6]$ octahedron, compared to $[\text{Fe}_1\text{O}_6]$ (table 1). The two Fe^{2+} type doublets are assigned to the Fe2 site holding an additional amount of 0.17(1) Fe^{3+} *pfu* equal to the area of the smallest Fe^{3+} type doublet. The increased IS at Fe2 with respect to the other Fe^{3+} -type doublets is explained by the larger oxygen bonding distances at Fe2. Adding up the residual $3d$ TM cations (0.58(3) Mn and 0.18(3) Zn), the Fe2 site has about 1.93 atoms *pfu*, near to the expected value 2. Hence, the association of two Fe^{2+} doublets to Fe2 can be understood further by interactions between next nearest neighbour cations, e.g. in two edge-sharing $[\text{Fe}_2\text{O}_6]$ octahedra belonging to two adjacent *h-clusters* (figure 4). There might be various local electronic and coordinative environments for neighbouring Fe^{2+} cations in $\text{Fe}^{2+}\text{-Fe}^{3+}$, $\text{Fe}^{2+}\text{-Mn}^{2+}$, $\text{Fe}^{2+}\text{-Zn}^{2+}$ pairs. The two clearly resolved Fe^{2+} doublets at Fe2 are probably due to the abundant $\text{Fe}^{2+}\text{-Fe}^{2+}$ and $\text{Fe}^{2+}\text{-Mn}^{2+}$ pairs. In summary, the both sites Fe1 and Fe3

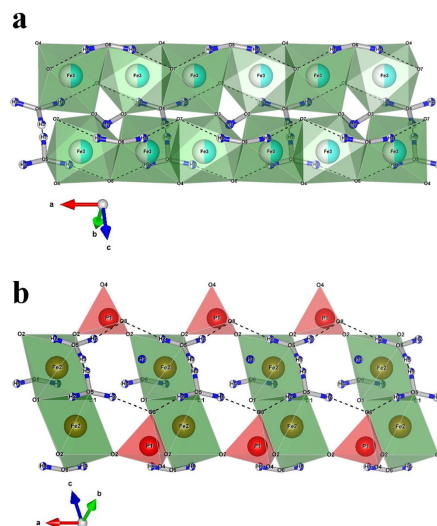


Figure 5. A honeycomb-like H-bond network (dashed line) of the title compound runs through the top (a) and bottom (b) of half-occupied $[\text{Fe}_3\text{O}_6]$ octahedral chains.

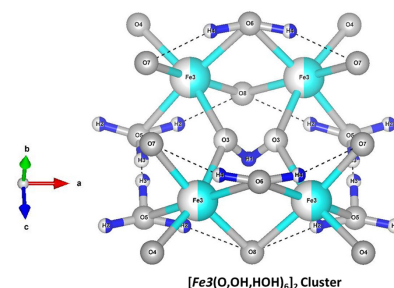


Figure 6. H-bond configuration around a quartet of half-occupied $[\text{Fe}_3(\text{O,OH,HOH})_6]$ octahedra.

are occupied exclusively by Fe^{3+} while Fe2 contains $\text{Fe}^{2+}/\text{Fe}^{3+}$ as well as Mn^{2+} and Zn.

Based on the starting model obtained from the XSD analysis, the nuclear structure was further refined with the HRNPD pattern acquired at 298 K to find hydrogen atoms (figure 8). The lattice metrics were fixed to the values accurately determined by the XPD analysis. In subsequent ΔF calculations, four negative density maxima of neutron coherent scattering length (*Coh b* for H = -3.739 fm) were resolved clearly near O3, O5, and O6. As predicted by BVS calculations [1–3], they were assigned to four H sites H1, H2, H3, and H4 (figure 6). The occupancy parameters (OCC) refined for four H sites gave rise to the value 5.88 H *pfu*. Considering the site multiplicity, the special site H1 with a

Table 1. Distortion parameters of octahedral units obtained from HRNPD at 298 K indicate strong distortion of the [Fe2O₆] octahedron in comparison to the more regular [Fe1O₆] and [Fe3O₆] octahedra. BLD = Bond-length distortion, ELD = edge-length distortion [23]; OAV = octahedral angle variance, OQE = octahedral quadratic elongation [24].

Octahedral sites	Fe1	Fe2	Fe3
d(Fe–O) (Å)	2.017(6)	2.117(9)	2.022(14)
d(O–O) (Å)	2.85	2.88	2.86
Volume (Å ³)	10.68	12.15	10.87
BLD (%)	1.63	1.52	1.55
ELD (%)	6.38	8.09	3.83
OAV (°)	58.35	103.67	33.54
OQE	1.0159	1.0279	1.0099

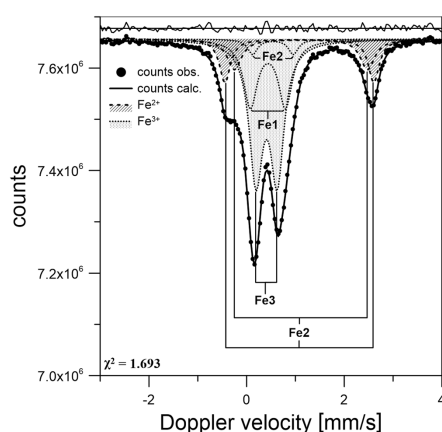


Figure 7. Mössbauer spectrum fitted with three narrow quadrupole splittings typical for octahedrally coordinated Fe³⁺ species and two broader doublets characteristic for Fe²⁺ in octahedral coordination. Difference between observed and calculated counts is plotted on top of the base line.

full occupation gives one H atom *pfu*, bonded to either O3 split site to form a static disordered OH group (figure 6). The general sites H2 and H4 are half occupied, each giving rise to two H atoms *pfu*. These build OH groups with oxygens at O5 and O6, respectively, along the skirt at O–O edges of empty [Fe3O₆] octahedra, i.e. only when Fe3 sites are unoccupied (figures 4(b) and 6). The split sites H2 and H3 are available for mutually exclusive occupation by H to build a HOH group (figure 6). Two adjacent H3 split sites with a low OCC of 0.22 are situated between two O5 sites only in a short distance, d(H3–H3) = 0.64 Å. The inclusion of H atoms at the site H3 significantly improved the structure refinements. The structure parameters refined with 298 K HRNPD data are given in table 3. A list of interatomic distances and angles are listed in supplementary 5.

The refined occupancy at H3 (about 0.88 hydrogen atoms *pfu*) matches fairly well to the lack of positive charge

Table 2. Hyperfine parameters at 298 K evaluated by fitting Mössbauer spectrum, based on 4.24 Fe *pfu*.

IS (mm s ⁻¹)	QS (mm s ⁻¹)	Γ (mm s ⁻¹)	Area (%)	Fe oxidation state and content <i>pfu</i>
0.408(7)	0.436(2)	0.167(4)	47.98	Fe ³⁺ : 2.03(2)
0.436(3)	0.719(1)	0.170(2)	24.11	Fe ³⁺ : 1.02(1)
0.539(9)	0.832(5)	0.120(2)	3.90	Fe ³⁺ : 0.17(1)
1.080(3)	3.049(4)	0.133(7)	12.44	Fe ²⁺ : 0.53(1)
1.112(7)	2.725(4)	0.178(2)	11.57	Fe ²⁺ : 0.49(1)

(–0.8 e *pfu*) by the selective substitution of Fe³⁺ by Mn²⁺ and Zn at Fe2. The octahedral moieties in rockbridgeite-type structures might be expressed correctly by [Fe1(O,OH)₆], [Fe2(O,OH,HOH)₆], and [Fe3(O,OH,HOH)₆] (figure 5). The determined H2–O5–H3 ligand requires revision on the mineral formula M²⁺Fe³⁺(PO₄)₃(OH)₅ (M = Fe, Mn, Zn). With the refined OCC at H3 compensating for the amount of Mn²⁺ and Zn replacing Fe³⁺ at Fe2 and the resulting charge deficit, we suggest the idealised formula for the title compound Fe²⁺Fe³⁺₂(Mn²⁺, Zn)_{0.8}(PO₄)₃(OH)_{4.2}(HOH)_{0.8}. The resulting content of about 2.9 H₂O corresponds the weight loss 7.76 wt% reached at the endothermic peak around 800 K in TGA (figure 2). Therefore, the additional endothermic peak above this temperature may be addressed to the impurity origin.

3.4. Structural disorder

The half-occupied Fe3 sites within a face-shared [Fe3(O,OH,HOH)₆]₂ cluster (figures 4(a) and 6) are spaced in a close distance of 2.35 Å. From the aspect of structural stability it is reasonable to have an alternating sequence of occupied and non-occupied [Fe3(O,OH,HOH)₆]₂ cluster chains along the *a* direction. These chains are connected in *c* direction to each other by common corners at one of two half-occupied O3 split sites (figure 5(a)). Thus, this arrangement creates double octahedral caverns within a quartet of [Fe3(O,OH,HOH)₆] octahedra. Indeed, as shown in figure 3(b), weak diffuse streaks were observed in *l* direction on *h0l* when *h* = odd, which are forbidden to the space group *Cmcm*. Such weak diffuse streaks were seen also along *k* in *hk0* (figure 3(c)). These XSD patterns strongly point to structural defects formed coherently in the main direction *a* to have a correlation length of |*a'*| = 2 |*a*|. This might be related to the half occupation of Fe³⁺ in the face-sharing [Fe3(O,OH,HOH)₆]₂ cluster-chains, showing long-range disorder parallel to the *a* axis.

On the other hand, there are forbidden reflections on *h0l* with *h*, *l* = odd showing extremely weak but well-confined intensities, as highlighted within circles in figure 3(b). But for *hk0* reflections, the reflection condition *h* + *k* = even was satisfied, and they are much stronger than those forbidden reflections in *h0l* layer. Therefore, we regraded XSD patterns from two intergrown polymorphs: Type **A** as the main phase in *Cmcm* and Type **B** in *Pmnm*. This means that Type **A** and **B** commonly contribute to *h0l* reflections with *h*, *l* = even; *h00*

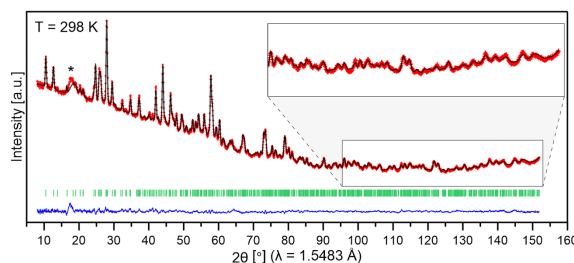


Figure 8. Graphic presentation of Rietveld calculation (black line) with observed (+) HRNPD pattern at 298 K. Short bars indicate the positions of rockbridgeite reflections. The flat difference profile between observed and calculated intensities plotted at the bottom is in accord with the low residual values: GOF (goodness of fit) = 2.52; wRp (weighted profile residual value) = 1.26; wR2 (weighted residual between the observed and calculated HRNPD for all nuclear reflections in the refinement against intensity) = 5.99% (* impurity).

Table 3. Atomic parameters with isotropic ADPs (U_{iso} (Å²)) and occupancy parameters (OCC) at 298 K and 25 K from structure refinements with HRNPD data.

Site	Atom type	OCC	298 K				25 K			
			x	y	z	U_{iso}	x	y	z	U_{iso}
Fe1	Fe	1	0	0	0	0.023(1)	0	0	0	0.037(1)
Fe2	Fe	0.62	0	0.0683(6)	0.1564(4)	0.035(2)	0	0.0706(5)	0.1544(3)	0.033(1)
	Mn	0.295								
	Zn	0.095								
Fe3	Fe	0.5	0.2304(10)	0.3206(4)	0.1372(2)	0.018(1)	0.2319(10)	0.3199(4)	0.1376(3)	0.024(1)
P1	P	1	0.5	0.1457(5)	0.0449(5)	0.027(2)	0.5	0.1453(5)	0.0428(4)	0.025(1)
P2	P	1	0	0.4846(9)	0.25	0.037(3)	0	0.4852(6)	0.25	0.025(2)
O1	O	1	0.2377(15)	0.5509(4)	0.25	0.034(2)	0.2412(13)	0.5502(4)	0.25	0.026(1)
O2	O	1	0.2535(9)	0.0815(3)	0.0576(2)	0.023(1)	0.2595(7)	0.0829(2)	0.0575(2)	0.022(1)
O3	O	0.5	0.3807(17)	0.3171(10)	0.25	0.017(2)	0.3752(16)	0.3144(9)	0.25	0.022(2)
O4	O	1	0.5	0.1782(5)	0.9588(3)	0.022(1)	0.5	0.1797(4)	0.9574	0.030(1)
O5	O	1	0	0.2139(5)	0.1749(4)	0.039(2)	0	0.2149(4)	0.1744(3)	0.032(1)
O6	O	1	0.5	0.4241(5)	0.1051(4)	0.025(1)	0.5	0.4232(5)	0.1049(4)	0.034(1)
O7	O	1	0	0.4212(5)	0.1757(3)	0.016(1)	0	0.4223(4)	0.1751(3)	0.018(1)
O8	O	1	0.5	0.2244(4)	0.1046(4)	0.021(1)	0.5	0.2243(3)	0.1051(1)	0.020(1)
H1	H	1	0.5	0.2639(18)	0.25	0.142(13)	0.5	0.2629(16)	0.25	0.093(7)
H2	H	0.5	0.3147(18)	0.2815(13)	0.8430(10)	0.051(4)	0.3019(12)	0.2776(9)	0.8489(7)	0.037(3)
H3	H	0.22	0	0.2307(13)	0.2310(10)	0.033(6)	0	0.2266(16)	0.25	0.081(7)
H4	H	0.5	0.6873(34)	0.4229(34)	0.1177(21)	0.162(14)	0.3161(19)	0.4068(19)	0.1146(14)	0.119(9)

with $h = \text{even}$; $0k0$ with $k = \text{even}$. The main reflections hkl with $h + k = \text{even}$ of Type **A** are contributed also to Type **B** when $h, l = \text{even}$. The $h0l$ reflections with $h, l = \text{odd}$ are originated solely from Type **B**. For their limited number and weak intensities, neither of their distribution functions nor the type of intergrowth could be delivered in this study. The presence of those weak forbidden reflections and diffuse streaks could not be resolved in HRNPD data with high background, as previously mentioned. For the same reason, however, a relevant conclusion could be drawn such that the long-range order of the main phase Type **A** is disturbed by a point defect-like occurrence of Type **B**. This structure defect is 2D in the $(b-c)$ plane, as diffuse streaks run in k and l , meaning the presence of 2D stacking faults $\perp a$. In turn, this defective structure is a highly interesting object in terms of the H-bond network as a basis for super protonic conductivity, described in the following sections.

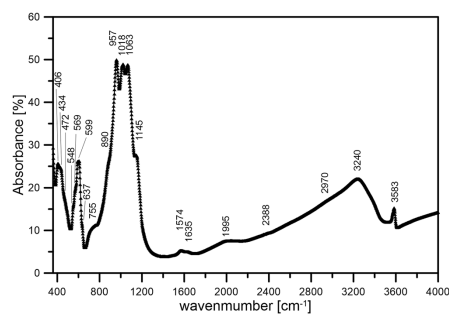
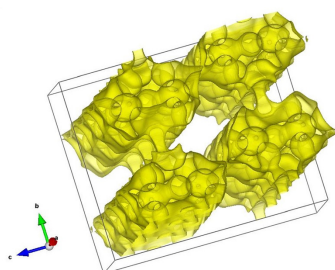


Figure 9. FTIR spectrum showing typical HOH modes indicated by absorption bands at 3482 cm⁻¹, 3240–2200 cm⁻¹, as well as 1635 cm⁻¹, and 1574 cm⁻¹ (table 4).

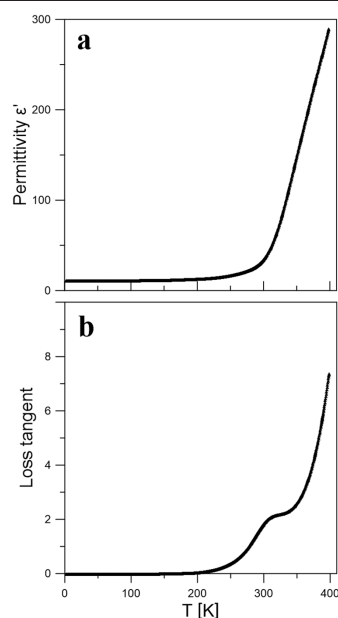
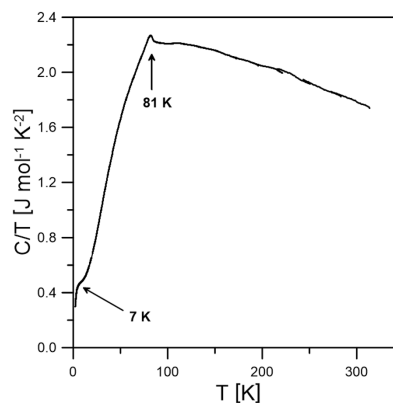
Table 4. Assignment of FTIR spectrum in figure 9.

Absorption bands (cm ⁻¹)	Assignments
3482, 3240–2200	O–H / HOH stretching vibration
2970, 2388, 1995	O–H...O–P modes (strong H-bonds)
1635, 1574	HOH bending vibration
1145, 1063, 1018, 957, 890	PO ₄ ³⁻ stretching vibration
755, 637	HOH librational vibration under H-bond formation
599, 569, 549	PO ₄ ³⁻ bending vibration
472, 434, 406	mixed lattice modes involving MO ₆ -octahedra

**Figure 10.** BV energy landscape along the *a* axis showing statistic pathways for conducting H⁺, marked in yellow with an isosurface at $V_{\text{pot},E} = -1.2$ eV. Along these pathways running via the H-bond network mobile H⁺ would retain its optimal BV in the title compound.

3.5. The H-bond network and dielectric anomaly

The hydrogen sites H1, H2, H3 and H4 form OH and HOH groups with oxygens at O3, O5 and O6 (figure 5). The fully occupied H1 site forms identical bonding distances to either the half occupied O3 split site. H atoms at H2 and H4 split sites reside at the edge of octahedral voids of Fe3 to build strong H-bonds: H2 is involved in an almost linear hydrogen bridge O5–H2...O8 ($d(\text{O}–\text{O}) = 2.851(4)$ Å; $\angle(\text{O}–\text{H}–\text{O}) = 169(2)^\circ$). H4 reaches more into the octahedral void under the formation of the H-bond O6–H4...O7 ($d(\text{O}–\text{O}) = 2.849(4)$ Å; $\angle(\text{O}–\text{H}–\text{O}) = 161(3)^\circ$). H atoms at H3 are attached to the O5–H2 group to form HOH groups, i.e. O5 is surrounded by two statically disordered H2 split sites and one H3. This unusual steering wheel-like triangle about O5 with $\angle(\text{O}–\text{H}–\text{O}) = 106(1)^\circ$ is a result of static disorder of H (figure 6). Thus, in the rockbridgeite-type structure, the H-bond O5–H3...O5 ($d(\text{O}–\text{O}) = 2.533(10)$ Å; $\angle(\text{O}–\text{H}–\text{O}) = 158(2)^\circ$) represents the shortest and strongest one over the statically disordered H atoms at the short H3 split sites. The presence of such strongly bonded OHO groups reflected by their bending and librational vibrations modes allows build up a 2D H-network in the (*a*-*c*) plane, as demonstrated with dashed black lines in figures 4 and 6. An indication of strong hydrogen bonds involving HOH-groups is proven in FTIR due to the broad vibration

**Figure 11.** Dielectric response measured in the sample orientation (3) in figure 1, displays a dramatic increase of real and imaginary parts of the dielectric permittivity around RT.**Figure 12.** Temperature derivative of heat capacity between 2 K and 300 K reveals two anomalies at about 81 K and 7 K.

bands at 755 cm⁻¹ and the shoulder at 637 cm⁻¹ (figure 9). In particular, the bands at 1635 and 1574 cm⁻¹ clearly evidence the presence of HOH groups. In addition, broad signals at 1995, 2388, and 2970 cm⁻¹ can be related to vibrations

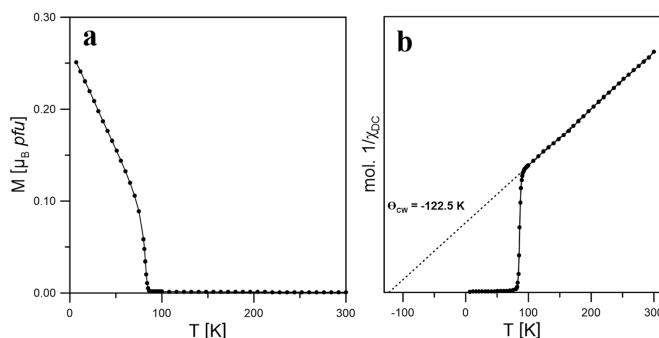


Figure 13. Magnetisation between 8 K and 300 K acquired preferably in the sample orientation (1) in figure 1, show a spontaneous increase in magnetisation below 83 K (a). The derived inverse molar susceptibility indicates a ferrimagnetic behaviour with $\theta_{\text{CW}} < 0$ K (b).

in local units of O–H...O–P associated with strong hydrogen bonds. As summarized in table 4, the FTIR absorption bands in figure 9 could be assigned to O–H stretching and bending vibration modes of OH anions, HOH, PO_4^{3-} anions [3, 25, 26]. These H-bonds play an important role for compensating the decrease in the framework stability due to vacancies in $[\text{Fe}_3(\text{O},\text{OH},\text{HOH})_6]_2$ cluster chains. Recall the dehydration of the title compound starting first around 600 K under argon. This reflects a high strength of H-bonds and their contribution to the structural stability.

As illustrated in figure 5, the determined OH or HOH groups build up a honeycomb-like H-bond network extending without interruption exclusively in the \mathbf{a} direction. This H-bond network is a highly exciting subject as resembling those in a few alkali sulphatic and arsenatic oxyhydroxides [27]. They provide the so-called dynamically disordered H-bond network over which protons are superconducting in a vehicle mechanism: new H-bonds are continuously created and faded in the network of asymmetric O–H...O bonds through correlated reorientation or thermal motions of the TO framework. Static disorder of H atoms in H-bonds over narrow split sites and vacancies present at the sites of $3d$ TM moieties can motorize vehicle-like fast motion of H^+ . In this aspect, this structure type exhibits a framework typical for superprotonic conductors. The possible pathways for conducting H^+ correspond to honeycomb-like cylinders of potential energy isosurface running in \mathbf{a} , as evaluated with BVS mismatch map of H^+ (figure 10). On such an isosurface of potential energy landscape, H^+ would move fast to find its optimal bond valence [28]. H-bonds are highly polarizable and susceptible to stimulated ion hopping through the application of (alternating) electric fields E_{AC} in the kHz range [29]. The fast charge transfer in the title compound could be proven by dielectric response $\perp [001]$ (figure 11) as the real part of dielectric permittivity and the loss factor dramatically increase above 300 K. The loss factor curve indicates at least two relaxation processes of fast charge transfers. The relaxation process in the low temperature range of 250 K–300 K may be attributed to fast local motion of H^+ over the split

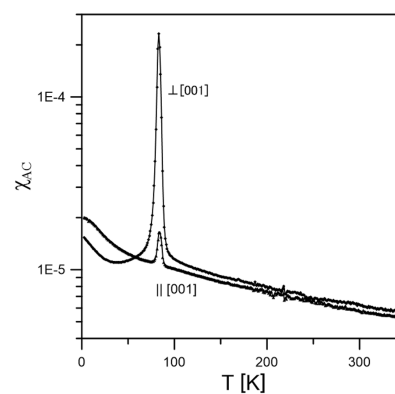


Figure 14. Magnetic AC-susceptibility between 2 K and 350 K recorded roughly parallel and perpendicular to the \mathbf{c} axis show anomalies at 83 K.

sites H3 in a short distance of 0.64 \AA . The steep increase in dielectric loss from 300 K points to the H^+ conductivity over the entire H-bond network.

3.6. Magnetic phase transition

Figure 12 presents the temperature derivative of the heat capacity curve ($C/\delta T$) as a function of temperature in the range of 2 K–300 K. Two anomalies are clearly seen near 7 K and 81 K. The latter is attributed to the magnetic phase transition reported in [16]. In fact, our magnetisation data taken preferably along \mathbf{c} axis, showed a spontaneous and steadily increasing magnetisation below $T_{\text{C}} = 83$ K. No magnetic saturation appeared up to the lowest measuring temperature 8 K with a relatively low magnetisation value of about $0.25 \mu_{\text{B}} \text{ pfu}$ from the polycrystalline sample (figure 13(a)). The derived molar χ^{-1} curve follows Curie–Weiss behaviour

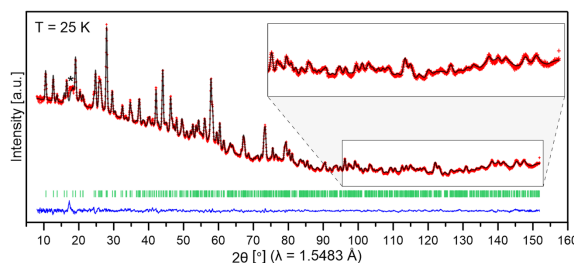


Figure 15. Results from combined Rietveld refinements of nuclear and magnetic structures with HRNPD data at 25 K in SG $Cm'c'm$, allowing a ferrimagnetic order with net magnetisation in $[001]$ ($k = (0, 0, 0)$). GOF = 2.26; wRp = 1.15; wR2 = 4.87% (* unidentified impurity).

Table 5. Magnetic space groups eligible for the propagation vector $k = (0,0,0)$ as subgroups of the nuclear space group $Cmcm$.

Magnetic space group	Magnetic order	Net magnetisation
$Cmcm$	AFM	—
$Cm'c'm'$	AFM	—
$Cm'cm$	AFM	—
$Cmc'm$	AFM	—
$Cmcm'$	AFM	—
$Cmc'm'$	FM	parallel $[100]$
$Cm'cm'$	FM	parallel $[010]$
$Cm'c'm$	FM	parallel $[001]$

between 100 K and 300 K. The negative Curie–Weiss temperature of $\theta_{CW} = -122.5$ K is typical for a paramagnetic to ferrimagnetic transition (figure 13(b)). AC susceptibility measurements confirmed a magnetic phase transition at $T_C = 83$ K, where peak value acquired roughly $\parallel [001]$ is lower than that of $\perp [001]$ (figure 14). Following the χ_{AC} curve towards the low temperature limit below about 50 K, the susceptibility in $[001]$ exceeds the one acquired $\perp [001]$. There is no clear evidence for magnetic spin re-ordering at 7 K from the AC susceptibility data.

3.7. Determination of the ferrimagnetic structure at 25 K

The only significant difference of the nuclear structure at 25 K compared to 298 K is the ordering of the H3 site on the special position $(0, 0.2260, 0.25)$ located in the exact middle between two O5 sites (table 3 and supplementary 5). However, in comparison to 298 K, a change in relative intensity distribution of rockbridgeite-inherent reflections is evident in the HRNPD pattern collected at 25 K for the ferrimagnetic ordering (figure 15). In the absence of additional magnetic satellites, the propagation vector $k = (0, 0, 0)$ leaves eight options for magnetic space groups (MSG) in the parental nuclear space group $Cmcm$ (table 5). Among them, only three MSG $Cm'c'm'$, $Cm'cm'$, and $Cm'c'm$ allow ferri-/ferromagnetic (FM) spin orders, whereas the others describe antiferromagnetic (AFM) alignments. According to results from magnetisation measurements, only $Cmc'm'$, $Cm'cm'$, and $Cm'c'm$ were taken

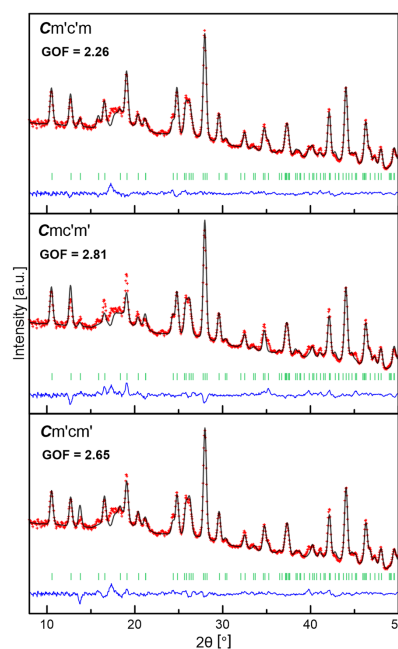


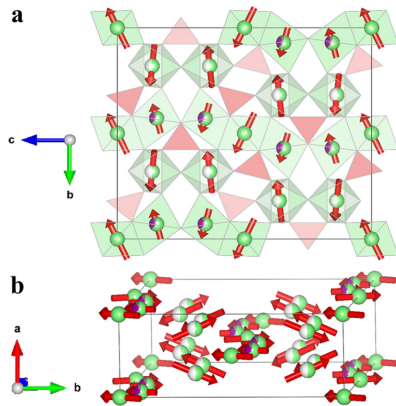
Figure 16. Graphical comparison of results from Rietveld refinements with the three MSG allowing FM order to show the correct model in $Cm'c'm$ with the best agreement factor.

into consideration, giving net magnetisation along the a , b , and c direction, respectively.

Rietveld refinements were performed for these three MSG (figure 16). For software limitation reasons in the refinement, the magnetic form factor of Fe^{3+} was applied for all Fe species, including Fe^{2+} at Fe2 site. The magnetic spin vectors of Mn and Fe at Fe2 were constrained to be equal in direction and length. The spin arrangements in $Cm'c'm'$, $Cm'cm'$,

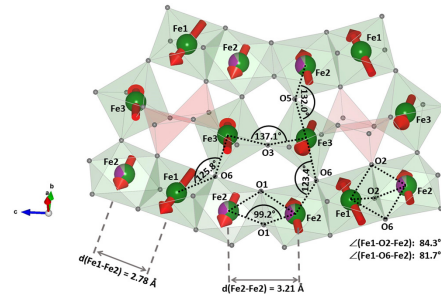
Table 6. Magnetic moment components (m_x , m_y , m_z) along with resulting magnitude M in μ_B obtained from Rietveld analyses with HRNPD data at 25 K (figure 16) for three possible MSG.

MSG	Sites	m_x	m_y	m_z	M
$Cm'c'm$	Fe1	0	-3.8(1)	1.9(2)	4.3(2)
	Fe2	0	-2.9(1)	0.8(2)	3.0(2)
	Fe3	-1.7(2)	3.9(1)	0.4(2)	4.3(4)
$Cmc'm'$	Fe1	-2.5(3)	0	0	2.5(3)
	Fe2	-2.1(2)	0	0	2.1(2)
	Fe3	-0.3(2)	0.7(4)	3.9(1)	4.0(5)
$Cm'cm'$	Fe1	0	-1.8(2)	3.0(1)	3.5(2)
	Fe2	0	-1.7(2)	3.6(1)	4.0(2)
	Fe3	0.8(3)	2.3(2)	-2.2(2)	3.3(4)


Figure 17. Ferrimagnetic spin order (red arrows) of three sublattices Fe1 (filled), Fe2 (mixed occupation), and Fe3 (half-filled) in $Fe^{2+}Fe^{3+}(Mn^{2+}, Zn)_{0.8}(PO_4)_3(OH)_{4.2}(HOH)_{0.8}$, resulting net magnetisation in [001].

and $Cm'c'm$ were refined (supplementary 6). In table 6, the refined magnetic moment components with the magnitude of magnetisation M at each site are given for three FM orders considered. According to results from structure analyses, the Shubkinov group $Cm'c'm$ was chosen as the correct MSG, as exhibiting the best agreement factor (figure 16). More importantly, the resulting M values, i.e. $M(Fe1) = M(Fe3) = 4.3 \mu_B$ and $M(Fe2) = 3.0 \mu_B$, are consistent with the site occupation: Fe^{3+} at Fe1 and Fe3; the occupation of Fe2 mainly by Fe^{2+} . This assignment agrees with the spin-only magnetic moments of Fe^{3+} ($5.92 \mu_B$) larger than that of Fe^{2+} ($4.90 \mu_B$).

Figure 17 visualizes the magnetic spin order refined in space group $Cm'c'm$. For their site symmetries magnetic spin vectors at Fe1 and Fe2 inherit non-zero components only in the $(b-c)$ plane whereas magnetic moments at Fe3 do not have any symmetry restriction. The components of spins in [010] at Fe1 and Fe2, as well as those in both [100] and [010] at Fe3 are cleared out (figure 17). In summary, a net magnetisation in [001] is established by three respective sublattices


Figure 18. Geometrical considerations on magnetic superexchange interactions of $[FeO_6]$ octahedra, as well as double exchange within a h -cluster.

built up by Fe1, Fe2 and Fe3 sites (figure 17(b)). The strongest contribution to magnetisation in [001] derives from 3d TM cations at Fe1, followed by those at Fe2 and Fe3 (table 6). This arrangement is in accordance with increasing $\chi_{AC} \parallel [001]$ below 50 K, since all magnetic spin vectors have their strongest deflections normal to c axis. The crossing-over of the χ_{AC} curves around 50 K measured $\parallel [001]$ and $\perp [001]$ could be due to competitive anisotropic effects of the three magnetic site sublattices dictating the overall spin order. Taking all sites into account, the magnetic structure at 25 K agrees with a calculated magnetisation of about $4.3 \mu_B pfu$ in c direction.

Within a h -cluster of face-sharing octahedra $Fe2-Fe1-Fe2$, the FM spin coupling (figure 18) could be governed mainly by two exchange mechanisms: (i) direct exchange underlying the close inter-cationic distance of about 2.78 Å [30]; (ii) double exchange (DE) mechanisms between Fe^{2+} or Mn^{2+} at Fe2 and Fe^{3+} at Fe1 via bridging 2p oxygen orbitals. These cases are considerable under the angles of $\angle(Fe1-O6-Fe2) = 80.7^\circ$ and $\angle(Fe1-O2-Fe2) = 84.3^\circ$ (x2), similar to the case of magnetite [31]. Interestingly, UV/vis spectra indicated $Fe^{2+}-Fe^{3+}$ intervalence charge transfer in the energy range (765 nm) appropriate for face-sharing octahedral configurations [15]. Consistently with our model, an intensification of a broad UV/vis absorption at 83 K, which covers the energy area of intervalence charge transfer, points to a correlation of charge transfer with ferromagnetic coupling through DE [16].

Magnetic spin coupling between two adjacent h -clusters along [001] through edge-sharing $Fe2$ -octahedra is predominantly AFM. 90° -superexchange interactions, i.e. $\angle(Fe2-O1-Fe2) = 99.2^\circ$, provide several scenarios: FM coupling is expected for $Fe^{2+}-O1-Fe^{2+}$, $Mn^{2+}-O1-Fe^{2+}$, and $Fe^{3+}-O1-Fe^{3+}$ according to the Goodenough-Kanamori (G-K) rules [32]. On the other hand, the $Mn^{2+}-O1-Mn^{2+}$ case is unclear with cation-cation distance of 3.21 Å [33]. The AFM spin order between two h -clusters in [001] can be a consequence of the stronger AFM coupling with the corner-sharing $[Fe_3O_6]$ octahedra over which h -clusters are connected $\perp [001]$ (figure 18). Alternating Fe2 and Fe3 octahedra form infinite AFM chains with the angles

$\angle(\text{Fe3-O6-Fe2}) = 123.4^\circ$ and $\angle(\text{Fe2-O5-Fe3}) = 132.0^\circ$. This agrees with G–K rules predicting AFM spin coupling for either of the possible combinations of $\text{Fe}^{3+}\text{-Fe}^{2+}$, $\text{Fe}^{3+}\text{-Fe}^{3+}$, and $\text{Fe}^{3+}\text{-Mn}^{2+}$. This is valid also for corner-linked Fe3 sites ($\angle(\text{Fe3-O3-Fe3}) = 137.1^\circ$), as well as in corner-linked Fe1 and Fe3 sites ($\angle(\text{Fe1-O6-Fe3}) = 125.8^\circ$). These AFM interactions among corner-sharing octahedra are stronger than the predicted FM interactions from 90° -superexchange [32]. As a consequence, the unusual AFM order between *h*-clusters in the *c* direction can be explained.

4. Conclusion

A comprehensive nuclear and magnetic structural study of a rockbridgeite-type compound was performed using neutron powder diffraction. Subtle information about H sites and their occupation parameters are delivered to show: (1) the H content is strictly correlated to the selective substitution of Fe^{3+} by divalent 3d TM cations at the Fe2 site; (2) the dielectric behaviour points to fast protonic conductivity through the H-bond network; (3) on the basis of the occurrence of new HOH ligand groups, the general formula $\text{Fe}^{2+}\text{Fe}_{4-x}^{3+}(\text{Mn}^{2+}, \text{Zn})_x(\text{PO}_4)_3(\text{OH})_{5-x}(\text{HOH})_x$ is suggested for the rockbridgeite-type series. The relevance of static and dynamic disorder of OH and HOH groups are explained in terms of structural defects in alternately half-occupied octahedral chains. The ferrimagnetic structure below the Curie temperature $T_C = 81\text{--}83$ K could be determined at 25 K. Neutron diffraction data below 7 K is requested to evaluate the ground state of magnetic spin order in rockbridgeite.

To address the protonic superconductivity in this system, further investigations are in progress, e.g. impedance spectroscopy and quasielastic neutron scattering (QENS). Very recently, we observed QENS line broadening in the title compound and will report details elsewhere. Our findings can be applied to develop protonic superconductors for fuel cells and further electrochemically active materials.

Acknowledgments

SHP acknowledges German Federal Ministry of Education and Research (BMBF) for the financial support via 05K13WMB. BR was funded partially by a scholarship from JSPS/DAAD (PE 15779).

ORCID iDs

S-H Park  <https://orcid.org/0000-0003-3127-7662>

References

- [1] Moore P B 1970 *Am. Mineral.* **55** 135–69
- [2] Redhammer G J, Roth G, Tippelt G, Bernroider M, Lottermoser W, Amthauer G and Hochleitner R 2006 *Acta Crystallogr. C* **62** i24–8
- [3] Elliott P, Kolitsch U, Giester G, Libowitzky E, McCammon C, Pring A, Birch W D and Brugger J 2009 *Mineral. Mag.* **73** 131–48
- [4] Frondel C 1949 *Am. Mineral.* **34** 513–40
- [5] Lindberg M L 1949 *Am. Mineral.* **34** 541–9
- [6] Lindberg M L 1950 *Am. Mineral.* **35** 1028–34
- [7] Mattievich E, Vugman N, Diehl L and Danon J 1979 *J. Phys.* **40** 1195–8
- [8] Grodzicki M and Amthauer G 2000 *Phys. Chem. Miner.* **27** 694–702
- [9] Redhammer G J, Tippelt G, Roth G, Lottermoser W and Amthauer G 2000 *Phys. Chem. Miner.* **27** 419–29
- [10] Behal D, Röska B, Park S H, Pedersen B, Benka G, Pfeleiderer C, Wakabayashi Y and Kimura T 2017 *J. Magn. Mater.* **428** 17–27
- [11] Röska B, Park S H, Yoshimori Y, Kimura K and Kimura T 2017 *J. Phys.: Condens. Matter* **29** 365401
- [12] Song Y, Zavalij P Y, Suzuki M and Whittingham M S 2002 *Inorg. Chem.* **41** 5778–86
- [13] Whittingham M S, Song Y, Lutta S, Zavalij P Y and Chernova N A 2005 *J. Mater. Chem.* **15** 3362
- [14] Singh S 2014 *Indian J. Chem.* **53A** 511–5
- [15] Amthauer G and Rossman G R 1984 *Phys. Chem. Miner.* **11** 37–51
- [16] Mattson S M and Rossman G R 1987 *Phys. Chem. Miner.* **14** 94–9
- [17] Rodríguez-Carvajal J 1993 *Physica B* **192** 55–69
- [18] Agilent Technologies SCALE3 ABSPACK—an Agilent Technologies Program
- [19] Oszlányi G and Süt A 2004 *Acta Crystallogr. A* **60** 134–41
- [20] Petříček V, Dušek M and Palatinus L 2014 *Z. Kristallogr.—Cryst. Mater.* **229**
- [21] Hoelzel M, Senyshyn A, Juenke N, Boysen H, Schmahl W and Fuess H 2012 *Nucl. Instrum. Methods Phys. Res. A* **667** 32–7
- [22] Brown I D and Shannon R D 1973 *Acta Crystallogr. A* **29** 266–82
- [23] Renner B and Lehmann G 1986 *Z. Kristallogr.—Cryst. Mater.* **175** 43–59
- [24] Robinson K, Gibbs G V and Ribbe P H 1971 *Science* **172** 567–70
- [25] Chukanov N V et al 2014 *Am. Mineral.* **99** 811–6
- [26] Chukanov N V and Chervonnyi A D 2016 *Infrared Spectroscopy of Minerals and Related Compounds (Springer Mineralogy)* (Cham: Springer) p 1109
- [27] Merinov B 1996 *Solid State Ion.* **84** 89–96
- [28] Adams S 2004 *Solid State Ion.* **168** 281–90
- [29] Kao K C 2004 *Dielectric Phenomena in Solids* (San Diego, CA: Elsevier) pp 41–14
- [30] Goodenough J B 1960 *Phys. Rev.* **117** 1442–51
- [31] Zener C 1951 *Phys. Rev.* **82** 403–5
- [32] Goodenough J B 1963 *Magnetism and the Chemical Bond* (New York: Interscience)
- [33] Motida K and Miyahara S 1970 *J. Phys. Soc. Japan* **28** 1188–96

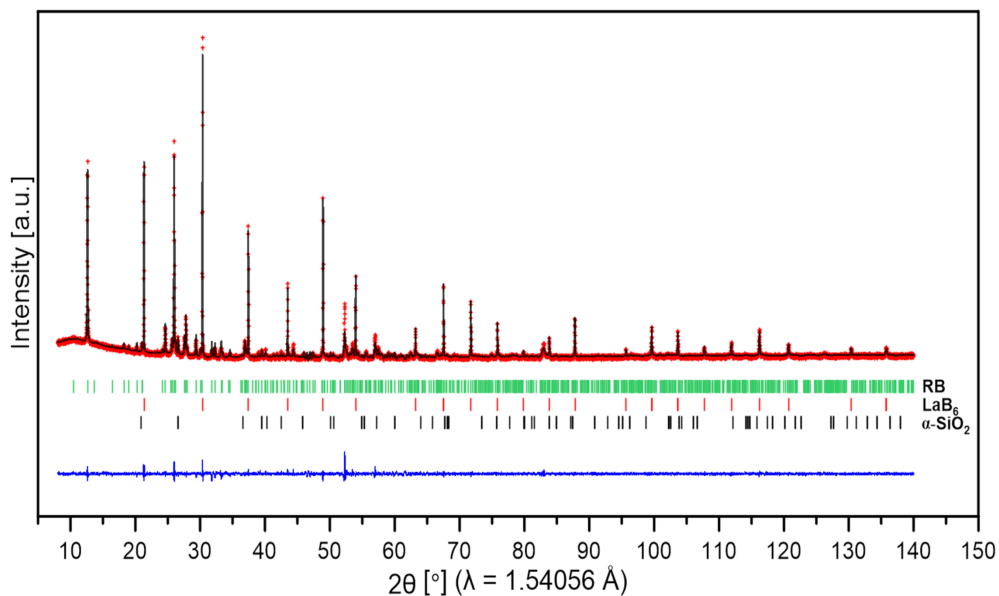
Supplementary 1 Experimental and refinement parameters of X-ray single crystal diffraction (XSD).

Wavelength [Å]	0.71073
Data collection temperature [K]	298
Crystal size [μm^3]	40 x 80 x 80
Theoretical density [g/cm^3]	3.532
Space group	Cmcm (#63)
Formula units per unit cell Z	4
Lattice parameter [Å]	a = 5.180(1) b = 13.991(1) c = 16.870(1)
Maximal $\sin(\theta)/\lambda$	0.68
h k l ranges	-6 < h < 6 -18 < k < 18 -22 < l < 21
Condition for observed reflection	l < 3 σ
Number of unique/total observed reflection	794/8226
Average redundancy	10.4
Absorption correction factors	A _{min} = 0.806 A _{max} = 1.376
R _{int}	5.45
Number of refinement parameters	84
R(F)	4.46
wR(F ²)	11.31
Goodness-of-Fit (S)	3.79
E-E ⁻¹	0.914
(Δ density) _{max}	1.2
(Δ density) _{min}	-1.3

$R(F) = [\sum ||F_o| - |F_c|| / \sum |F_o|]$; $wR(F^2) = [\sum w(F_o^2 - F_c^2)^2 / \sum wF_c^2]^{1/2}$; Weighting $w = 1/(\sigma^2(I) + 0.0004 * I^2)$.

$S = [\sum w(F_o^2 - F_c^2)^2 / (M - P)]^{1/2}$, where F_o and F_c are observed and calculated structure factors, respectively.

M is number of reflections, and P is number of parameters.

Supplementary 2 Graphical presentation of results from LeBail fitting with XRD data of our rockbridgeite powder sample.

Supplementary 3 Atomic parameters of at 298 K from structure refinements with XSD data.

Site	Atom type	Occupancy	x	y	z
Fe1	Fe	1	0	0	0
Fe2	Fe	0.62	0	0.0681(1)	0.1562(1)
	Mn	0.29			
	Zn	0.09			
Fe3	Fe	0.5	0.2310(2)	0.3212(1)	0.1389(1)
P1	P	1	0.5	0.1430(1)	0.0434(1)
P2	P	1	0	0.4823(1)	0.25
O1	O	1	0.2440(8)	0.5456(3)	0.25
O2	O	1	0.2585(5)	0.0807(2)	0.0577(2)
O3	O	0.5	0.3788(15)	0.3130(5)	0.25
O4	O	1	0.5	0.1817(3)	0.9604(2)
O5	O	1	0	0.2168(3)	0.1756(2)
O6	O	1	0.5	0.4233(3)	0.1041(2)
O7	O	1	0	0.4207(3)	0.1748(2)
O8	O	1	0.5	0.2218(3)	0.1067(2)

Supplementary 4 Anisotropic atomic displacement parameters (ADPs) u_{ij} ($i, j=1-3$) with principal mean square ADPs U_i ($i=1-3$) in \AA^2 from structure refinements with XSD data.

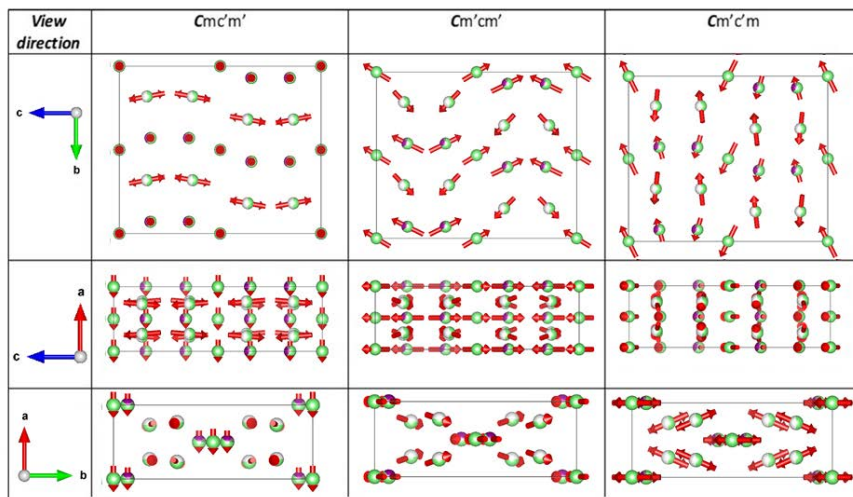
Site	u_{11}	u_{22}	u_{33}	u_{12}	u_{13}	u_{23}	U_1	U_2	U_3
Fe1	0.0089(6)	0.0088(5)	0.0095(6)	0	0	0.0000(4)	0.0089	0.0089	0.0095
Fe2	0.0214(5)	0.0147(5)	0.0125(5)	0	0	-0.0000(3)	0.0125	0.0147	0.0214
Fe3	0.0089(6)	0.0079(6)	0.0052(6)	0.0020(4)	-0.0001(4)	-0.0007(4)	0.0050	0.0066	0.0105
P1	0.0106(7)	0.0066(6)	0.0041(6)	0	0	-0.0009(5)	0.0038	0.0069	0.0106
P2	0.0134(10)	0.0083(9)	0.0069(9)	0	0	0	0.0069	0.0083	0.0134
O1	0.0215(22)	0.0174(20)	0.0149(20)	-0.0091(18)	0	0	0.0101	0.0149	0.0287
O2	0.0118(14)	0.0111(13)	0.01178(13)	-0.0043(11)	0.0008(11)	-0.0028(10)	0.0066	0.0110	0.0170
O3	0.0126(41)	0.0120(42)	0.0094(41)	0.0068(31)	0	0	0.0055	0.0094	0.0191
O4	0.0394(28)	0.0141(20)	0.0050(19)	0	0	0.0026(15)	0.0043	0.0148	0.0394
O5	0.0423(29)	0.0105(20)	0.0078(19)	0	0	0.0025(16)	0.0063	0.0120	0.0423
O6	0.0123(20)	0.0074(17)	0.0113(19)	0	0	0.0026(15)	0.0061	0.0123	0.0127
O7	0.0183(23)	0.0143(19)	0.0082(19)	0	0	-0.0047(15)	0.0056	0.0168	0.0183
O8	0.0129(20)	0.0078(18)	0.0080(19)	0	0	-0.0046(15)	0.0032	0.0125	0.0129

14. Publication on rockbridgeite

Supplementary 5 Interatomic distances evaluated from structure refinements with XSD at 298 K and HRNPD data acquired at 298 K and 25 K.

	298 K XSD		298 K HRNPD			25 K HRNPD		
	d [Å]	d _p - d [Å]	d [Å]	d _p - d [Å]	Bond valence	d [Å]	d _p - d [Å]	Bond valence
Fe1								
O2 (x4)	2.003(3)	0.018	1.992(5)	0.025	4x 0.534	2.021(4)	0.014	4 x 0.490(5)
O6 (x2)	2.056(4)	0.035	2.066(7)	-0.049	2x 0.437	2.063(6)	-0.028	2 x 0.432(8)
	∅ 2.021(3)		∅ 2.017(6)		∑ 3.010	∅ 2.035(5)		∑ 2.822(15)
Fe2								
O1 (x2)	2.087(3)	0.044	2.097(8)	0.020	2x 0.375	2.111(6)	0.009	2 x 0.358(6)
O2 (x2)	2.140(3)	-0.009	2.128(7)	-0.011	2x 0.344	2.118(6)	0.002	2 x 0.351(5)
O5	2.106(4)	0.025	2.061(11)	0.056	0.415	2.041(9)	0.079	0.432(10)
O6	2.209(4)	-0.078	2.192(11)	-0.075	0.289	2.220(9)	-0.100	0.265(7)
	∅ 2.132(3)		∅ 2.117(9)		∑ 2.143	∅ 2.120(7)		∑ 2.116(17)
Fe3								
O3	2.027(3)	-0.0035	2.056(6)	-0.034	0.448	2.043(5)	-0.030	0.458(6)
O4	2.057(3)	-0.0335	2.011(6)	0.011	0.506	1.989(6)	0.024	0.532(8)
O5	1.986(3)	0.0375	2.013(8)	0.009	0.503	1.988(7)	0.025	0.537(10)
O6	2.079(3)	-0.0555	2.083(8)	-0.060	0.416	2.083(7)	-0.070	0.415(8)
O7	1.932(3)	0.0915	1.955(7)	0.067	0.588	1.984(7)	0.029	0.540(10)
O8	2.042(3)	-0.0185	2.016(7)	0.006	0.501	1.989(6)	0.024	0.535(9)
	∅ 2.024(3)		∅ 2.022(14)		∑ 2.963	∅ 2.013(6)		∑ 3.017(21)
P1								
O2 (x2)	1.543(3)	-0.009	1.575(6)	-0.03475	2x 1.120	1.541(5)	-0.0115	1.229(18)
O4	1.501(4)	0.033	1.520(10)	0.02025	1.294	1.513(9)	0.0165	1.311(30)
O8	1.534(4)	0.000	1.491(10)	0.04925	1.404	1.523(8)	0.0065	1.276(29)
	∅ 1.534(4)		∅ 1.540(8)		∑ 4.939	∅ 1.530(7)		∑ 5.045(49)
P2								
O1 (x2)	1.543(4)	-0.001	1.541(10)	-0.003	2x 1.229	1.546(8)	-0.0055	1.210(26)
O7 (x2)	1.533(4)	0.009	1.535(9)	0.003	2x 1.248	1.535(7)	0.0055	1.231(24)
∅	∅ 1.542(4)		∅ 1.538(10)		∑ 4.954	∅ 1.541(8)		∑ 4.882(50)
H1								
O3			0.97(2)		0.807	0.97(2)		0.798
O8 (x2)			2.51(1)		0.151	2.49(1)		0.078
					∑ 0.959			∑ 0.96
H2								
O1			2.85(2)		0.043	2.944(13)		0.036
O2			2.57(2)		0.068	2.523(13)		0.074
O3			2.32(2)		0.105	2.294(14)		0.110
O4			2.61(2)		0.064	2.494(12)		0.078
O5			1.01(1)		0.698	1.104(8)		0.495
O8			1.86(1)		0.231	1.743(8)		0.279
					∑ 1.209			∑ 1.072
H3								
O1 (x2)			2.87(2)		0.082	2.790(21)		0.094
O3			2.33(1)		0.103	2.301(26)		0.108
O5			0.97(2)		0.785	1.280(61)		0.469
O5*			1.60(2)		0.332	1.280(61)		0.469
O7			2.82(2)		0.045	3.020(20)		0.032
					∑ 1.346			∑ 1.174
H4								
O2			2.46(4)		0.082	2.690(30)		0.056
O3			2.70(4)		0.065	2.620(30)		0.063
O4			2.51(3)		0.076	2.370(20)		0.096
O6			0.99(2)		0.737	0.992(13)		0.738
O7			1.89(2)		0.217	1.943(16)		0.199
					∑ 0.951			∑ 0.95

Supplementary 6 Comparison of spin structures in three ferrimagnetic (FM) subgroups of $Cmcm$. The correct magnetic space group is $Cm'c'm$ according to Rietveld analyses.



Acknowledgement

I am very lucky to have family and friends greatly supporting me throughout the time in which this thesis was prepared. They spent the necessary motivation to put away discouraging drawbacks. They were happy with me for every small step taken. I am very grateful to be surrounded by such wonderful people.

I want to express my sincere gratitude to my supervisor, Prof. Dr. SoHyun Park. In a BSc course she raised my interest to study crystallography and diffraction techniques. Giving me the chance to work as a student assistant, our collaboration intensified during my Master thesis and the present work.

SoHyun Park invested great efforts in making possible my position for doctorate studies. She helped me to make the highly valuable experience of working in an external lab at the Osaka University.

With her kind nature, she always created a pleasant atmosphere within the working group, also spending private time with us. Her door was always open to ask questions and for help. I am very thankful to have learned many things about crystallography and beyond.

I want to especially thank Prof. Dr. P. Gille for his continuous support and helpfulness during the past years. Apart from his valuable professional advices, I am deeply grateful for his engagement for my doctorate position.

I also want to thank Prof. Dr. W. W. Schmahl for his support for my position at the beginning of my doctorate studies.

I acknowledge Prof. Dr. T. Kimura (Tokyo University) for kindly hosting me for 6 months at his group at the Osaka University. During my stay, I could make many new and highly precious scientific but also cultural experiences.

My special thanks go to my working group colleagues Dr. Ulf Gattermann and David Behal. Apart from our close collaborations we became friends. It was a great time sharing the office and I am thankful for their advices and introduction when I started my work.

Finally, I want to thank all the colleagues of the Sektion Kristallographie at the LMU. We shared wonderful collaborations inside, and also outside the labs.

Last but not least, I want to thank my doctorate colleagues Alexander Reul, Felix Hentschel, and Korbinian Schiebel for the long and close friendship, starting from our first classes during the BSc studies.

List of publications

Behal D, **Röska B**, Gattermann U, Reul A and Park S-H. Structure analysis of a Mn-doped willemite-type compound, $\text{H}_{0.12}(\text{Zn}_{1.89(3)}\text{Mn}_{0.05(1)}\square_{0.06})\text{Si}_{1.00(1)}\text{O}_4$. *Journal of Solid State Chemistry* **210** 144–9, 2014.

Gattermann U, **Röska B**, Paulmann C and Park S-H. Large single crystal growth of MnWO_4 -type materials from high-temperature solutions. *Journal of Crystal Growth* **453** 40–8, 2016.

Behal D, **Röska B**, Park S-H, Pedersen B, Benka G, Pfeleiderer C, Wakabayashi Y and Kimura T. The first study of antiferromagnetic eosphorite-childrenite series $(\text{Mn}_{1-x}\text{Fe}_x)\text{AlPO}_4(\text{OH})_2\text{H}_2\text{O}$ ($x=0.5$). *Journal of Magnetism and Magnetic Materials* **428** 17–27, 2017.

Röska B, Park S-H, Yoshimori Y, Kimura K and Kimura T. Anomalous dielectric response of short hydrogen bonds under pressure: the case of $(\text{Mn, Fe})^{2+}\text{AlPO}_4(\text{OH})\text{H}_2\text{O}$. *Journal of Physics: Condensed Matter* **29** 365401, 2017.

Röska B, Park S-H, Behal D, Hess K-U, Günther A, Benka G, Pfeleiderer C, Hoelzel M and Kimura T. Determination of the hydrogen-bond network and the ferrimagnetic structure of a rockbridgeite-type compound, $\text{Fe}^{2+}\text{Fe}_{3.2}^{3+}(\text{Mn}^{2+}, \text{Zn})_{0.8}(\text{PO}_4)_3(\text{OH})_{4.2}(\text{HOH})_{0.8}$. *Journal of Physics: Condensed Matter* **30** 235401, 2018.

Röska B, Akter I, Hoelzel M and Park S-H. Na^+/Li^+ -ionic conductivity in $\text{Fe}_2\text{Na}_2\text{K}[\text{Li}_3\text{Si}_{12}\text{O}_{30}]$. *Journal of Solid State Chemistry* **264** 98–107, 2018.

Conference contributions

Japan-Korea-Taiwan Workshop on Strongly Correlated Electron Systems, Tokyo - Japan, 2016.

Poster: "2D dynamics of Na^+ and Li^+ ions in a 6-er double-ring silicate, sugilite."

B. Röska, S.-H. Park

International Conference on neutron scattering, Daejeon - Rep. Korea, 2017.

Poster: "The magnetic structure and anomalous dielectric response of $(\text{Mn}_{1-x}\text{Fe}_x)^{2+}\text{AlPO}_4(\text{OH})_2\text{H}_2\text{O}$ ($x = 0.5$)"

B. Röska, D. Behal, S.-H. Park, B. Pedersen, G. Benka, C. Pfeleiderer, Y. Yoshimori, Y. Wakabayashi, K. Kimura, T. Kimura